TRANSFER PRINTING BASED MICROASSEMBLY AND COLLOIDAL QUANTUM DOT
FILM INTEGRATION

BY

HOHYUN KEUM

DISSERTATION

Submitted in partial fulfillment of the requirements
for the degree of Doctor of Philosophy in Mechanical Engineering
in the Graduate College of the
University of Illinois at Urbana-Champaign, 2017

Urbana, Illinois

Doctoral Committee:

      Assistant Professor Seok Kim, Chair
      Professor Placid M. Ferreira
      Professor John A. Rogers
      Associate Professor Moonsub Shim

Abstract

Micro / nanoscale manufacturing requires unique approaches to accommodate the immensely different characteristics of the miniscule objects due to their high surface area to volume ratio when compared with macroscale objects. Therefore, surface forces are much more dominating than body forces, which causes the significant difficulty of miniscule object manipulation. Because of this challenge, monolithic microfabrication relying on photolithography has been the primary method to manufacture micro / nanoscale structures and devices in place of microassembly. However, by virtue of the two-dimensional (2D) nature of photolithography, formation of complex 3D shape architectures via monolithic microfabrication is inherently limited, which would otherwise enable improvements in performance and novel functionalities of devices. Furthermore, monolithic microfabrication is compatible only with materials which survive in a wet condition during photolithography. Delicate nanomaterials such as colloidal quantum dots cannot be processed via monolithic microfabrication. In this context, transfer printing has emerged as a method to transfer heterogeneous material pieces from their mother substrates to a foreign substrate utilizing a polymeric stamp in a dry condition. In this thesis, advanced modes of transfer printing are studied and optimized to enable a 3D microassembly called 'micro-Lego' and a novel strategy of quantum dot film integration. Micro-Lego involves transfer printing for material piece pick-and-place and thermal joining for irreversible permanent bonding of placed material pieces. A microtip elastomeric stamp is designed to advance transfer printing and thermal joining processes are optimized to ensure subsequent material bonding. The mechanical joining strength between material pieces assembled by micro-Lego are characterized by means of blister tests and the nanoindentation. Moreover, the electrical contact between two conducting materials formed by micro-Lego are examined. Lastly, inspired from the subtractive transfer printing technique,

protocols of quantum dot film patterning using polymeric stamps made of a shape memory polymer as well as a photoresist are established for the convenient integration of quantum dots in various geometries and configurations as desired. Transfer printing-based micro / nanoscale manufacturing presented in this thesis opens up new pathways to manufacture not only complex 3D functional micro devices but also high resolution nano devices for unparalleled performance or for an unusual functionality, which are unattainable through monolithic microfabrication.

Acknowledgements

I would like to begin by mentioning that every result addressed in this thesis was accomplished by full support from my principal investigator, professor Seok Kim and all colleagues, coauthors and staff members at University of Illinois. It has always been my pleasure to work in collaboration and I'm genuinely thankful for their contributions for the researches that I could accomplish throughout my graduate school years. They all flourished my experience at University of Illinois and it has been my privilege to work with such outstanding individuals.

By foremost, I express my deepest gratitude to professor Seok Kim for his mentoring, guidance, patience and the endless encouragements. He has always been an approachable advisor to guide me when I am profoundly disoriented from my research. His philosophy in research and advising greatly disciplined me and I cannot express how much I am indebted to him. Also, I would like to convey my gratitude to Professor John A. Rogers who had given me an opportunity to work in his group as a participating undergraduate researcher. All the experience obtained while in his group had established the profound fundamentals of my research. I would like to extend my thanks to Professor Placid M. Ferreira who has provided instructions with his keen insights for more in depth analysis and Professor Moonsub Shim for widening my research experience in the nanomaterial field.

I'm obligated to acknowledge Dr. Glennys A. Mensing for all her supports, suggestions and discussions. She not enriched my graduate student experience by offering me a teaching assistant position in her class, but also her consultation with my own projects has always been valuable. All staff members at Micro Nano Mechanical Systems, Frederick Seitz Materials Research Laboratory, Micro and Nano Technology Laboratory and department of mechanical

science and engineering, especially Joe Maduzia, Miki Takagi and Kathryn A. Smith have always been admirable supporters. I must thank my colleagues in my group, Jeffrey Eisenhaure, Zining Yang and Jun Kyu Park for their cooperation, motivation, support and friendship. I had pleasuring knowing, working and discussing with them. I tried my utmost effort to acknowledge all the people supported and accompanied me throughout my years at University of Illinois and I present my sincerely apologies for those whom I may have missed.

Last but not least, I would like to thank my parents and my sister, Youngsoo Keum, Mihee Lee and Sohyun Keum for their years of support and care. Their sacrifice and encouragements motivated and guided me. Thank you, for your explicit love and enduring support.

Table of Contents

List of Figures

List of Tables

Chapter 1.　　Introduction

1.1　Micromanufacturing Overview

Development of micromanufacturing enabled fabrication of microscale devices with comparatively low cost-to-performance ratio by reducing the waste accommodated in the manufacturing process while maintaining high throughput. Not only the micro devices are profiting from the manufacturing perspective, they also merit from light weight for portability, high sensitivity, low energy consumption and processing performance due to their size effect [1,2]. Owing to the excellences mentioned, the micro devices can be found in various applications namely microelectromechanical systems (MEMS) and micro optical electronics systems (MOES), micro reactors, heat exchangers, fuel cells, micro robots, micromedical components [3-8]. The universally found microchips and micro devices merit our everyday lives and becoming inevitable for the continuation of our modern life styles.

Additionally, recent advances in connected objects or internet of things (IoT) augments the demand of microchips with higher computing power in compact format, which subsequently requires evolution of the micromanufacturing techniques. Micromanufacturing requires sparsely different approach from meso / macro scale manufacturing due to the domineering surface effect and the requirement for high resolution alignment while reducing the error that can be originated from the thermal effect as well as the vibrations from various sources. Due to the aforementioned reasons, adaptation of manufacturing schemes in macroscales by simply scaling down to microscale is not feasible, which have led researchers to investigate on diverse strategies and methodologies for efficient manufacturing techniques in microscale.

Numerous micromanufacturing techniques have been developed as listed in **Table 1.1,** which are classified according to the components formation methodologies [9]. The listed micromanufacturing processes have genuinely focused on miniaturization of the microdevices for higher performance while maintaining the miniscule footprint. However, the future microsystems require immensely different micromanufacturing techniques that enable functional integration in a compact format to open new opportunities. Some recently developed devices with functional integrations are polymer based lab-on-a-chip platform which incorporates microfluidic system and actuators with planar surface plasmon resonance sensors and optical lens with micron-scale metal interconnects and light-emitting diodes (LED) for display purposes [10-12]. In order to fully exploit the functional system integration, a new micromanufacturing approach that enables incorporation of different length-scale structures and features in a single component need to be developed. In this aspect, three dimensional (3D) microassembly process, which enables assembly of microscale objects and devices is a persuasive alternative approach.

Table 1.1 *Classification of micromanufacturing processes based on components formation methodology [9]*

Subtractive processes	Micro-Mechanical Cutting (milling, turning, grinding, polishing, etc.); Micro-EDM; Micro-ECM; Laser Beam Machining; Photo-chemical-machining; etc.
Additive processes	Surface coating (CVD, PVD); Direct writing (inkjet, laser-guided); Micro-casting; Micro-injection moulding; Sintering; Photo-electro-forming; Chemical deposition; Polymer deposition; Stereolithography; etc.
Deforming processes	Micro-forming (stamping, extrusion, forging, bending, deep drawing, incremental forming, superplastic forming, hydro-forming, etc.); Hot embossing; Micro/Nano-imprinting; etc.
Joining processes	Micro-Mechanical-Assembly; Laser-welding;

Table 1.1 *(continued)*

Hybrid processes	Micro-Laser-ECM; LIGA and LIGA combined with Laser-machining; Micro-EDM and Laser assembly; Shape Deposition and Laser machining; Efab; Laser-assisted-micro-forming; Micro assembly injection moulding; Combined micro-machining and casting; etc.

1.2 Three dimensional additive microassembly techniques

1.2.1 Overview of MEMS fabrication techniques and three dimensional additive microassembly processes

MEMS devices has been mainly based on Si, due to its abundance and compatibility with other micromanufacturing processes, which had been developed for past several decades. The MEMS manufacturing techniques are based on the monolithic microfabrication, which fundamentally originated from the silicon industry manufacturing field such as oxidation, diffusion ion implantation, low pressure chemical vapor deposition (LPCVD), sputtering, etc., yet the inclusion of the mobile components for actuation or sensing purposes require different approach in the fabrication of MEMS devices. The processes of MEMS device fabrications are typically divided into bulk micromachining, surface machining and combination of lithographie, galvanoformung and aboformung (stands for lithography, electroplating and molding, abbreviated as LIGA) processes.

Bulk micromachining involves creating 3D components by removing materials from thick substrates (generally Si) using primarily etching methods. The etching process is carried out by either chemical wet etching, gas phase etching and reactive ion etching (RIE) schemes. A wet etching process, depending on the material and the etchant utilized in the process, can be isotropic or anisotropic. The isotropic wet etching arises when the etch rate is independent with the crystal planes of the substrate, while the anisotropic wet etching exhibits high selectivity between the

3

different crystal planes. Through exploiting the anisotropic wet etching characteristics, shapes such as pyramidal or wedge, can be accomplished conveniently. The gas phase etching is usually carried out in xenon difluoride (XeF_2), which etches Si by mere chemical reaction without any plasma assisted dissociation of the radicals involved like in RIE. Overall, the process is capable of manufacturing simple geometry with cost efficiently, while the material loss is high and the aspect ratio is limited [13].

Surface micromachining is another type of manufacturing technique to fabricate MEMS devices. The process is structured by sequence of the material deposition and patterning until desired 3D configuration is formed, at which point, one or more pre-deposited layer (often called sacrificial layer) is removed to construct a 3D free standing structure. When designing the process flow for the surface micromachining process, it is critically to consider the selectivity between diverse class of material deposited in the manufacturing process as well as the process compatibility since some deposition schemes are conducted in relatively high temperature. While integration of different materials in the process arises complexity in the process, the degree of flexibility in the deposited material is a great advantage over bulk micromachining process [14,15]. Additionally, the deposition can achieve higher aspect ratio than bulk micromanufacturing process, while less waste is resulted in the process. However, the process requires bulk capital equipment for deposition as well as multiple masks, which increases total cost of the device fabrication.

Lastly, the LIGA process is primarily a non-silicon based technology, which incorporates synchroton generated x-ray radiation for lithography process. Poly(methyl methacrylate) (PMMA) is the commonly used resist in the process, that is sensitive to the x-ray beam with relatively deep penetration depth for nearly perfect vertical sidewalls. The LIGA process constitutes of PMMA

coating and patterning on metal substrate, which is electroplated to fill the patterned PMMA region. Following the electroplating is the removal of PMMA layer, which reveals the electroplated micro components for the MEMS device application. While the capable of creating high aspect ratio objects, flexibility in microstructure configuration and geometry and convenient incorporation of metallic microstructures in LIGA process are favorable, the incorporation of the advanced lithography tool as well as the specially designed mask for PMMA patterning raises the total cost of the process [16].

Other MEMS fabrication techniques namely hot embossing, laser micromachining, electro-discharge micromachining, focused ion beam (FIB) micromachining are being researched to complement the drawbacks of the aforementioned methodologies, but their adaptation in MEMS manufacturing is immature as of now. While the three MEMS micromanufacturing processes have demonstrated their capability in MEMS device fabrication, the techniques suffer from means of integrating diverse microscale components and microdevices on a single chip to create multi-functional devices. 3D microassembly micromanufacturing techniques have drawn much anticipation in this scope where the techniques are expected to complement the limitations of the broadly adopted MEMS fabrication techniques by establishing convenient integration of diverse class of microscale objects and microdevices.

1.2.2 Serial microassembly processes

Serial microassembly process, also called pick-and-place process is inspired from macro / meso manufacturing techniques where individual constituents are fabricated independently, and subsequently joined to form a uniform structure. 'Design for assembly' concept established by Boothroydm in 1982, which describes that the assembly process of an aggregate product is

streamline by a clever design of its individual components in in the fundamentals of the serial microassembly process due to the number of different factors to consider in microscale when compared with macroscale as described in **Table 1.2** [17, 18]. Development of grippers or manipulators for microscale, high precision positioning system as well as the proper fixturing schemes are the elementary aspects that requires immediate development for microassembly process.

Table 1.2 *Comparison between microassembly with macroscale [18]*

Feature	Macroscale	Microscale
Dominant forces	Gravity, friction	Electrostatic, Van der Walls, stiction, capillary, friction
Positioning	Simple	Complex, very high resolution required
Velocity	Rapid: cm/s, m/s	Slow: μm/s, mm/s
Force sensing	Simple	Difficult, forces can be as low as a few μN
Grippers	Mechanical, well established	Micromechanical, suction, vacuum, etc. other under development
Fixturing	Mechanical, well established	Micromechanical, subject of further development
Handling	Simple	Complex, parts are very fragile and subject to micro-scale forces
Vision system	Simple, well established	Complex, costly, requires further development
Throughput / manipulation	Serial	Parallel and serial

A field that has been extensively explored for serial microassembly is in the development of grippers or manipulator, which includes electrostatic microgrippers, optical microgrippers, mechanical fingers, haptic technology-based gripping approach and shape memory alloy (SMA) – based grippers. Cecil and his coauthors have comprehensively summarized the recently emerged

microgrippers with its key aspects and applications as shown in **Table 1.3** [19]**.** The list is extensive but their detailed descriptions are neglected for the scope of this thesis, yet their references are included for assistance. A few microgrippers are disregarded since their originalities are not profoundly discoverable.

Table 1.3 *List of different grippers developed and their key aspects and applications [19]*

Publication	Principles and approach	Application and other key aspects
Ballandras et al. [20]	• Fabrication using the LIGA technique	• Annealing improves the gripper performance
Yi and Liu [21]	• Magnetic actuation techniques • Electroplating techniques to fabricate grippers	• Quick response assembly of optical devices
Ivanova et al. [22]	• Thermal actuation	• Used in dusty and atmosphere / vacuum environments
Chen et al. [23]	• Active releasing method developed • Reduce the adhesion forces	• Robotic pick-and-place operation
Nashrul and Shirinzadeh [24]	• Cantilever beam structure and flexure hinge approaches • Piezoelectric mechanism for actuation	• High-precision positioning systems
Wester et al. [25]	• Mechanically actuated MEMS micro-tweezer • Electroplating-based processes used to fabricate tweezer components	• Used in remote, minimally invasive surgical and dissection procedure
Hamedi et al. [26]	• Electrostatic micro-gripping system applying comb drive mechanism	• Manipulates two micro-components simultaneously
Kohl et al. [27]	• SMA thin sheet and two integrated actuations • Folded beam structure with two circular beams	• Finite element simulations for stress and strain profile evaluation

Table 1.3 *(continued)*

Publication	Principles and approach	Application and other key aspects
Kohl et al. [28]	• Gripping devices mounted between substrates • Photo sensor used to identify the optical properties	• FEM used for analysis of temperature distribution
Roch et al. [29]	• Monolithic and hybrid process of SMA thin film used • SU-8 gripper and SMA glued and assembled in a closed-state position	• FEM used for determining the force and amplitude • Micrometric gold ruler used for the measurement of displacement • Used for MEMS applications
Kyung et al. [30]	• Use of SMA wires, flexible hinges • Two gripping jaws • Fabricated the gripper using electo-discharge machining	• FEM for optimizing the gripper width
Daly et al. [31]	• Monolithic self-positioning Ni Ti shape memory micro-gripper	• Resistive heating measurements used to monitor thermal actuation • Used for micro-manipulation

In conjunction with the development of the microgrippers for the manipulation in microscale, automated stages that allow programmable microassembly have been developed as shown in **Figure 1.1**. **Figure 1.1 (a)** is M^3 Packaging System developed by Automation and Robotics Research Institute at the University of Texas at Arlington (UTA), which is based on three robotic end-effectors with nanometer levels of positioning with motorized stages and 19 degree of freedom (DOF) [32]. Another microassembly system was developed by group of researchers from ETH Zurich, which focuses on the assembly of hybrid MEMS parts and other micro-components through mechanical grippers (**Figure 1.1 (b)**) [33]. Xie also developed an atomic force microscope

(AFM) based 3D micromanipulation system (3DMS) with a nanotip gripper that features real-time interactive force sensing for monitoring as shown in **Figure 1.1 (c)** [34,35].
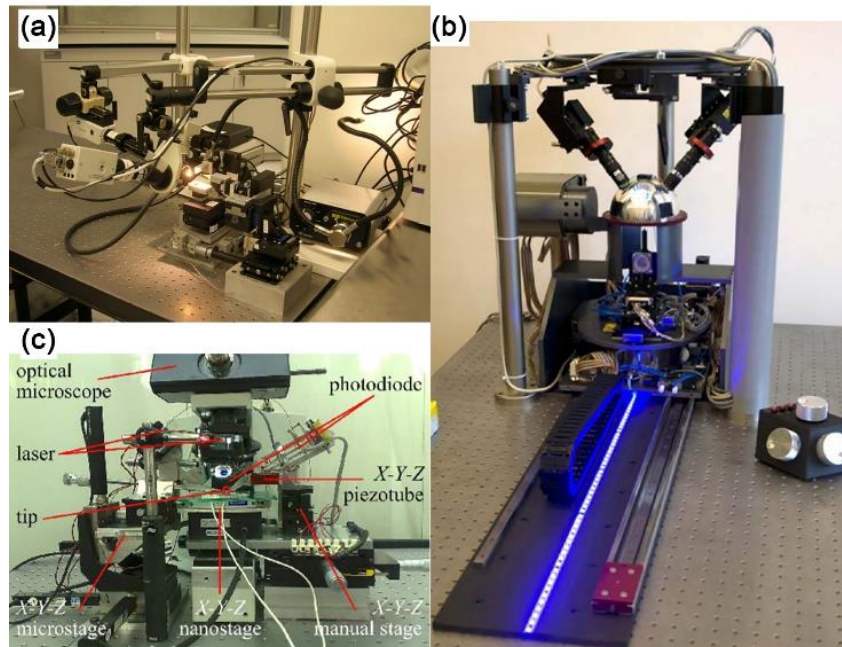
Figure 1.1 Microassembly instruments from (a) Automation and Robotic Research Institute at the University of Texas Arlington called "M³" [18] and (b) ETH Zurich's "Microassemby System V2" [19] (c) AFM based 3D micromanipulation system (3DMS) developed by Xie [34,35]

Although the development of microgrippers as means of manipulator and the automated system are perceivably a route for future microassembly technique, the serial microassembly process is yet impeded from complicated and bulky instrument for automation. Furthermore, throughput of the assembled commodity suffers from the serial protocol since incorporation of multiple manipulator in the limited workspace in the stage is unrealistic due to the relatively larger manipulator footprint [36, 37].

1.2.3 **Parallel microassembly processes**

Parallel microassembly process, which is capable of assembling multiple components or devices simultaneously is an alternative route that can complement the drawbacks of the

throughput in the serial microassembly process. Additionally, given that the most micromanufacturing techniques are batch process where collective components are prepared concurrently, the parallel microassembly process is more compatible platform in the micromanufacturing protocol than serial assembly approach [38]. There are two approaches for parallel microassembly namely deterministic parallel microassembly and stochastic parallel microassembly.

Deterministic microassembly is commonly conducted by wafer-to-wafer transfer of microstructures where the placements of individually configured objects are predetermined by their layout on the wafer. In this manner, the alignment of large scale microassembly can be conducted effortlessly. However, the challenges lie in the releasing mechanism from the processed substrate as well as in the joining practices of the microscale units onto the target site. Epitaxial lift-off (ELO) technique had been demonstrated, which is utilized to release III/V device structure from its gallium arsenide (GaAs) substrate using selective wet etching a thin release layer is an example of deterministic microassembly technique that is hindered by the large consumption of the waste as well as back-end modification [39-41]. In this aspect, flip-chip bonding or batch transfer microassembly are the most distinguishing approaches by their compatibility, throughput and simplicity in the process [42,43]. The flip-chip bonding is utilized in the application of chip packaging as a route to establish an interconnection between IC chips and MEMS devices with an external circuitry while avoiding cumbersome serial techniques such as wire bonding [44,45]. By replacing the traditional wire bonding, the electrical lines are truncated, leading to short delay in signal, less power loss, higher heat conductance, reduced inductance as well as reducing the form factor of the overall device package. Although the flip-chip bonding is tremendously advantageous, the immature joining mechanisms require further study to be widely utilized.

Stoichiometry, also can be referred as self-assembly, is based on the natural phenomena where all systems evolve towards a state of minimal potential energy. The driving force for this shift is insignificant in macroscale, yet they are powerful enough to redistribute or reorient the micro objects. To accomplish successful self-assembly, a few criteria must be satisfied. Firstly, the assembled state must exhibit lower potential energy. Secondly, the driving energy supplied should be larger than the energy barrier to accomplish the ground state that is displayed upon fully assembled situation. Thirdly, external energy must be provided which is converted to the random kinetic energy for the objects to redistribute themselves to the ground state [46]. Fluidic agitation with ultrasonic vibration is a persuasive method of supplying this random kinetic energy that has been explored comprehensively, as well as other approaches as addressed in **Table 1.4**. Although the list is not comprehensive of all the self-assembly techniques demonstrated up to date, the most commonly exploited driving energies are capillary, electrostatic, magnetic and optics are addressed.

Both flip-chip bonding and self-assembly are compelling approaches for future 3D microassembly techniques owing to their efficiency in mass production and their simplicity in the instruments setup when compared with most of the serial 3D microassembly techniques. The flip-chip bonding at the current stage requires specific combination of materials to be joined, which requires extensive development for broader adaptation. Additionally, the technique is mostly utilized in the packaging stage where the devices are firstly prepared monolithically. In contrast, the self-assembly process requires in depth analysis in energy level prior to utilization in the micromanufacturing, which can be complex and often not applicable with most of the materials used in the micromanufacturing. Additionally, while the individual micro objects can be reorganized into specified site, their structural integrity is doubtful since most of the researches spared on their assembly, not on their reliability in the scope of robustness of their joining. The

next chapter will discuss on the transfer printing process, which is a type of parallel microassembly process that can potentially complement the limitations of the flip-chip bonding and self-assembly processes.

Table 1.4 Self-assembly techniques [19]

Publication	Principles and approach	Application and other key aspects
Tien et al. [47]	• Development of micro-assembly process through the use of electrostatic force • Mechanisms and processes for charging of micro-parts electrostatically for binding	• Experimental analysis of various chemical components for micro-parts assembly
R. R. A. Syms [48]	• Analysis of various materials used for generation of surface tension by rotation • Examination of various mechanisms and components for precise measurement and control of surface tension forces	• Examination of various layouts suitable for self-assembly of micro-parts
Harsh et al. [49]	• Determination of various system parameters for soldering process using VR models • Detailed controlling factor analysis of soldering process	• Self-assembly of 3D structures with the help of soldering technology
Clark [50,51]	• Capillary self-assembly • Target binding sites can also be on the micro-devices themselves	• Creation of 3D device structures
Wang [52]	• External magnetic fields	• Manipulation of ferromagnetic parts

1.3   **References**

[1]   Koc, M., and Ozel, T., *Micro-manufacturing: design and manufacturing of micro-products,* John Willey wr   & Sons, 2011

[2]   Jain, V. K., et al., *Micromanufacturing: a review-part I,* Proceedings of the Institution of Mechanical Engineers, Part B: Journal of Engineering Manufacture, 2014, **228**.9: p. 973-994

[3]   Jain, V. K., Dixit, U. S., Paul, C. P., and Kumar, A., *Micromanufacturing : A review-part II,* Proceedings of the Institution of Mechanical Engineers, Part B: Journal of Engineering Manufacture, 2014, **228**.9: p. 995-1014

[4]   Qin, Y., Mishima, N., and Ashida, K., *Microfactory and micro machine tool,* The 1st Korea-Japan Conference on Positioning Technology, Daejeon, Korea 2002

[5]   Claessen, U and Codourey, A., *Microfactory*, Section Head CSEM CH 6055 Alpnach, Switzerland, 2002

[6]   Rachkovkij, D. A., et al., *Heat exchange in short micro tubes and micro heat exchangers with low hydraulic losses,* Journal of Microsystems and Technology, 1998, **4**: p. 151-158

[7]   Aoki, I., et al., *Trial production of medical micro tool by metal deformation processes using moulds,* IEEE Proceedings, 1995: p. 344-349

[8]   Yeh, R., Kruglick, E. J. J., Pister, K. S. J., *Surface-micro machined components for articulated micro robots,* Journal of Microelectromechanical Systems, 1996, **5**: p. 10-17

[9]   Qin, Y., *Overview on Micro-Manufacturing, Micro-manufacturing Engineering and Technology,* Glasgow, Elsevier, 2009

[10]   Nestler, J., et al, *Polymer lab-on-chip systems with integrated electrochemical pumps suitable for large scale fabrication*, International Journal of Advanced Manufacturing Technology, 2010, **47**: p. 137-145

[11]   Ho, H., et al, *Contact lens with integrated inorganic semiconductor devices,* Proceedings of the IEEE 21st International Conference on Micro electro mechanical systems (MEMS 2008), Tucson, Arizona: p. 403-406

[12]   Dimov, S., Brousseau, E., Minev, R., and Bigot, S., *Micro- and nano- manufacturing: Challenges and opportunities,* Proceedings of the Institution of Mechanical Engineers, Part C: Journal of Mechanical Engineering Science, 2012, **226**.1: p. 3-15

[13]   Qin, Yi. *Micromanufacturing engineering and technobology*. William Andrew, 2010.

[14]   Bustillo, J. M., Roger T. H., and Richard S. M., *Surface micromachining for microelectromechanical systems. Proceedings of the IEEE,* 1998, **86**.8: p. 1552-1574.

[15]   Howe, R. T. *Surface micromachining for microsensors and microactuators.* Journal of Vacuum Science & Technology B: Microelectronics Processing and Phenomena, 1988, **6**.6: p. 1809-1813.

[16]   Ehrfeld, W. *The LIGA process for microsystems.* Micro System Technologies. Springer Berlin Heidelberg, 1990. 521-528.

[17]   Boothroydm G., *Design for assembly: The Road to Higher Productivity*, Assembly Engineering, March, 1982

[18]   Bogue, R., *Assembly of 3D micro-components: a review of recent research,* Assembly Automation, 2011, Vol. **31**, Issue 4: pp. 309-314

[19]   Cecil, J., Barathi Raj Kumar, M. B., Lu, Y., and Basallali, V., *A review of micro-devices assembly techniques and technology*, International Journal of Advanced Manufacturing Technology, 2016, **83**: p. 1569-1581

[20]   Ballandras, S., et al, *Micro grippers fabricated by the LIGA technique*, Sensors and Actuators A Physical, 1997, **58**(3): p. 265-272

[21]   Yi, Y., Liu, C., *Assembly of micro-optical devices using magnetic actuation,*Sensors and Actuators A Physical, 1999, **78**(2-3): p. 205-211

[22]   Ivanova, K., et al., *Thermally driven microgrippers as a tool for micro assembly,* Microelectric Engineering, 2006, **83**(4-9): p. 1393-1395

[23]   Chen, B. K., Zhang, Y., and Sun, Y., *Active release of microobjects using a MEMS microgripper to overcome adhesion forces,* Journal of Microelectromechanical Systems, 2008, **18**(3)**:** p. 652-659

[24]   Nashrul, M., Shirinzadeh, B., *Development of a high precision flexure based micro gripper,* Precision Engineering, 2009, **33**(4): p. 362-370

[25]   Wester, B., et al., *Development and characterization of a packaged mechanically actuated microtweezer system*, Sensors and Actuators A Physical, 2011, **167**(2): p. 502-511

[26]   Hamedi, M., Salimi, P., and Vismeh M., *Simulation and experimental investigation of a novel electrostatic micro gripper system,* Mechatronic Engineering, 2012, **98**: p. 467-471

[27]   Kohl M., Just, E., Pleging, W., and Miyazaki S., *SMA micro gripper with integrated antagonism,* Sensors and Actuators A Physical, 2000, **83**(1-3) p. 208-213

[28]   Kohl, M., Krevet, B., and Just, E., *SMA micro gripper system,* Sensors and Actuators A Physical, 2002, **97-98**: p. 646-652

[29]   Roch, I., Bidaud, P., Collard, D., Buchaillot, L., *Fabrication and characterization of an SU-8 gripper actuated by a shape memory alloy thin film,* Journal of Micoromechanics and Microengineering, 2003, **13**(2): p. 330-336

[30] Kyung, J. H., Ko, B. G., Ha, Y. H., and Chung, G. J., *Design of microgripper for micromanipulation of microcomponents using SMA wires and flexible hinges,* Sensors and Actuators A Physical, 2008, **141**(1): p. 144-150

[31] Daly, M., et al, *Fabrication of a novel laser-processed NiTi shape memory micro gripper with enhanced thermomechanical functionality,* Journal of Intelligent Material Systems and Structures, 2012. **0**: p. 1-7

[32] Popa, D. O., and Stephanou, H., *Multiscale Robotics Architecture for Micro & Nano Manufacturing,* Korea-U.S. NanoForum, Seoul, Korea, April 2006

[33] Probst, M., *Design of an Advanced Micro-Assembly System for the Assembly of Bio-Micro-Robots*, Swiss Federal Institute of Technology Zurich, 2008

[34] Xie, H., and Regnier, S., *Three-dimensional automated micromanipulation using a nanotip gripper with multi-feedback*, Journal of Micromechanics and Microengineering, 2009, **19**, 075009

[35] Xie, H., et al., R*ecent advances in the study of Micro/Nano Robotics in France,* IARP Workship on Service Robotics and Nanorobotics, 2009

[36] Cercil, J., Powel, D., Vasquez, D., *Assembly and manipulation of micro devices – A state of the art survey* Robotics and Computer-Integrated Manufacturing, 2007, Vol. **23**. Issue 5: p. 580-588

[37] Cohn, M. B., et al., *Microassembly technology for MEMS, Micromachining and Microfabrication*, Internaiontal society for Optics and Photonics, 1998

[38] Nelson, B. J., Zhou, Y., and Vikramaditya, B., *Sensor – based microassembly of hybrid MEMS devices,* IEEE Control Systems, 1998, **18**.6: p. 35-45

[39] Demeester, P., et al., *Epitaxial lift-off and its applications,* Semiconductor Science and Technology, 1993, **8**, 6: 1124

[40] Schemer, J. J., et al., *Epitaxial Lift-Off for large area thin film III/V devices,* Physica Status Solidi (a), 2005, **202**, 4: p. 501-508

[41] Cheng, C.-W., et al., *Epitaxial lift-off process for gallium arsenide substrate resue of flexible electronics,* Nature Communications, 2013, **4**: 1577

[42] Singh, G. A., et al., *Batch transfer of microstructures using flip-chip solder bonding* Journal of Microelectromechanical Systems, 1999, Vol. **8**: p. 27-33

[43]   Maharbiz, M. M., Howe, R. T., and Pister, K. S., *Batch transfer assembly of micro-components onto surface and SOI MEMS*, Proceedings Transducer ' 90 Conference, Sendai, Japan, June 7-10, 1999

[44]   Tanida, K., et al, *Micro Cu Bump Interconnection on 3D Chip Stacking Technology*, Japanese Journal of Applied Physics, 2004, Vol. **43**, Part 1, Number 4B

[45]   Shuto, T., and Asano, T., *In situ observation of ultrasonic flip-chip bonding using high-speed camera,* Japanese Journal of Applied Physics, 2015, **54**, 030204

[46]   Cohn, M. B., and Fearing, R. S., *Self-Assembly in Microfabrication,* Seminar Presented too the Berkeley Sensor and Actuator Center, Nov. 22, 1992

[47]   Tien, J., Terfort, A., and Whitesides G. M., *Micro-fabrication through electrostatic self-assembly,* Langmuir, 1997, **13**(20): p. 5349-5355

[48]   Syms, R. R. A., *Rotational self-assembly of complex microstructures by the surface tension of glass,* Sensors and Actuators A, 1998, **65**: p. 238-243

[49]   Harsh, K. F., Bright, V. M., and Lee, Y. C., *Solder self-assembly for three-dimensional microelectromechanical systems,* Sensors and Actuators, 1999, **77**: p. 237-244

[50]   Clark, T. D., et al. *Template-directed self-assembly of 10-μm-sized hexagonal plates,* Journal of American Chemical Society, 2002, **124**: p. 5419-5426

[51]   Clark, T. D., et al., *Self-assembly of 10-μm-sized objects into ordered three-dimensional arrays,* Journal of American Chemical Society, 2010, **123**: p. 7677-7682

[52]   Wang, D. A., Ko, H. H., *Magnetic-assisted self-assembly of rectangular-shaped parts,* Sensors and Actuators A: Physical, 2009, **151**: p. 195-202

Chapter 2.   Transfer Printing

2.1 Transfer printing overview

Transfer printing in micro-manufacturing represents all techniques for deterministic assembly of micro and nanoscale objects from their processed site to a spatially organized foreign area of interest to serve the purpose of manufacturing with cost efficiency or unique functionalities and performances. Owing to the scalability of the soft lithography, various means of printing techniques in commercial level and the relatively low capital cost compared with other means of conventional manufacturing appeal the transfer printing in the scope of manufacturing efficiency [1-4]. Moreover, the transfer printing is a compelling alternative route of manufacturing technique, which complements the microassembly processes discussed in the previous chapter. Heterogeneous integration of diverse class of material has been an extreme challenge in micro-manufacturing since the means of deposition in conventional manufacturing involves rather complicated high-vacuum processes i.e. physical vapor deposition (PVD), radio-frequency (RF) power generated chemical vapor deposition (CVD) or extremely high thermal treatment for chemical processes such as thermal oxidation. While these techniques have served adequately until recently where the focus in the semiconductor industry have been in the enhancement of the computing power by improving the resolution attributed from the reduced pitch, the novel additive manufacturing routes have to emerge for the future semiconductor industry, which involves electronic devices with unprecedented form factor for innovative applications. In this scope, the transfer printing based micro-manufacturing technique is extremely appealing since the process merely relocates various forms of micro and nanoscale objects for convenient heterogeneous assembly of diverse class of materials. Additionally, the additive nature of the transfer printing benefits in the fabrication of complex three dimensional (3D) architectures, which can not only

reduce the overall occupational volume of the devices, but also can potentially augment applications in the microsystems.

One field of future electronics that have benefitted from the most recent advances in the transfer printing is in the flexible / stretchable electronics. The electronic industry has been domineered by silicon (Si) due to the accessibility of the material as well as its superb semiconducting properties. The progress in manufacturing techniques of Si and other inorganic materials such as deposition, etching and doping has allowed the rapid growth in information technology (IT) industry with one major limitation in its rigid, planar form factor. With development of conductive polymers (polypyrrole, polyaniline, and polyphenylene sulfide) in modern days, attempts to make transistors, organic thin film displays and memories have been pursued with little success due to the limited mobility of charge carriers in polymers when compared with the inorganic materials commonly used in semiconductor industry [5-7]. To overcome the drawbacks with the 2D and the rigid form factor while maintaining the outstanding charge mobility in the inorganic materials, heterogeneously integrated devices created from inorganic functional components encapsulated by the polymer structural materials have emerged. This heterogeneous integration allows electronic devices to effortlessly deform while exhibiting favorable characteristics such as mechanical shock tolerance, biocompatibility and biodegradability [8,9]. However, the viscoelastic behavior and the low tolerance in the thermal process of the polymers limit the direct adaptation of the material in the conventional micro-manufacturing processes, which is resolved by the transfer printing process. Here, the electronic devices are prepared through established micro-manufacturing processes on a rigid substrate, which is subsequently transfer printed onto a polymer substrate to create the stretchable /

deformable electronic devices, integrated circuit, optoelectronics, display, biosensors to list a few [10-18].

Microelectromechanical systems (MEMS) is another field of industry that has thrived from the maturing of the transfer printing process. MEMS evolved from the integrated circuit (IC) industry when sparse activities, such as anisotropic Si etching, which enabled sculpture of the three-dimensional (3D) features have investigatged in recent years [19]. Since, further development of the micromachining in both bulk and surface enabled pioneering activities in academics and industries to incorporate the 'mechanical' components in microscale devices such as cantilevers, membranes, channels and nozzles [20-23]. In order to achieve such mobile mechanical components in the microscale devices, the means of manipulation is limited, and often achieved by removal of sacrificial layer that lies beneath the desired component through either wet etching or gas-phase etching. Here, the complication of the sacrificial layer removal process resides, where the material compatibility should be conscientiously considered. Additionally, extreme caution is required to avoid phenomena called stiction where micromachined structure is permanently pulled down to the substrate due to the capillary forces during drying [24,25]. Limited means of etching, material compatibility as well as the potential risk of stiction constrains the fabrication of complex 3D architectures in microscale, which can otherwise, be purposeful for various applications. The inherent additive protocols of transfer printing can circumvent the challenges in the fabrication of suspended, mobile micro components in the MEMS device conveniently.

2.2 Fundamentals of transfer printing

2.2.1 Different schemes of transfer printing

Transfer printing technique is largely constituted of two major components, "ink" and "stamp". The ink refers to a material piece that is being transferred from their processed mother

substrate or donor substrate, and the stamp refers to the instrument or manipulator that plainly conducts the transfer and printing action which are further discussed in subsequent two sections respectively. As shown in the **Figure 2.1**, transfer printing process is broadly divided into three different methods termed additive transfer, subtractive transfer and deterministic transfer [26]. **Figure 2.1 (a)** represents additive transfer printing where the stamp is prepared and the ink material is directly deposited onto the stamp, which is followed with contacting against printing substrate for successful printing onto the receiving substrate. In order to selectively transfer print, the structured stamp is utilized where desired configuration is protruded in the stamp, such that during printing procedure, only the selected protruded region is making contact with the receiving substrate. On the contrary, subtractive transfer is when the donor substrate is deposited by ink material in planar 2D manner, which is selectively retrieved by the structured stamp (**Figure 2.1 (b)**). At this point, the stamp is "inked" just as in additive transfer printing, which can be either printed onto the receiving substrate, or directly utilize the patterned donor substrate in subsequent microfabrication process to fully construct the anticipated devices. The advantages of the additive and the subtractive transfer method reside in its mechanical patterning of the ink material that does not require complex high-vacuum instruments, any toxic and environment unfriendly chemicals as well as process compatibility with wide range of materials so long as the adhesion at the surface level is controllable. Therefore, the methods are commonly adopted in nanomaterials such as carbon nano tubes (CNT), quantum dots and other polymers that are relatively complex to develop meaningful patterning processes. Examples of the devices that exploits additive and subtractive transfer are included in references [27-31] and [32,33] respectively.

(a) Additive Transfer

1. Prepare stamp

   stamp

2. Deposit ink on stamp

   ink

3. Contact stamp; deliver ink structures to receiver substrates

   receiver

(b) Subtractive Transfer

1. Deposit continuous ink layer on donor substrate

   ink

   donor

2. Contact stamp; selectively retrieve ink structures from donor substrate

3. Use ink structures on stamp and/or donor substrate

   ink

(c) Deterministic Assembly

1. Prepare ink structures on a donor substrate

   ink

   donor

2. Contact stamp; selectively retrieve ink structures from donor

3. Contact stamp; deliver ink structures to receiver substrate

   receiver

Figure 2.1 Different schemes of transfer printing (a) additive transfer refers to the scheme where transferring material is directly deposited onto stamp, which is subsequently transferred onto target substrate (b) subtractive transfer is when the ink material is deposited onto donor substrate and selectively retrieve the ink material from the substrate through the structures of the stamp (c) deterministic assembly is when the ink is patterned into desired configuration, which is subsequently transfer printed by a stamp [26]

On the other hand, deterministic assembly is genuinely different from the other two above-mentioned methods in the view that the inks are first patterned on the donor substrate through conventional microfabrication techniques like photolithography (**Figure 2.1 (c)**). It is advantageous since the conventional micromanufacturing techniques are directly exploited for higher resolution inks preparation with drawbacks in relatively challenging protocols when lowering the adhesion of the ink with the substrate by means of sacrificial layer etching or

surface modification. Once the inks are fully prepared, subsequent steps are analogous with the other two methods where the stamp is brought to contact with the ink for inking process, and subsequent printing procedures. Nonetheless, the all three types of transfer printing enable rapid delivery of material in sparse or dense layouts over large substrate area efficiently.

2.2.2 Retrievable objects for transfer printing

One of the two major constituents of the transfer printing are the material that is being transfer printed, which is commonly referred to as "inks". Unlike common conception where ink is in the liquid format for writing or inkjet printing, the terminology "inks" in transfer printing represents any state of material (often in solid state) with wide range of material classes in the form of various configuration and geometry. The inks generally exhibit low adhesion with the surface that they are processed on by either surface modification or micromachining processes for convenient retrieval during transfer printing process. The first method of surface modification is commonly achieved by treating the surface of the donor substrate with self-assembled monolayer (SAM) such as octadecyltrichlorosilane (ODTS) or dichlorodimethysilane (DDMS), which are commonly employed material for anti-stiction monolayer in MEMS industry owing to its close to zero work of adhesion (0.012 and 0.045 mJ/m^2 respectively) [34, 35]. While little adhesion to the substrate is a significant impediment in the perspective of micromachining since the deposited material is prone to delamination during post processes, it is extremely beneficial in the scope of transfer printing due to its convenience in manipulation. The incompatibility with the post micromachining processes, however, bounds the surface modification method to either additive or subtractive transfer printing where no further lithography or wet processes are required. The ink preparation through surface modification is commonly adopted for transfer printing of nanoscale materials such as colloidal quantum dots (cQD), and organic light-emitting devices (OLED) to list

a few [36-39]. **Figure 2.2** represents OLED ink preparation on silicon dioxide (SiO_2) substrate with subsequent transfer printing onto PEDOT:PSS coated ITO glass substrate.
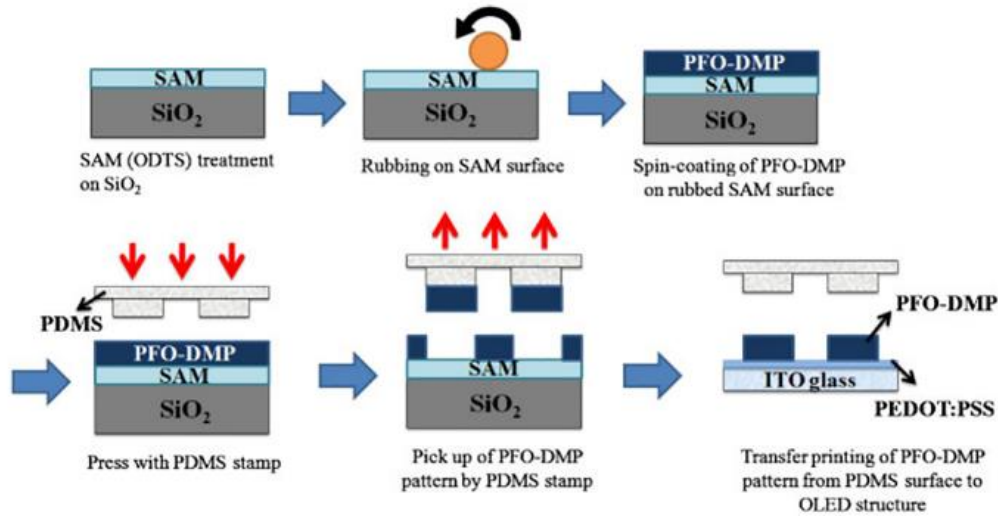
Figure 2.2 *Schematic illustration of the utilization of SAM for low surface energy to ink preparation and transfer printing of OLED [39].*

Another method of preparing an ink is by micromachining the ink material such that it is mechanically tethered to the donor substrate by means of sacrificial layer removal. The method is beneficial in the view of accessibility to the capital equipment commonly utilized for micromanufacturing processes such that extremely high resolution features with complex 2D geometry can be easily accomplished while finding suitable material for sacrificial layer for surface machining processes are rather challenging. Through mechanical tethering in conjunction with the sacrificial layer removal method, intrinsic materials, namely silicon (Si) and gold (Au), indium gallium nitride as well as complex fully integrated devices such as thin film transistors (TFTs), solar cells had been successfully transfer printed [40-47]. **Figure 2.3** represents an example of Si ink preparation schematics, which will be further discussed in subsequent chapters. In the presented case, the sacrificial layer is silicon dioxide (SiO_2), which is removed by hydrofluoric acid (HF). The SEM images reveal that after retrieval of the Si ink, the photoresist

(PR) anchors remain intact with the substrate. The phenomena imply that the delamination during retrieval occurs at the interface between the Si ink and the PR anchor, which further indicates that the Si ink utilized for transfer printing is free of contamination from PR anchoring. Regardless of the ink preparation procedures, either surface modification or mechanical anchoring and sacrificial layer removal schemes, the key in ink preparation is in to preparation of contamination and defect free ink material with minimal adhesion to the donor substrate. With proper ink preparation procedure, the materials which can be arranged to ink format is unbounded, as the materials for ink discovered until now is in wide range of class of material with various dimensions and configurations.
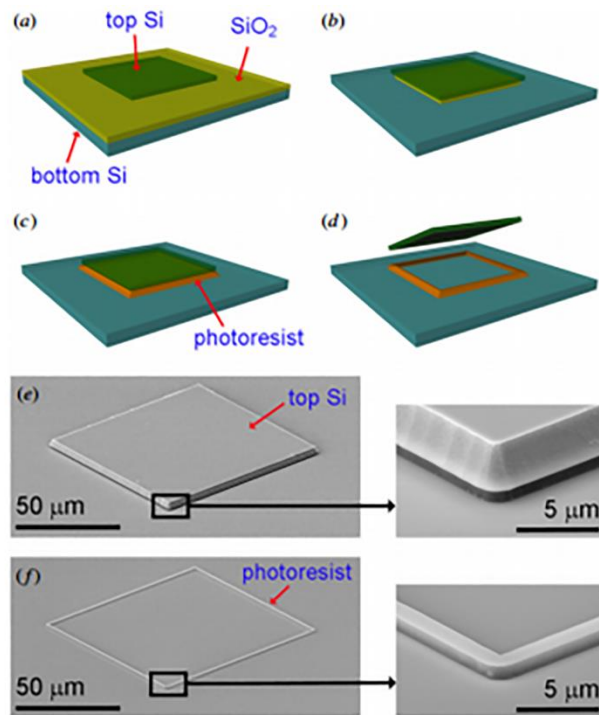
Figure 2.3 *Si ink fabrication scheme and SEM images of the ink before and after retrieval [41]. (a) Top device layer of SOI is patterned through micromachining, (b) Etching of exposed box oxide layer with slight undercut beneath the defined Si, (c) Photoresist filling of the undercut region and removal of SiO2 underneath the ink (d) retrieval of the Si ink (e) SEM image of the fully prepared Si ink, and (f) SEM image after removal of the Si ink. The PR anchors remain intact on the donor substrate.*

2.2.3 **Manipulators for transfer printing**

The domineering surface interaction associated with the remarkably high surface area to volume ratio in microscale objects augments the challenges in the manipulation of such minuscule objects. Pick-and-place through microgrippers, self-assembly and the batch processes are all recently developed methodologies of maneuvering the microscale objects, but they are hindered by complex instrumentation, process compatibility as discussed in the previous chapter [48-50]. In this context, polydimethysiloxane (PDMS), inspired from microcontact printing has emerged for the next generation manipulator [51]. The manipulator in transfer printing is commonly referred to as "stamp". The first of its kind was a simple flat surface, which kinetically controls the adhesion against contacting surfaces by exploiting the viscoelastic response of the elastomeric PDMS [52,53]. The energy release rate, which indicates the energy required to propagate a unit length of the crack, was employed to quantify the flat PDMS stamp. The experiment was conducted by simply rolling a PDMS coated rod on various angled ramps and about 10 times of the energy release rate difference between the adhesion on (fast rolling) and the off (slow rolling) states was discovered [54]. Subsequently, numerous attempts to enhance the adhesion on / off ratio, ranging from inflating membrane incorporated stamp, pedestal shaped stamp as well as angled post stamp, had been investigated, which either displays superb adhesion on / off ratio with complex form factor or insufficient enhancement of the adhesion tunability [55-58]. **Figure 2.4** represents optical and SEM images of an inflating membrane stamp, an angled post stamp array and a pedestal stamp respectively [56-58].
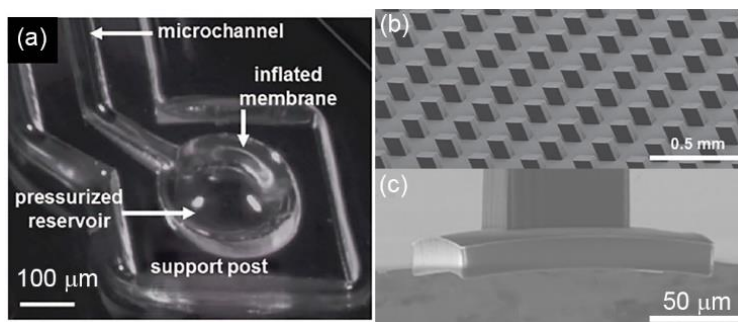
Figure 2.4 *Optical and SEM images of various stamp design for enhanced adhesion tunability. (a) optical image of inflating membrane stamp [56], (b) SEM image of array of angled stamp [58] and (c) SEM image of pedestal stamp [57]*

In this aspect, a PDMS stamp that features microtips on the surface of a square post with ~ 1 mm backing layer configuration was developed as shown in **Figure 2.5** [40]. **Figure 2.5 (a)** represents the SEM image of the PDMS stamp that features 4 microtips at 100 μm x 100 μm square post with its magnified view. The magnified view reveals that the tip is ~ 700 nm in radius. **Figure 2.5 (b)** is an SEM image and its respective schematics of the microtip stamp upon high preload prior to rapid retrieval from the donor substrate, which shows full collapsing of the microtip stamps such that close to ~ 80% of the microtip stamp surface is conformally contacting with the ink. In contrast, once the ink is retrieved from the donor substrate and adhered to the microtip stamp, with high retraction speed, the stamp experiences negligible load since the ink and the stamp is suspended in air. In such situation, the microtips recover their original shape, as shown in **Figure 2.5 (c)**, in which case, the contact area between the retrieved ink and the microtip stamp is drastically reduced as shown in the zoom in view as well as its schematics. The manuscript describes that the contact area in such situation is ~ 0.07%, which shows ~ 1,000 times of the difference in contact area by merely employing the microtips on the surface of the flat PDMS stamp. The hugely different contact area is directly reflected in the contrast of the adhesion, but not limited since the contact area difference doesn't incorporate the viscoelastic effect in the

process. Hence, the adhesion difference is greater than what is estimated from the mere contact area difference.
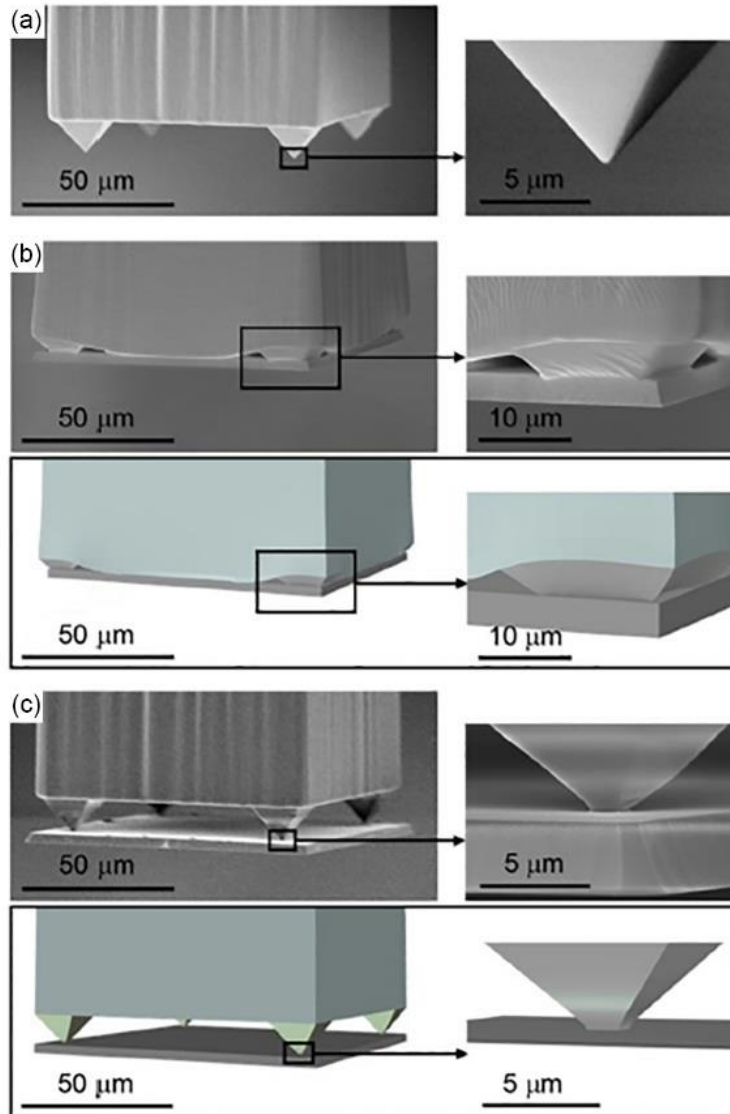
Figure 2.5 *SEM images and schematics of a PDMS stamp that features four microtips at each corner of the 100 μm by 100 μm surface. (a) SEM image of the microtip stamp with its magnified view (b) full collapsing of the microtip upon preload and its schematics (c) SEM image and the schematics of the microtip stamp once the microtips are restored due to the removal of the preload [40]*

The direct comparison of the pull off force between the microtip stamp and flat surface stamp, which are both made of PDMS, are presented in **Figure 2.6 (a)** and **Figure 2.6 (b)** respectively.

While the absolute value of the pull-off force from the microtip stamp ~ 80% when compared with the flat PDMS stamp, the crucial aspect lies in the difference between the adhesion on / off ratio, since the transfer printing technique thoroughly utilize this difference more extensively. Nonetheless, through microtip stamp, numerous 3D microstructures were demonstrated that can be exceedingly challenging otherwise as shown in **Figure 2.7 (a)** through **Figure 2.7 (f)** [40].
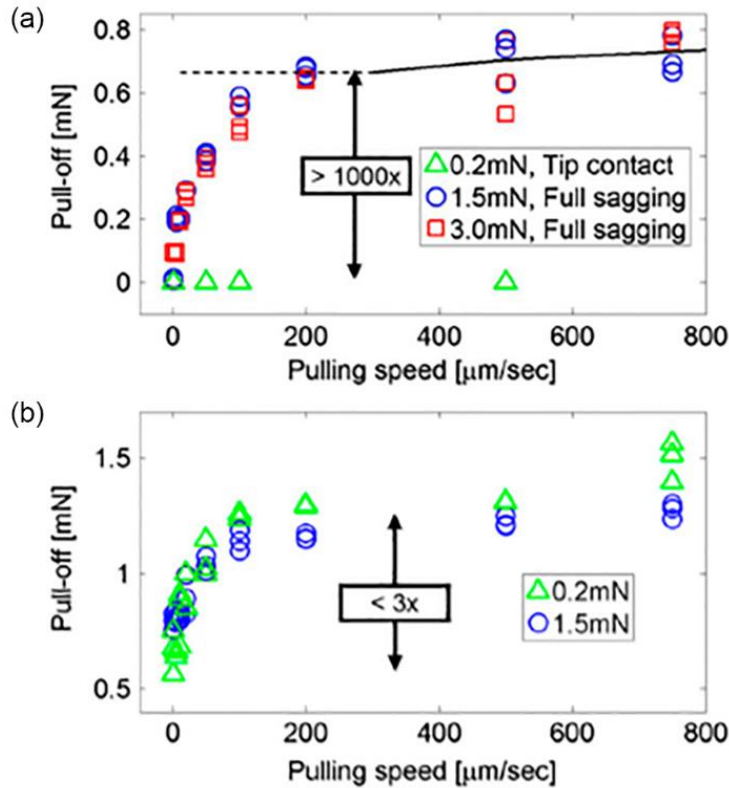
Figure 2.6 Adhesion measurement during printing and retrieval (a) microtip stamp (b) flat stamp [40]

However, the described microtip stamp yet exhibits limitations of utilization in the characteristic that it is only transferrable with discrete solid objects with dimensions that is seamlessly consistent with the stamp design to fully utilize the microtip structures. Therefore, development of the microtip stamp with versatile utility is critical for broader adaptation of the deterministic transfer printing techniques.
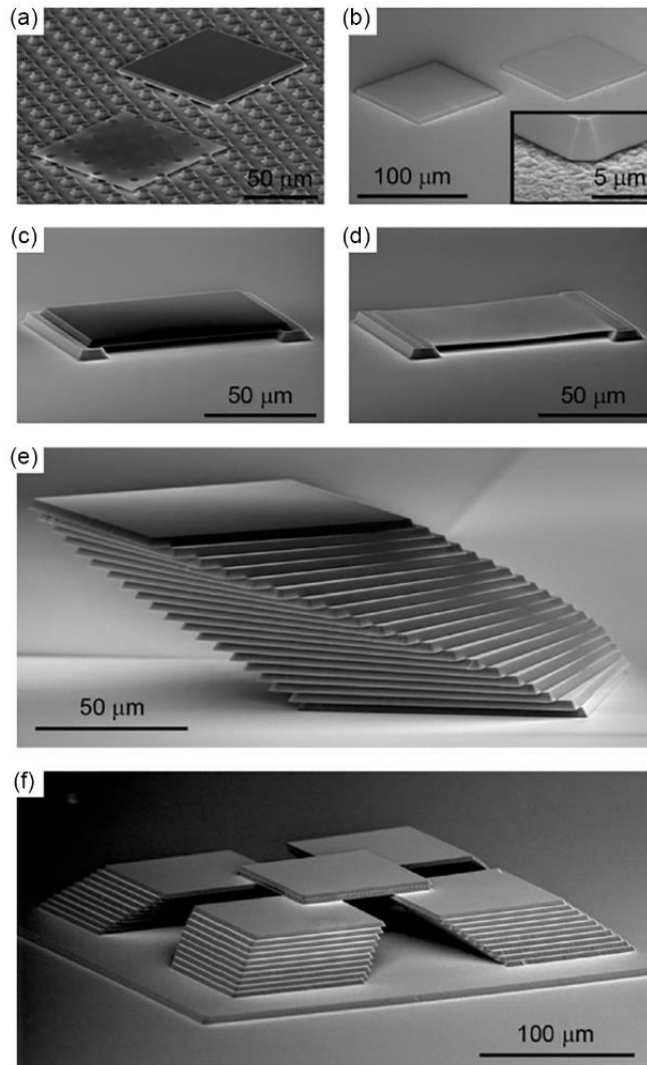
Figure 2.7 *Microscale 3D structures fabricated through transfer printing of 3 μm and 260 nm Si ink with 100 μm x 100 μm lateral dimension. (a) Both 3 μm and 260 nm printed on square island posts. The 260 nm ink appears transparent due to the physically diminishing thickness of the transfer printed Si ink (b) 3 μm printed on the rough surface (c) and (d) 3 μm and 260 nm platelet printed in suspended manner (e) multiple stacks of 3 μm platelet with incremental rotation and translations (f) multiple micro structure similar with that from (e) with pair of ink printed at the center [40]*

2.3 Development of a multiple microtip stamp

2.3.1 Design of a universal elastomeric microtip stamp with its performance estimation

Energy release rate or strain energy release rate is the fundamental quantitative concept in

fracture mechanics, which refers to the energy dissipated per unit of newly created surface during

fracture. In the view of energy balance, the energy supplied to a crack tip for growth must be balanced by the sum of energy dissipated due to the formation of new surfaces and other energy dissipated during process such as heat, or plasticity. Transfer printing is based on the competition between the interface between substrate - ink interface and ink – stamp interface and thus, understanding of this energy release rate is exceedingly important. Jian Wu and his colleagues first described stress intensity factor of the stamp and an ink object analytically as [59]

$$K_I = \frac{1}{\sqrt{1.07 \, ln\left(\frac{w_{stamp}}{w_{tip}}\right) - 0.42}} \frac{E'h_{tip}}{2} \sqrt{\frac{\pi}{cw_{spacing}(1 - 4c^2)}} \frac{1}{K(\sqrt{1 - 4c^2})} \qquad (2\text{-}1)$$

which was obtained from [60]. K term in **Equation (2-1)** is the complete elliptic integral of first kind, c represents the ½ percentage of the contact area between the stamp, E' is the plane-strain modulus given as $E' = \frac{E}{(1-v^2)}$ and a platelet and other geometrical terms $w_{microtip}$, w_{stamp}, $w_{spacing}$ and h_{tip} can be found in **Figure 2.8 (a)**. The stress intensity factor is converted to the energy release rate by $G = \frac{K_I^2}{E'}$, which generated the following equation for a single pair of microtip stamp [60]

$$G = \frac{1}{1.07 \, ln\left(\frac{w_{stamp}}{w_{tip}}\right) - 0.42} \frac{\pi E'h_{tip}^2}{8w_{spacing}} \frac{1}{c(1 - 4c^2)K^2(\sqrt{1 - 4c^2})} \qquad (2\text{-}2)$$

The **Equation (2-2)**, however is only applicable to the situation when the stamp has only a single pair of microtip. In order to convert to the multiple microtip stamp situation, the plane-strain modulus factor, E', needs to be modified according to the following relation [61]

$$E'_{periodic} = \frac{\pi^2}{8(1 + \frac{w_{microtip}}{w_{spacing}})^2 ln[sec\left(\frac{\pi}{2\left(1 + \frac{w_{microtip}}{w_{spacing}}\right)}\right)]} E' \qquad (2\text{-}3)$$

from which, the total energy release rate of the multiple microtip stamp becomes

$$G = \frac{1}{1.07\, ln\left(\frac{w_{stamp}}{w_{microtip}}\right) - 0.42} \times \frac{\pi^3 E' h_{tip}^2}{8 w_{stamp}} \times \frac{1}{c(1 - 4c^2)K^2(\sqrt{1 - 4c^2})}$$

$$\times \frac{1}{8\left(1 + \frac{w_{microtip}}{w_{stamp}}\right)^2 ln\left[sec\left(\frac{\pi}{2\left(1 + \frac{w_{microtip}}{w_{stamp}}\right)}\right)\right]} \qquad (2\text{-}4)$$

With **Equation (2-4)** established, the $w_{microtip}$, $w_{spacing}$ and w_{stamp} dimensions of the multiple

microtip stamp is determined to be 12 μm, 48 μm and 400 μm respectively, which yields ~ 5 J/m²

of the energy release rate. In addition to the energy release rate analysis, the relationship between

the microtip size and the spacing is critical because in order to display high adhesion on / off ratio,

the elastic restoring force should overcome the work of adhesion between the stamp and the

retrieved ink. A minimum height for a microtip, h_{min}, with a given separation and microtip size

has recently been determined as [40]

$$h_{min} = \sqrt{\frac{w_{spacing}\gamma}{E'}\left[3.04\, ln\left(\frac{w_{spacing}E'}{\gamma tan^2\left(\frac{\pi}{2}\right)}\right) - 11.5\right]} \qquad (2\text{-}5)$$

where γ represents the work of adhesion. The equation yields h_{min} of 6.6 μm ($E \approx 1.8$ MPa [62],

$v \approx 0.5$ and $\gamma \approx 155$ mJ/m² [63]), which is marginally shorter than our $h_{tip} \approx 8.1$ μm microtip

heights formed through anisotropic etching of the [100] Si substrate with potassium hydroxide

(KOH).
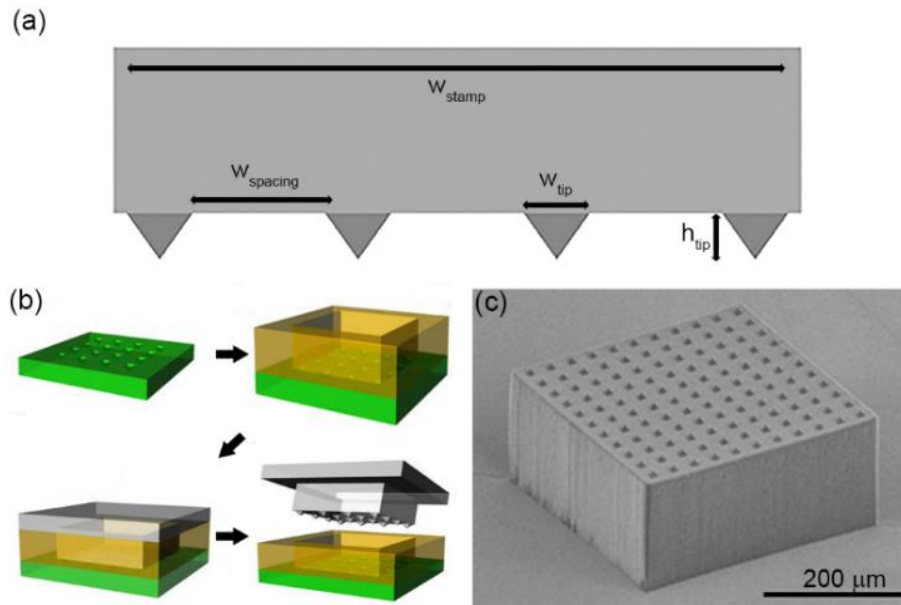
Figure 2.8 *(a) side view schematic illustration of the microtip stamp and geometrical terms (b) multiple microtip stamp fabrication flow (c) SEM image of the microtip stamp [41]*

2.3.2 **Multiple microtip stamp preparation protocols and its performance characterization**

With all the analytical characterization approximation, the elastomeric multiple microtip stamp was fabricated as depicted in **Figure 2.8 (b)**. The microtips were generated on [100] Si substrate (green) utilizing KOH anisotropic etching, which is predetermined by the crystal structure of the Si wafer. Subsequently, the square cavity was formed through SU-8 negative photoresist (yellow), which is commonly used as a structural material in microfabrication. The negative template was coated with trichlorosilane in desiccator prior to PDMS molding, which facilitates the demolding of the fully cured PDMS stamp. **Figure 2.8 (c)** is the SEM of the PDMS multiple microtip stamp after full fabrication, which exhibits 400 μm by 400 μm square post and 121 microtips with tip base size of 12 μm by 12 μm and tip to tip spacing of 36 μm. Additionally, PDMS being a transparent material, it is easily visible when the microtip initiates to contact the ink material, and whether they are fully collapsed or not, by optical microscope due to the small deformed region next to the tips. The versatility of this multiple microtip stamp was confirmed through pull off force measurement with respect to different radius of silicon disk. **Figure 2.9 (a)**

depicts the side and plane view of the stamp and a silicon disk respectively and **Figure 2.9 (b)** represents the obtained pull-off force with respect to varying Si disk radius. The experiments were conducted at 200 μm/s retraction speed with sufficient relaxation time of 5 s prior to retrieval. The obtained data indicates that for r < 30 μm, the pull-off force as well as normalized pull-off force values are insignificant, while for r > 30 μm disks yielded pull-off / area values ranging from 3 x 10^4 to 6 x 10^4 N/m^2. Based on this trend, it was speculated that the minimum silicon unit lateral feature size, above which the unit is reliably retrieved using the presented multiple microtip stamp is about 30 μm or larger. It is worth to note that the plot in **Figure 2.9 (b)** may seem to depict increasing normalized pull-off force per area (unfilled triangle facing downwards), but the plot is due to the possible registration error where the microtips are making contact on the side of the ink instead of the top surface of the experimental setup.
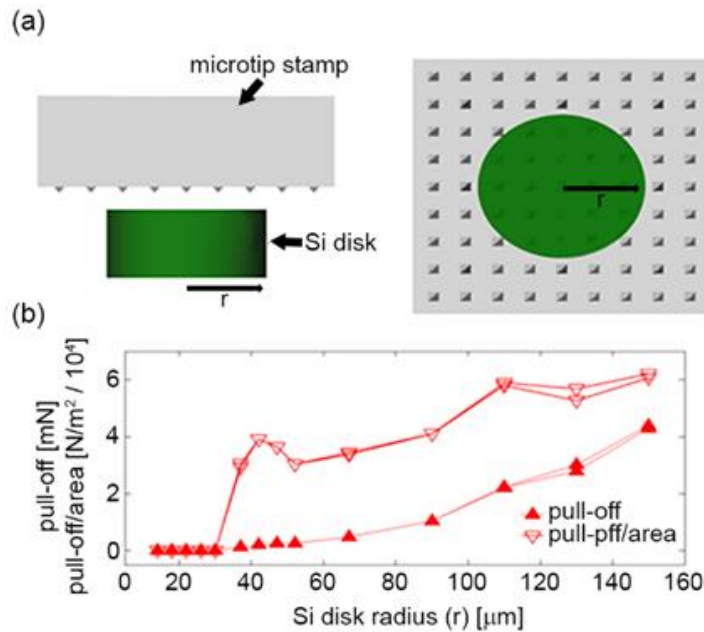
Figure 2.9 *Schematic illustration of the microtip stamp and a contact silicon disk to measure pull-off per contact area in a profile view and a plane view (a); (b) pull-off and pull-off per contact area against the silicon disk as a function of the radius [41]*

Furthermore, delicateness of the transfer printing process by exploiting the multiple microtip stamp was investigated by transfer printing extremely vulnerable photonic crystal structure since the process of retrieval and printing by the proposed multiple microtip stamp is purely mechanical process. **Figure 2.10 (a)** represents general schematics of the testing specimen where the delicate photonic crystal (pattern on ~ 3 µm Si platelet) is transfer printed and permanently joined at the suspended manner with ~ 50 µm circular pillars on four corners. **Figure 2.10 (b)** represents the magnified view of the photonic crystal where conical shapes are sparsely patterned in array with pitch of ~ 650 nm and **Figure 2.10 (c)** is an SEM image of the fully assembled photonic crystal table as depicted in **Figure 2.10 (a)** schematics. **Figure 2.10 (d)** is the reflection spectra measured by spectrometer (Bruker, Vertex 70 FTIR) coupled with a microscope (Bruker, Hyperion 1000) after coating the measuring surfaces with ~ 50 nm of gold (Au) through electron beam evaporator on both as in the donor substrate (prior to transfer printing and microassembly and after microassembly through the proposed multiple microtip stamp). The deposition of Au serves to facilitate the well-known surface-plasmon polaritonic (SPP) enhancement of the electromagnetic field for optical characterization and to prevent the incident light from transmitting into the photonic structures underneath, which can complicate reflectance measurement due to Fabry-Perot interferences caused by the thin-film silicon layer [65,66]. The reflectance spectra of the surfaces on donor and as assembled display similar trend over the entire measured wavelengths except for a small difference in reflectance value (~ 4%), which is speculated due to the suspended architecture of the assembled test specimen. Except for the overall shifted value in the assembled structure, both samples show SPP resonance peaks at 0.75 µm and 1.1 µm, which advocates the non-destructive process of mechanical transfer printing processes even with delicate structures like photonic crystal [41].
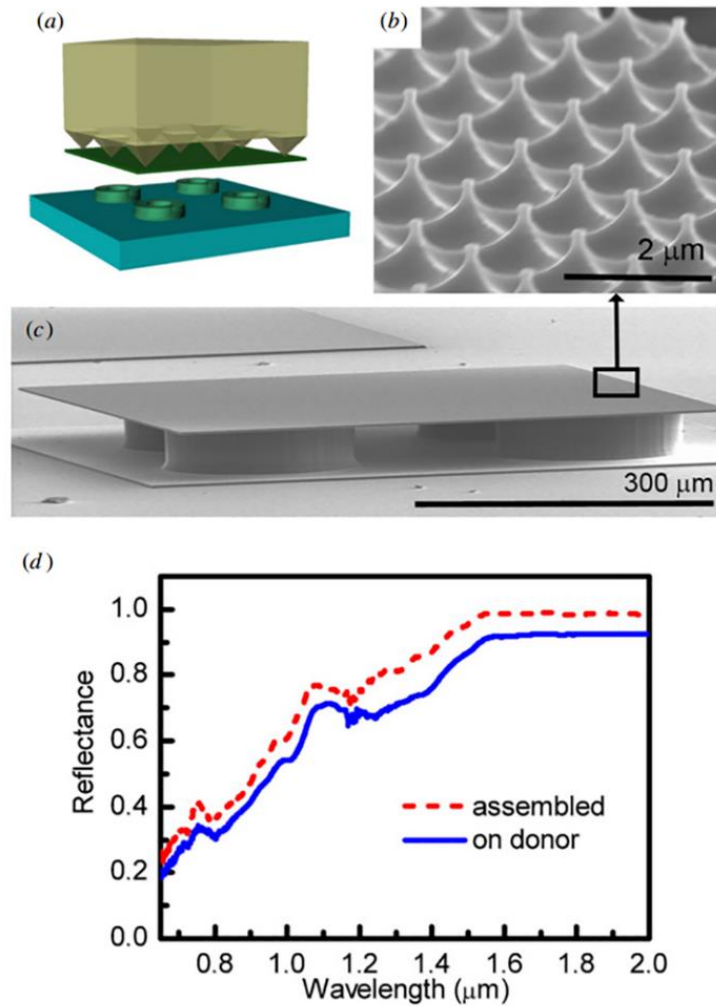
Figure 2.10 *An illustration of micro-masonry of a silicon photonic surface and four silicon rings (a) and SEM images of the nanostructures on the photonic surface (b) and the assembled silicon photonic surface on four silicon rings (c); (d) Reflectance spectrum plots of the photonic surface before and after assembly [41].*

2.4 **References**

[1]   Xia, Y., and Whitesides, G. M., *Soft Lithography,* Angewandte Chemie International Edition, 1998, Vol. **37**, Issue 5: p. 550-575

[2]   Xia, Y., and Whitesides, G. M., *Soft Lithography,* Annual Review of Material Science, 1998, Vol. **28**: p. 153-184

[3]   Rogers, J. A., and Nuzzo, R. G., *Recent progress in soft lithography*, Materials today, 2005, **8.2**: p. 50-56

[4]   Menard, E., et al., *Micro- and Nanopatterning Techniques for Organic Electronic and Optoelectronic Systems*, Chemical Reviews, 2007, **4**, 107: p. 1117-1160

[5]   Sundar, V. C., et al., *Elastomeric transistor stamps: reversible probing of charge transport in organic crystals.* Science, 2004. **303**(5664):p.1644-1646.

[6]   Rogers, J. A., *Electronics: Toward paperlike displays.* Science, 2001. **291**(5508): p. 1502-1503.

[7]   *Guizzo, E.,* Organic memory gains momentum. Spectrum, IEEE, 2004. **41**(4):p. 17-18.

[8]   Miyajima, H., et al. *A durable, shock-resistance electromagnetic optical scanner with polyimide-based hinges*. Microelectromechanical Systems, Journal of, 2001. **10**(3): p.418-424.

[9]   Aramani, D. and C. Liu, *Microfabrication technology for polycaprolactone, a aiodegraadable polymer.* Journal of Micromechanics and Microengineering, 2004. Vol. **10**: p.80-84.

[10]   Kim, D.-H., et al. *Stretchable and foldable silicon integrated circuits*. Science, 2008. Vol. **320**: p. 507 – 511

[11]   Ko, H. C. et al. *A hemispherical electronic eye camera based on compressible silicon optoelectronics*. Nature, 2008. Vol. **454**: p 748-753

[12]   Kim, T.-I. et al. *Injectable, cellular-scale optoelectronics with applications for wireless optogenetics*. Scinece, 2013. Vol. **340**: p. 211-216

[13]   Park, J.-S. et al. *Flexible full color organic light-emitting diode display on polyimide plastic substrate driven by amorphous indium gallium zinc oxide thin-film transistors.* Applied Physics Letters, 2009. **95**, 013503

[14]   Zhou, L. et al. *All-organic active matrix flexible display*. Applied Physics Letters, 2006. **88**, 083502

[15]   Kim, D.-H. et al. *Epidermal Electronics*. Science, 2011. Vol. **333:** p. 838-843

[16]   Yeo. W.-H. et al. *Multifunctional epidermal electronics printed directly onto the skin*. Advanced Materials, 2013 **25**, 2773-2778

[17]   Kim, D.-H. et al. *Electronic sensor and actuator webs for large-area complex geometry cardiac mapping and therapy*. Proceedings of the National Academy of Science of the United States of America, 2012. Vol. **108,** 19910-19915

[18]   Kim. D.-H. et al. *Thin, flexible sensors and actuators as 'instrumented' surgical sutures for targeted wound monitoring and therapy.* Small, 2012. **8**, No. 21 3263-3268

[19]   Bean, K. E., *Anistropic etching of silicon.* IEEE Transaction on Electron Devices, 1978. **ED 25**: p. 1185-1193

[20]   Petersen, K. E., *Silicon as a mechanical material*. Proceedings of the IEEE, 1982. **70**(5): p. 420-457

[21]   Gabriel, K. J., *Microelectromechanical systems.* Proceedings of the IEEE, 1998. **86**(8): p. 1534-1535

[22]   Angell, J. B., Terry, S. C., and Barth, P. W. *Silicon micromechanical devices*. Scientific American, 1983. **248**: p. 44-55

[23]   Middelhoek, S., *Celebration of the tenth transducer conference: The past, present and future of transducer research and development.* Sensors and Actuators A: Physical, 2000. **82**(1-3): p. 2-23

[24]   Tas, N. et al. *Stiction in surface micromachining*. Journal of Micromechanics and Microengineering, 1996. **6**: p. 385-397

[25]   Khanna, V. K., *Adhesion-delamination phenomena at the surface and interfaces in microelectronics and MEMS structures and packaged devices*. Journal of Physics D: Applied Physics, 2011, **44**, 034004

[26]   Carlson, A., et al., *Transfer Printing Techniques for Materials Assmebly and Micro/Nanodevice Fabrication*. Advanced Materials, 2012, **24**: p. 5284-5318

[27]   Loo, Y.0-L., Willet, R. L., Baldwin, K. W. and Rogers, J. A. *Additive, nanoscale patterning of metal films with a stamp and a surface chemistry mediated transfer process: Applications in plastic electronics*. Applied Physics Letters, 2002, **81**, 562

[28]   Meitl, M. A., et al., *Solution Casting and Transfer Printing Single-Walled Carbon Nanotube Films*. Nano Letters, 2004, Vol **4,** No. 9: p. 1643-1647

[29]   Jiang, x., Chen, R., and Bent, S. F., *Spatial control over atomic layer deposition using microcontact-printed resists*. Surface & Coating Technology, 2006, **201**: p. 8799-8807

[30]   Suh, D., Choi, S.-J., and Lee, H. H., *Rigiflex Lithography for Nanostructure transfer.* Advanced Materials, 2005, **17**: p./ 1554-1560

[31]   Hines, d. R. et al., *Nanotransfer printing of organic and carbon nanotube thin-film transistors on plastic substrates*. Applied Physics Letters, 2005, **86**, 163101

[32] Rogers, J. A., and Lee, H. H. *Unconventional Nanopatterning Techniques and Applications*. Wiley & Sons, Inc, Hoboken, 2008

[33] Kim, J. K., et al., *Low-pressure detachment nanolithography*. Nanotechnology, 2006, Vol. **17**, No. 4

[34] Ashurst, W. R., et al. *Dichlorodimethysilane as an Anti-Stiction Monolayer for MEMS: A comparison to the Octadecyltricholosiane Self-Assembled Monolayer.* Journal of Microelectromechanical Systems, 2001 Vol. **10**: p. 41-49

[35] Maboudian, R., Ashurst, W. R., and Carraro, C., *Self-assembled monolayers as anti-stiction coatings for MEMS: characteristics and recent developments*, Sensors and Actuators, 2000, **82**: p. 219-223

[36] Kim, B. H., et al. *Multilayer Transfer Printing for Pixelated, Multicolor Quantum Dot Light-Emitting Diodes*, ACS Nano, 2016 **10**: p. 4920-4925

[37] Kim, T.-H., et al., *Bright and stable quantum dots and their applications in full-color displays*, MRS Bulletin, 2013, **38**, 09: p. 712-720

[38] Lee, S., Yoon, D., Choi, D. and Kim, T.-H., *Mechanical characterizations of high-quality quantum dot arrays via transfer printing*, Nanotechnology, 2013, **24**, 025702

[39] Noh, H. Y., et al., *Transfer Printing Method to Obtain Polarized Light emission in Organic Light-Emitting Device*, Japanese Journal of applied Physics, 2012, **51**, 06FJ03

[40] Kim, S., et al., *Microstructured elastomeric surfaces with reversible adhesion and examples of their use in deterministic assembly by transfer printing*. Proceedings of the National Academy of Sciences, 2010, **107.40**: p. 17095-17100

[41] Keum, H., et al., *Silicon micro-masonry using elastomeric stamps for three-dimensional microfabrication*, Journal of Micromechanics and Microengineering, 2012. Vol. **22**, 055018

[42] Oh, D.-W., et al., *Interfacial thermal conductance of transfer-printied metal films*. Advanced Materials, 2011, **23**, 5028

[43] Kim, H.-S, et al., *Unusual strategies for using indium gallium nitride grown on silicon (111) for solid-state lighting,* Proceedings of the National Academy of Science, 2011, **108.25**: p. 10072-10077

[44]   Yoon, J. et al., *Ultrathin silicon solar microcells for semitransparent, mechanically flexible and microconcetrator module designs*. Nature Materials, 2008, Vol. **7**: p. 907-915

[45]   Lee, K. J. et al., *Bendable Gan high electron mobility transistors on plastic substrates.* Journal of Applied Physics, 2006, **100**, 124507

[46]   Zhao, Y., et al., *Three dimensional metal pattern transfer for replica molded microstructures*. Applied Physics Letters, 2009, **94,** 023301

[47]   Lee, K. J. et al., *A Printable Form of Single-Crystalline Gallium nitride for Flexible Optoelectronic Systems.* Small, 2005, Vol. **1**, 12: p.1164-1168

[48]   Dechev, N., Cleghorn, W. L., and Mills. J. K., *Microassembly of 3-D microstructures using a compliant, passive microgripper*. Journal of Microelectromechanical Systems, 2004, **13.**2: p.176-189.

[49]   Fang, J., and Böhringer, K. F., *Wafer-level packaging based on uniquely orienting self-assembly (the DUO-SPASS processes).* Journal of Microelectromechanical Systems, 2006, **15**.3: p.531-540.

[50]   Shah, A., et al. *Surface-tension-driven self-alignment of microchips on black-silicon-based hybrid template in ambient air*. Journal of Microelectromechanical Systems, 2013, **22**.3: p.739-746.

[51]   Xia, Y., and Whitesides, G. N., *Extending microcontact printing as a microlithographic technique*. Langmuir, 1997, **13**.7: p.2059-2067

[52]   Robers, A. D. *Looking at rubber adhesion.* Rubber chemistry and Technology, 1979, **52**.1: p.23-42

[53]   Barquins, M., *Adherence, friction and wear of rubber-like materials.* Wear, 1992, **158**, 1-2: p. 87-117

[54]   Meitl, M. A., et al. *Transfer printing by kinetic control of adhesion to an elastomeric stamp*. Nature Materials, 2006, Vol. **5**: p.33-38

[55]   Song, S., and Sitti, M., *Soft Grippers Using Micro-Fibrillar Adhesives for Transfer printing,* 2014, **26**: p. 4901-4906

[56]   Carlson, A., et al. *Active, Programmable Elastomeric Surfaces with Tunable Adhesion for Deterministic Assembly by Transfer Printing*, Advanced Functional Materials, 2012, **22**: p. 4476-4484

[57]   Kim, S., et al. *Enhanced adhesion with pedestal-shaped elastomeric stamps for transfer printing*, Applied Physics Letters, 2012, **100**, 171909

[58]   Yang, S. Y., et al. *Elastomer Surfaces with Directionally Dependent Adhesion Strength and Their Use in Transfer Printing with Continuous Roll-to-Roll Applications*, Advanced Materials, 2012, **24**: p. 2117-2122

[59]   Wu, J., et al., *Mechanics of reversible adhesion*, Soft Matter, 2011, **7**, 8657

[60]   Tada, H., Paris, P. C., and Irwin, G. R., *The stress analysis of cracks.* Handbook, Del Research Corporation, 1973

[61]   Huang, Y. Y., et al., *Stamp Collapse in Soft Lithography*, Langmuir, 2005, **21**: p. 8058-8068

[62]   Kim, D.-H., et al., *Optimized structural designs for stretchable silicon integrated circuits,* Small, 2009, **5**.24: p. 2841-2847

[63]   Chaudhury, M. K., and Whitesides, G. M., *Direct Measurement of Interfacial Interactions between Semispherical Lenses and Flat Sheets of Poly(dimethysiloxane) and Their Chemical Derivatives*, Langmuir, 1991, **7**: p. 1013-1025

[64]   Feng, X., et al., *Competing fracture in kinetically controlled transfer printing,* Langmuir, 2007 **23**, 25: p. 12555-12560

[65]   Wurtz, G. A., and Zayats, A. V., *Optical Bistability in Nonlinear Surface-Plasmon Polaritonic Crystals*, Physical Review Letters, 2006, **97**, 057402

[66]   Hecht, E., *Optics,* 2001, Wesley, San Francisco, CA

Chapter 3. Micro-Lego

3.1 Micro-Lego overview

While monolithic microfabrication has been quite successful in the manufacturing of microsystems such as integrated circuit (IC) and microelectromechanical systems, continued innovation towards 3D architectures and heterogeneous integration have been limited, which would otherwise enable enhancements in performance and novel functionalities of microsystems [1,2]. Associated challenges originate from layer-by-layer thin film processing on a single substrate and dissimilar nature of materials that my need different techniques to process. Consequently, 3D heterogeneous integration often requires independent fabrication of constituents followed by microassembly rather than monolithic microfabrication. In this context, transfer printing has emerged as a method that utilizes highly reversible surface adhesion of a polymeric stamp to deterministically transfer microscale solid objects called "inks" [3,4]. The ability to transfer inks from a donor substrate where inks are grown and processed to a receiving substrate where inks are finally assembled reduces the complexity of micromanufacturing processes regarding heterogeneous material integration. Furthermore, previously reported micro-masonry, which relies on transfer printing demonstrates that after proper thermal processing, direct bonding between transferred silicon inks can be achieved, which may be sufficiently strong to produce various MEMS devices [6-8]. However, limited assembling material classes and quantitatively unknown interfacial characteristics between joined inks suppress broader adaptation of this transfer printing-based microassembly.

Here, we extend micro-masonry to an approach to assembling microsystems with four disparate classes of device-grade materials including Si (semiconductor), SiO_2 (dielectric), Au (metal) and epoxy-based SU-8 (polymer) at the microscale. We refer to this approach as 'micro-

Lego' due to the similarities to the commercial product, Lego, in the aspects of stacking and joining of different types of building blocks while at different scales. Four different materials are processed into inks, assembled into spatially organized 3D architectures via reversible adhesion-based transfer printing followed by thermal processing-based material joining as schematically depicted in **Figure 3.1**.
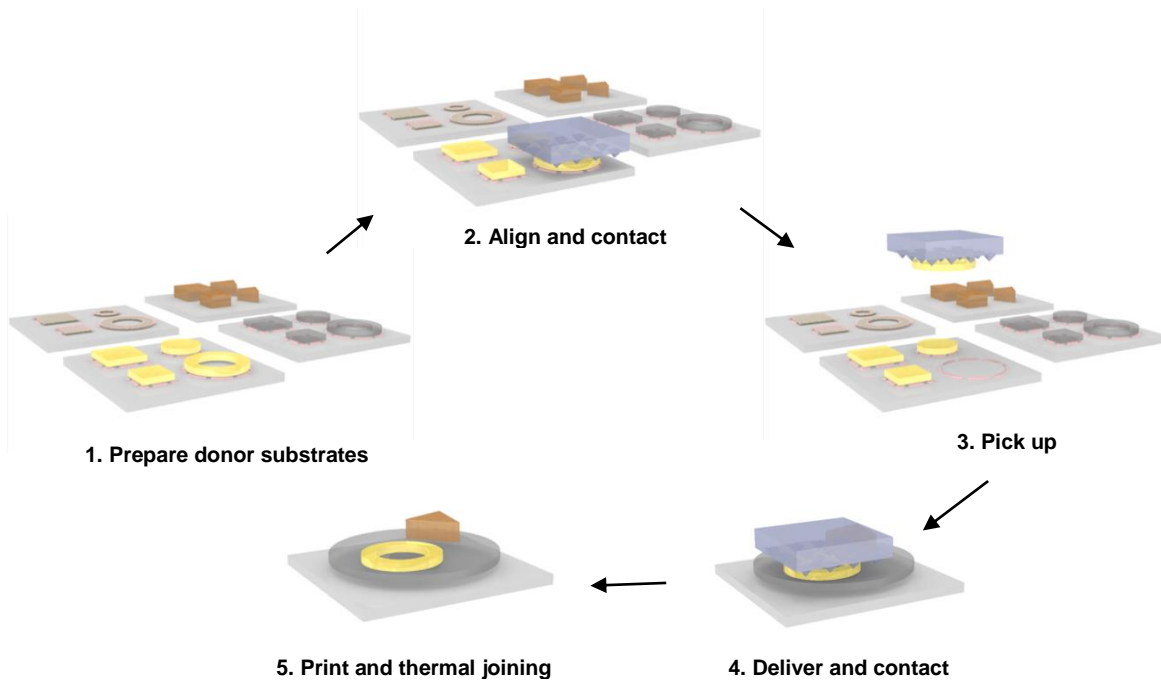
Figure 3.1 Schematics of general transfer printing procedure. Each individual inks are prepared on donor substrate and transferred onto receiver substrate through polymeric multiple microtip stamp, which is thermally processed for permanent joining [23]

Depending on the assembled material pairs, diverse joining mechanisms including fusion, eutectic, and adhesive bonding are explored at the microscale [9-12]. The joining strength for each joining pairs are examined utilizing blister tests not only for systematic comparison of joining methods of our different assembled material pairs but also for quantitative validation of the structural integrity enabled by micro-Lego [13,14]. In an effort to demonstrate 3D heterogeneous integration capabilities of micro-Lego, various 3D microstructures, a microtoroid resonator and a

radio frequency (RF) MEMS switch are assembled with Si, SiO$_2$, Au and SU-8. Furthermore, electrical connection between constituents on different steps of the RF MEMS switch is fulfilled to highlight 3D interconnection by micro-Lego. Theses 3D heterogeneous architectures are extremely challenging or inaccessible to reproduce via conventional monolithic microfabrication or other microassembly techniques such as those based on pic-and-place and self-assembly [15,16].

3.2 Protocols of ink preparation for micro-Lego process

3.2.1 Silicon inks

It is not overly exaggerating to say that the fundamentals of the electronic devices and the information technology (IT) are based on the emergence of the silicon industry. The abundance of the silicon as well as its mechanical stability has drawn much attention for the structural material for microelectromechanical (MEMS) devices while its unique electrical properties as a semiconducting material as well as the capability of tuning the mobility through doping demonstrated its capability in electronic devices [17-19]. Depending on the crystalline structure of the Si, the Si is categorized into single crystalline (often called monocrystalline silicon), polycrystalline and amorphous Si, where each exhibits their own advantages over the other forms of the Si. The single crystalline Si is the most touted material of choice for integrated circuit (IC) or other forms of miniaturized electronic devices owing to its consistency in electrical property when compared with polycrystalline or amorphous silicon where highly disordered grain boundaries may form either optical gap or heterojunction [20,21]. Although the single crystalline Si is advantageous, the process of manufacturing highly ordered with extreme purity Si involves intensely high thermal treatment, which confines the IC manufacturing processes [22]. In this aspect, polycrystalline Si or amorphous Si have been exploited in IC due to its relatively low process temperature through means of depositions such as low pressure chemical vapor deposition

(LPCVD), chemical vapor deposition (CVD), Plasma enhanced chemical vapor deposition (PECVD) or room temperature process such as PVD [22]. Therefore, deterministic assembly of single crystalline Si for device constituents would benefit the electrical performances by incorporating the superb electronic grade of Si for the IC purposes.

Figure 3.2 is a schematic process description of the single crystalline Si ink preparation [23]. The process begins with the careful selection of a silicon on insulator (SOI) wafer since the device layer dictates the electrical characteristics, i.e. resistivity as well as mechanical properties i.e. the thickness of the transfer printed Si ink (**Figure 3.2 (a)**). The buried oxide layer is recommended to ~ 1 μm thickness since the oxide layer is where the PR anchoring is formed, therefore, the thickness is required to be compatible with the thickness of the spin coated PR. Subsequently, the device layer is photolithographically patterned using reactive ion etching (RIE), or deep reactive ion etching (DRIE) if the device Si layer is relatively thick (**Figure 3.2 (b)**). PR is patterned that covers part of the top surface of the Si inks and extends out to the oxide layer and hard baked to promote the adhesion to selectively undercut the SiO_2 such that when removing the sacrificial layer of SiO_2, HF can penetrate flawlessly as well as to minimize the surface area of the PR anchors supporting with the ink (**Figure 3.2 (c)**). **Figure 3.2 (d)** represents the removal of exposed SiO_2 as well as small undercut underneath the Si inks and **Figure 3.2 (e)** is the formation of the PR anchors with inlet for the HF. Finally, the donor substrate with the Si ink array is accomplished with full removal of SiO_2 layer (**Figure 3.2 (f)**). With properly prepared donor substrate, the PR anchors remain adhered onto donor substrate after retrieval of the Si inks that requires no additional process to remove contaminants, which is in consistency with previously demonstrated Si ink [24].
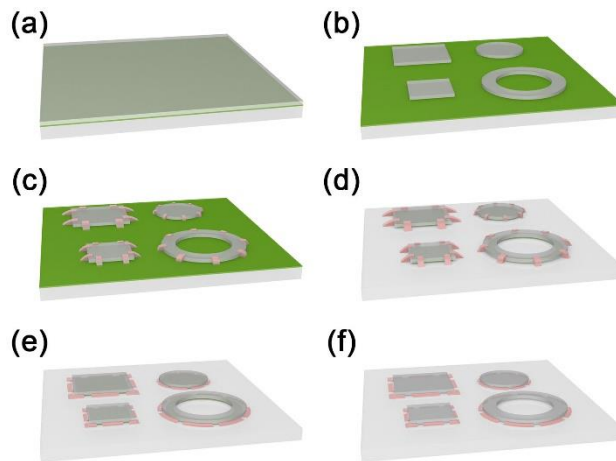
Figure 3.2 *Schematic process flow of Si ink fabrication scheme (a) SOI wafer is selectively chosen, (b) the device layer is patterned by photolithography, (c) masking of undercut layer for selective anchoring of PR (d) removal of buried oxide layer with small undercut beneath the Si inks where the PR is not covered, (e) removal of PR and filling of undercut region with PR for anchoring, (f) removal of all buried oxide layer underneath the Si ink [23]*

3.2.2 **Gold inks**

Gold is utilized in variety of field in electronics, wire bond, flip chip and off wafer interconnections, due to its corrosion resistance, ability to form metallurgical bonds by soldering or cold welding and ease of fabrication [25]. Additionally, the superb electrical and thermal conductivity of the material make Au to be a compelling candidate for the material of choice in electronic devices with an immense drawback in economic efficiency due to the high cost of the material [26]. With the growing industry of the IC and electronic devices, utilization of Au in every electronic device is not realistic, yet with its vital role in the modern electronic industry, and in applications where performance and reliability is more important than the cost, the gold will remain the technical and commercial material of choice [27]. In this view, the fundamental in implementation of Au in electronic devices is in the economic efficiency in the micro-processing technique, at which micro-Lego assembly of Au can benefit due to its deterministically additive nature of the process.

45
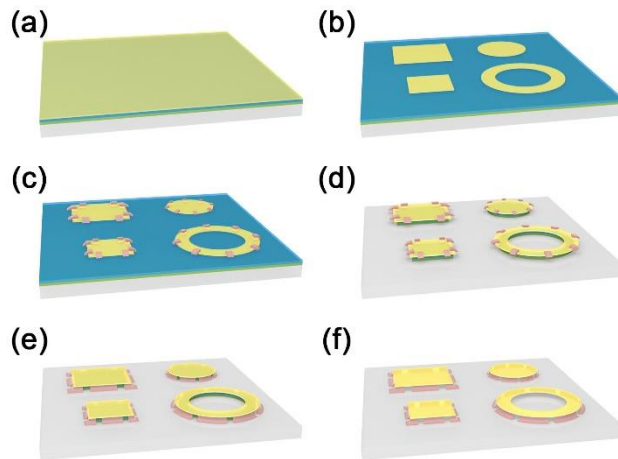
Figure 3.3 Schematic process flow of Au ink fabrication scheme (a) ~ 1 μm thermal oxide is grown on Si wafer followed with Ti and Au deposition, (b) Etch back patterning of Au, (c) PR patterning for selective undercut etching, (d) Removal of exposed box oxide layer and undercut of oxide layer beneath the patterned Si, (e) Formation of anchors within the undercut region, (f) Complete removal of box oxide layer resulting in the suspended Au layer tethered by PR anchors [23]

Figure 3.3 depicts the process of Au ink fabrication protocol. Similar with the Si ink fabrication scheme, SiO_2 is the material of choice for the sacrificial layer. **Figure 3.3 (a)** represents ~ 1 μm thermal oxide grown on a Si wafer with titanium (Ti) and Au deposition. Thin layer (~ 5 nm) of Ti adhesive layer is utilized in this process since Ti is etched out by HF during SiO_2 sacrificial layer removal step. The thickness of Au deposition requires a careful attention since the thickness of Au ink is solely determined during the Au deposition while the geometry and the lateral dimension can be configured during the photolithography patterning and etch back step as shown in **Figure 3.3 (b)**. Subsequently, the PR masking layer is formed for selective undercut etching (**Figure 3.3 (c)**), followed with sacrificial SiO_2 and Ti layer removal with undercut formation for PR anchors (**Figure 3.3 (d)**). The PR masking is removed and the PR anchors are filled in the undercut region (**Figure 3.3 (e)**), with full removal of the Ti and SiO_2 to complete the Au ink array formation in suspended structure for convenient retrieval.

3.2.3 **Silicon dioxide inks**

With its excellent stability in both water and at elevated temperature, outstanding electrical insulating performance, masking to common diffusing species, and capability of forming a nearly perfect electrical interface with its substrates in its native form, SiO_2 has demonstrated its vital role in semiconductor industry for past several decades [28.29]. In the heart of the semiconductor industry, two major device types comprehensively utilize the properties of SiO_2 are in capacitors, where SiO_2 is used for information storage in dynamic random-access memories (DRAMs) and in transistor gate dielectric in complementary metal-oxide semiconductor (CMOS) field-effect transistor (FET) logic devices [30]. There are two dominant methods of forming SiO_2 on the surface, thermal oxidation and deposition via various means of CVD (CVD, LPCVD, PECVD) or PVD (e-beam, dielectric sputter). The thermal growth of SiO_2 generally forms denser thin film when compared with other deposition methods, which is greatly beneficial especially in semiconductor industry with its reliability as well as higher breakdown voltage, the thermal growth method suffers from constraints such as high operating temperature, longer process time. Wet oxidation methods and high pressure oxidation, which both increase the concentration of oxidizer in the processing chamber to expedite the deposition process while lowering the process temperature, are both developed, with insufficient success due to the major constraints due to the surface where the oxidation occurs is limited by Si. Hence, other dielectric materials such as amorphous or crystalline tantalum pentoxide (Ta_2O_5), as an intermediate permittivity material, and on the crystalline, high-permittivity, complex oxide (Ba_xSr_{1-x})TiO_3, termed BST have been researched as a suitable replacing candidate for SiO_2, which is already in use as a dielectric in bulk capacitors [30]. Nonetheless, integration of thermally grown oxide for a functional device

component potentially benefit through its denser and high purity form factor, which inspired the prepare thermally grown SiO_2 into ink format for transfer printing and heterogeneous integration.

Figure 3.4 schematic depicts the process protocols for SiO_2 donor substrate preparation [23]. The process begins with an SOI wafer where the device layer is employed as a sacrificial layer material. As previously described in Si ink fabrication protocol, it is important to delicately select the device layer thickness since the layer serves not only as a sacrificial layer, but also as a seed layer where the thermal oxide is grown (**Figure 3.4 (a)**). For example, if the desired thickness of the SiO_2 ink is ~ 1 μm, approximately 500 nm of Si is consumed during formation of the SiO_2, which indicates that this consumed thickness must be considered along with the ~ 1 μm Si for sacrificial layer. Once the SOI wafer is carefully selected, the substrate is placed in furnace for the growth of the SiO_2 (**Figure 3.4 (b)**). Subsequently, the SiO_2 layer is patterned via lithography patterning and RIE etching followed with device Si layer removal through RIE (**Figure 3.4 (c)** and **Figure 3.4 (d)**). The PR is patterned, with small region overextending to tether the ink onto the box oxide layer (**Figure 3.4 (e)**), which is then placed inside XeF_2 gas phase etching instrument to finalize the thermally grown oxide into ink format where the inks are suspended by the PR anchor and tethered to the buried oxide layer (**Figure 3.4 (f)**). The isotropic nature of XeF_2 gas phase etching is adopted to remove the sacrificial Si layer, which produces minute etching of the SiO_2 ink due to inadequate selectivity between the two material. Therefore, the PR anchor which masks the SiO_2 ink is selected for the process, which introduces unwanted PR that requires post processing to remove after transfer printing.
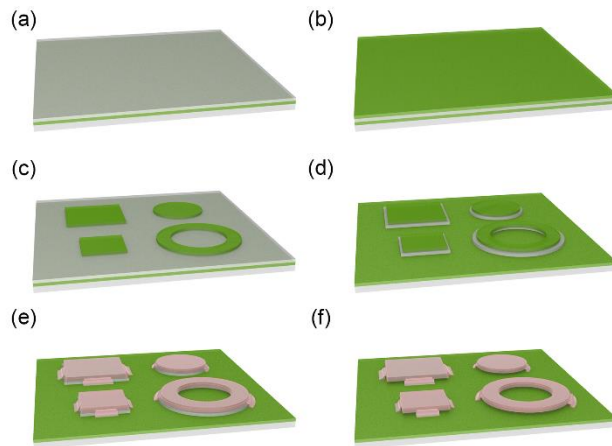
Figure 3.4 *Schematics of SiO$_2$ ink fabrication procedure. (a) SOI wafer is prepared with specific device layer thickness, (b) the device layer is thermally grown, (c) the thermally grown oxide is etched, (d) defining the Si sacrificial layer, (e) formation of the PR anchors and (f) removal of the Si sacrificial layer through XeF$_2$ etching [23]*

3.2.4 SU-8 photoresist inks

The lithography based micromanufacturing principally depend on PR since it is the main substance to form a patterned coating on a surface through activating the light-sensitive material in the PR. Unlike other commonly utilized PR, the SU-8 negative tone PR is also adopted for structural materials in MEMS owing to its exceptional mechanical stability as well as inertness to various solvents and other reactive chemicals once the SU-8 is fully cured [31]. Furthermore, the SU-8 can conveniently form comparatively thick layer of resist due to the very high concentration in solvents along with low optical absorption in near-Ultra Violet (UV) spectrum that can be exploited in other forms of manufacturing such as rapid prototyping of gearwheels, high luminosity lighting panels and photonic crystals [31 – 33]. Since the SU-8 is commonly registered by spin casting and the material adheres flawlessly with numerous substances, application of SU-8 is convenient in the view of surface micromachining. However, in the scope of broadening the materials available for micro-Lego process such that its utilitarian in micromanufacturing is broadened, SU-8 is processed to ink format as depicted in **Figure 3.5**.

The Si substrate is first coated with poly(methyl methacrylate) (PMMA), which forms thin layer serving as a sacrificial layer (**Figure 3.5 (a)**). The PMMA adopted in this process is 495 PMMA A4 resist from Microchem that yields ~ 200 nm of thickness when spun at 3000 rpm [34]. Once the PMMA is fully cured, SU-8 50 is spin coated over the PMMA deposited Si wafer (**Figure 3.5 (b)**), which is patterned and slightly cured through hard baking process (**Figure 3.5 (c)**). The hard baking duration and temperature is critical in the SU-8 ink fabrication since the degree of curing must reside in between the degree such that it can sustain in an acetone bath for a short period while preserving some of the epoxy chain for adhering after transfer printing. The substrate is then, placed in acetone bath for sufficient time to remove the PMMA layer, leaving the SU-8 inks adhere to the Si surface with mere surface interaction (**Figure 3.5 (d)**). During sacrificial layer removal step, it is critical to process with great care since the SU-8 inks don't feature PR anchors, therefore the inks are prone to displace if processed in vigorous environment.
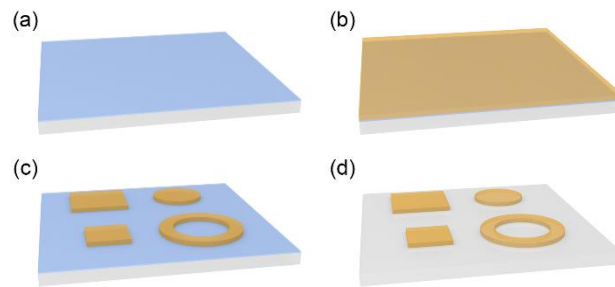
Figure 3.5 *Schematics of SU-8 ink fabrication. (a) PMMA sacrificial layer is spin coated on Si wafer, (b) SU-8 is spin coated on PMMA, (c) Defining of the SU-8 through photolithography and (d) removal of PMMA in acetone bath [23]*

3.3 Permanent joining schemes for heterogeneous material integration and their characterizations

3.3.1 Joining mechanisms for diverse material combinations and their joining parameters

As described in the introduction section of this chapter, the fundamental distinguishing factor of micro-Lego when compared with deterministic transfer printing techniques is in its heterogeneous material joining techniques without utilizing any adhesive layer to fully exploit the inherent material properties, which leads to lower electrical contact resistance and higher thermal conductivity at the joined interface. The joining schemes for cohesive and heterogeneous integration are typically adopted from wafer scale joining processes as listed in **Table 3.1**.

Table 3.1 *Diverse joining techniques utilized for different joining material combinations [23]*

Joining Materials		Joining Techniques
Si	Si, SiO$_2$	Fusion [35-42]
Si	Au	Eutectic [43-47]
Au	Au	Cold welding [48,49]
SU-8	Si, Au, SiO$_2$	Adhesive [50-52]

It is worthwhile to comment that although the joining schemes in micro-Lego are borrowed from wafer scale joining, the micro-Lego joining can be conducted without external pressure, which simplifies the micro-Lego as well as improves the capability of fabricating complex 3D suspended structures for the applications of MEMS devices. It is believed that this successful joining without external pressure is drawn from two major reasons; first, the microscale objects are domineered by the surface interaction rather than the body forces. Therefore, it is speculated that the surface interactions (Van der Waal's interaction) upon printing is sufficient to make intimate and conformal contact between the two joining materials. Secondly, the microscale inks are likely to contain less defects when compared with the wafer scale objects such as impurities

like dust, or possible angle misalignment, which also influences in the degree of contact at the interface.

Fusion bonding also known as direct bonding is employed for joining of Si and another Si or SiO_2 material, which is well-established and found its applications in not only preparation of an SOI wafer as well as other functional devices including pressure sensors, CMOS transistors in a very thin silicon film and static random access memory (SRAMs) [38-42]. When the two surfaces are brought to contact at room temperature, the two surfaces are initially bonded reversibly by either hydrogen bond or Van der Waals interaction as depicted in **Figure 3.6 (a)** and **Figure 3.6 (b)**. Subsequent thermal treatment at elevated temperature induces chemical reaction between the surface species of opposing wafer sides, which usually yield covalent irreversible bonds. The **Figure 3.6 (a)** represents the case of hydrophilic and **Figure 3.6 (b)** depicts the case of hydrophobic and their corresponding chemical equations are depicted in **Equation (3-1)** and **Equation (3-2)** [40].

$$-\underset{|}{\overset{|}{Si}}-OH \quad + \quad OH-\underset{|}{\overset{|}{Si}}- \quad \longrightarrow \quad -\underset{|}{\overset{|}{Si}}-O-\underset{|}{\overset{|}{Si}}- \quad + \quad H_2O \qquad (3\text{-}1)$$

$$-\underset{|}{\overset{|}{Si}}-H \quad + \quad H-\underset{|}{\overset{|}{Si}}- \quad \longrightarrow \quad -\underset{|}{\overset{|}{Si}}-\underset{|}{\overset{|}{Si}}- \quad + \quad H_2 \qquad (3\text{-}2)$$

25°C 800°C - 1000°C

(a)

silicon wafer

SiO2 →

OH OH OH OH OH OH OH OH OH OH
H2O H2O H2O H2O H2O H2O H2O
hydrogen bonds →
H2O H2O H2O H2O H2O H2O H2O
OH OH OH OH OH OH OH OH OH OH

SiO2 →

silicon wafer

silicon wafer

O O O O O O O O O O ← Si-O-Si bonds

silicon wafer

(b)

25°C > 600°C

silicon wafer

van der Waals interactions →
H H H H H H H H H H
H H H H H H H H H H

silicon wafer

silicon wafer

← Si-Si-bonds

silicon wafer

Figure 3.6 The bonding mechanism during fusion bonding [40] (a) Schematic drawing of the bonding of a two hydrophilic silicon surfaces at room temperature and at 800 ºC (b) Schematic drawing of the bonding of two hydrophobic silicon surfaces at room temperature and at 600 ºC

When joining Si – Au interface, eutectic bonding is employed to join the two material at compatibly lower temperature than that of the melting point of the Au [43-47]. Eutectic bonding forms eutectic metal alloy given specific composition and temperature is provided without transition phase of two-phase equilibrium. The low process temperature as well as the formation of alloy empowers the process significantly due to the process compatibility with even with some organic materials with high glass transition temperatures as well as disdain of the probability of reflow due to the formation of liquid phase at the interface. **Figure 3.7** is the phase diagram between Au and Si, which indicates the formation of eutectic alloy at ~ 363 ºC. The method can be found in the application of contact pad formation especially in MEMS devices where wedge bonding is commonly utilized for electrical interconnections.
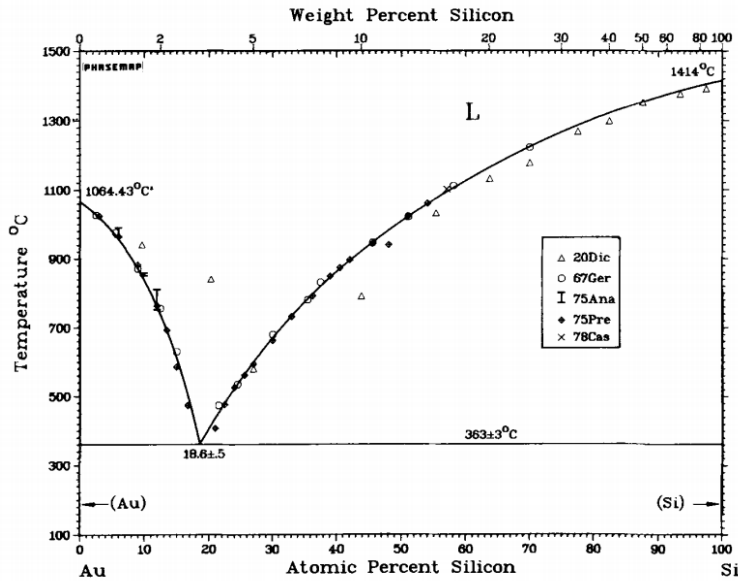
Figure 3.7 *Phase diagram between Au – Si [47]*

In the case of Au – Au bonding, cold welding is adopted to make strong irreversible joining at the interface. Cold welding refers to solid state welding process in which joining takes place without fusion at the interface, which is realized through high external pressure in ultra-high vacuum with atomic level clean surface in bulk scale. However, Ferguson and his colleague reported in 1991 that ductile Au can be cold welded at low pressure in room environment, which inspired to employ the cold welding for micro-Lego application [48]. Yang Lu recently demonstrated that the cold welding between gold nanowires with mechanical strength that is compatible with pure Au nanowire [49]. Additionally, gold and silver, silver and silver material pairs which were successful cold welded and it was reported that the formation of cold welding at nanowires are attributes of nanoscale sample dimensions, oriented-attachment mechanisms, as well as mechanically assisted surface atom diffusions. Although the exact physics of this cold welding in nanoscale at room condition is not profoundly established, owing to its adequate mechanical integrity as well as negligible electrical contact resistance at the joined interface

54

seemed plausible when directly adopted in micro-Lego process. Lastly, SU-8 is joined with all the aforementioned materials available for micro-Lego process by means of adhesive joining. SU-8 is an epoxy resin based negative PR, where the epoxy resins are directly employed to join the SU-8 with the other materials owing to its highly adhesive nature. **Table 2** represents the detailed protocol implemented in micro-Lego with corresponding material combination. Through the process parameters, complex 3D microscale architectures and functional devices with unique capability are formed, which will be dealt in after discussing the mechanical and electrical characterizations of the micro-Lego process.

Table 3.2 *Detailed description of joining conditions implemented for construction of 3D structures and devices*

Receiving material	Ink material	Joining Conditions
Si	Si	An Si ink is directly transfer printed onto a target Si surface and thermally processed in a furnace at 1000 °C for 10 min with 5 sec ramping.
Si	SiO$_2$	For high temperature (1000 °C) joining, a SiO$_2$ ink is directly printed onto a Si surface and thermally processed in a furnace at 1000 °C for 10 min with 5 sec ramping.
		For lower temperature (600 °C) joining, a SiO$_2$ ink is first transfer printed onto a Si substrate, which undergoes O$_2$ descuming process (O$_2$ 20 sccm, 150 mTorr, 200 W, 5 min) to remove photoresist (PR) that covers the SiO$_2$ ink. The ink is then, transfer printed onto an activated (O$_2$ 20 sccm, 150 mTorr, 100 W, 30 sec) Si surface. The substrate is then placed and thermally processed in a furnace at 600 °C for 10 min with 5 sec ramping.
Si	Au	The surface of the Si is cleaned with HF for removal of native oxide layer followed with transfer printing of an Au ink. The Au ink is transfer printed within short period of time after the HF treatment. The transfer printed sample is then placed in a furnace and thermally processed at 365 °C for 10 min with 5 sec ramping.

Table 3.2 (continued)

Receiving material	Ink material	Joining Conditions
Si	SU8	An SU8 ink is directly printed on a Si surface and thermally processed in a furnace at 150 °C for 10 min with 10 min ramping.
SiO$_2$	Si	Si ink is directly printed onto a SiO$_2$ surface and thermally processed in a furnace at 1000 °C for 10 min with 5 sec ramping.
Au	Au	An Au ink is printed onto a clean Au surface with a moderate pressuring for more intimate contact.
SU8	Si, Au, SiO$_2$	A desired ink is printed and thermally processed in a furnace at 150 °C for 10 min with 10 min ramping.

3.3.2 Mechanical joining strength for diverse material combinations

3.3.2.1 Blister test for material combination with silicon

The microsystems formed through micro-Lego displays excellent structural integrity due to the post irreversible joining process as listed in **Table 3.1**. Although all the joining schemes had been widely adopted in various fields of industry, confirmation of their mechanical stability is required to further highlight the uniqueness of the micro-Lego process. The blister test technique had been successfully demonstrated as a method of characterizing the adhesion of thin films formed on Si substrates [53,54]. The pressure inside hermetically sealed microcavity increases in a controlled manner using a syringe pump, which induces the delamination of a transfer printed and thermally joined ink from the rim structure on a receiving substrate at critical pressure that satisfies Griffith's fracture criterion [53]

$$G_c = G(p_c) = 0.625 p_c d_c \qquad\qquad (\textit{3-3})$$

where G_c is a material property termed critical energy release rate or toughness, which indicates the material's resistance to fracture along any given path. Provided that a joined ink delaminates along the joining interface, the corresponding G_c indicates the toughness of the joining.
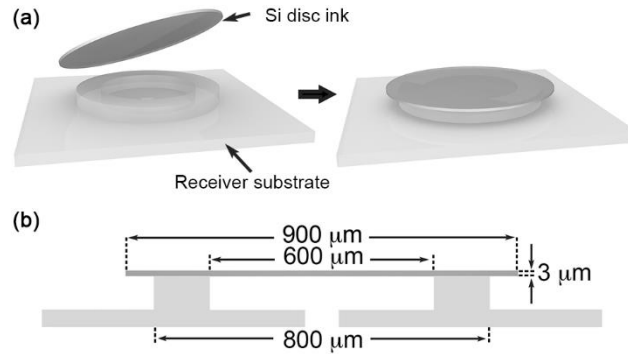
Figure 3.8 (a) schematics of microassembly of a Si - Si bonded blister test specimen, (b) Dimensions of the blister test specimen [23]

Figure 3.8 (a) and (b) shows the procedure to make a Si specimen for a blister test and its dimensions respectively. While maintaining the Si disc for the ink material, the receiver substrate in Figure 3.8 (a) is coated with SiO_2, Au and SU-8 to mimic the actual thermal joining process with various heterogeneously integrated interfaces. The description of various receiver substrate with different materials are shown in Figure 3.9. The parameters employed for this blister test were similar with that of listed in Table 3.2, as described in Table 3.3. The prepared blister test with various combination of materials are then placed in plastic packaging, which allows air to flow through. Upon failure, the critical pressure p_c was measured and the corresponding deflection d_c was obtained through simulation as shown in Figure 3.10 (a). By combining the experimentally obtained p_c and simulated d_c values, the critical energy release rate G_c can be formulated. The similar experiments were conducted with various combination of the materials and the obtained G_c values are plotted in Figure 3.10 (b).

Table 3.3 *Thermal processing conditions for blister test with Si inks [23]*

Receiving Surface Materials	Joining Conditions
Si	A Si ink is transfer printed and thermally processed in a furnace at 1000 °C for 10 min with 5 sec ramping.
SiO$_2$	Condition 1: A Si ink is transfer printed and thermally processed in a furnace at 1000 °C for 10 min with 5 sec ramping.
	Condition 2: A receiving SiO$_2$ surface is activated (O$_2$ 20 sccm, 150 mTorr, 100 W, 30 sec). Afterwards, a Si ink is transfer printed and thermally processed at 600 °C for 10 min with 5 sec ramping.
Au	Any native oxide on a Si ink is removed in a HF bath. The Si ink is transfer printed and thermally processed at 365 °C for 10 min with 5 sec ramping.
SU8	Condition 1: A Si ink is directly transfer printed and thermally processed in a furnace at 150 °C for 10 min with 10 min ramping.
	Condition 2: A SU8 receiving substrate is baked at 110 °C for 1 min followed with immersing in acetone bath for 1 min before thermal processing at 150 °C for 10 min with 10 min ramping.

The joining strengths presented in **Figure 3.10 (b)** indicate that even without the external loading, the toughness data for four pairs of materials similar to or higher than the toughness data for silicon wafer bonding measured elsewhere [35,36, 55]. Yet, it is worthwhile to mention that for the Si-Au blister test specimen, ~ 150kPa is applied during thermal processing to form hermetic sealing in the microcavity. Without the pressure, the bonding is formed at localized regions, which invalidates the application of **Equation (3-3)**. Nevertheless, all other Au inks assembled through transfer printing and thermal processing in this work are joined without such external pressure. Therefore, the measured joining strength at Si-Au interface is the upper bound of the actual joining strength. Also, the SU 8 and Si joining was conducted two different conditions, which refers to the

optimal situation (condition 1) and as conducted situation (condition 2). While the optimal situation displays ~ 3 times higher joining strength then as conducted situation, still ~ 1.4 J/m^2 joining strength of the as conducted situation is acceptable to guarantee the structural integrity of the microassembled structures and devices.
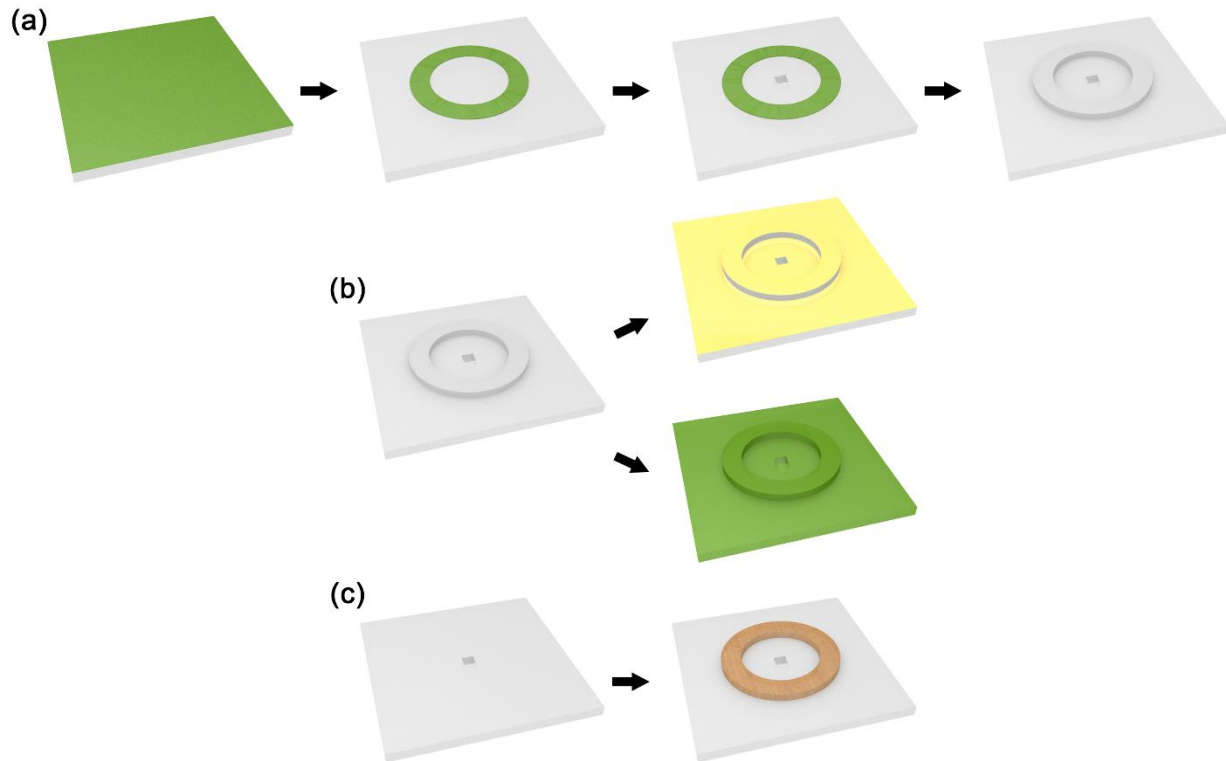
Figure 3.9 *Schematics description of receiver substrate for blister test specimens, which will subsequently joined with Si disc ink for heterogeneously integrated joining (a) Si receiver substrate sample (b) the exact receiver substrate is coated with Au (Au – Si, shown in top) and thermal treatment to grow SiO₂ (SiO₂ – Si, shown in bottom) and (d) simple formation of SU-8 ring post for SU-8 - Si [23]*
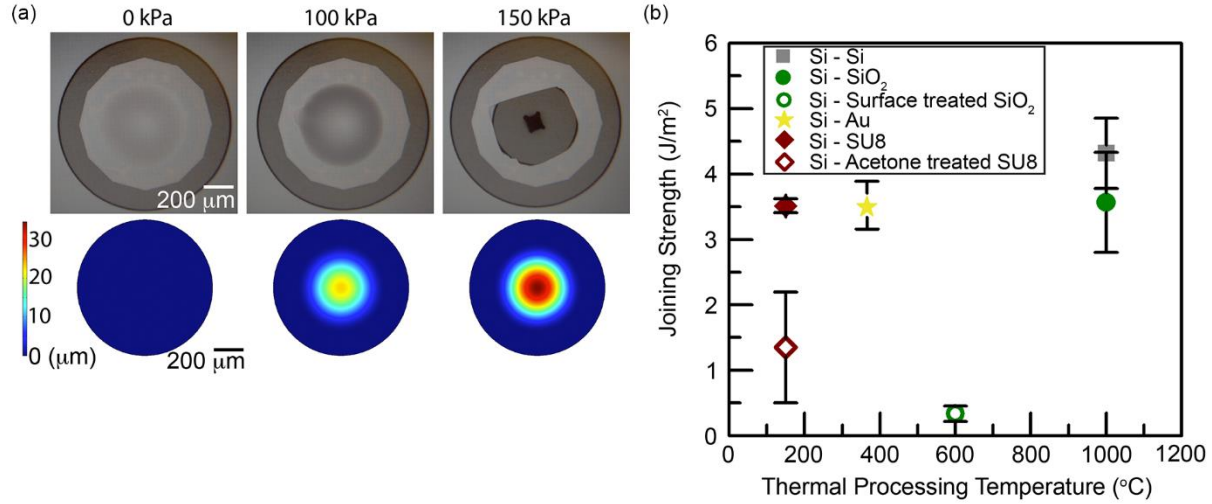
Figure 3.10 *(a) Optical image of the experimentally obtained p_c and its corresponding d_c with Si – Si blister test setup and (b) joining strength with respect to various thermal processing temperature [23]*

3.3.2.2   Cantilever nanoindenter test for SU-8 – SU-8 combination

In addition to the blister test to quantify the mechanical integrity of the micro-Lego assembled heterogeneous structures, bending test through nanoindenter was also conducted to examine the cohesively joined SU-8 and SU-8 interface. Although nanoindenter is an instrument that is commonly employed to characterize the hardness, modulus of elasticity, yield strength, fracture toughness, scratch hardness and wear properties, the method had been successfully adopted to characterize the mechanical deformation and corresponding behavior of RF MEMS switches [56,57]. Firstly, a SU-8 cantilever is formed through micro-Lego process (**Figure 3.11 (a)**) with dimensions of 100 μm by 100 μm spacer and 300 μm by 100 μm beam. **Figure 3.11 (b)** is a schematic of the SU-8 cantilever with notations *t, a* and *b*, each representing thickness of the beam, load distance from the fixed end and the length of the spacer respectively. Three individual tests were conducted through continuous stiffness measurement (CSM) technique with two experiments at *a* = 150 μm and the other at *a* = 100 μm and their corresponding data is plotted in

Figure 3.11 (c). The inset images in **Figure 3.11 (c)** represents before and after the nanoindentation experiment, where the specimen clearly shows indented mark in the top SU-8 cantilever beam. Upon observing the force versus displacement plot obtained through nanoindentation test, the plot can be categorized by three major regimes as noted by ①, ② and ③. Firstly, the SU-8 cantilever failed only when tested at $a = 100$ μm while the microassembled specimen survived when tested at $a = 150$ μm, which can infer that region ③ is where the cantilever failed. Secondly, region ② shows consistent slope independent with the load location, which is suspected to be the regime where the SU-8 initiates to yield and the indentation in the material starts to form. In this view, region ① is responsible for the behavior of the SU-8 cantilever upon load and its trend where the stiffness of the beam increases with reduced distance appears to be consistent with the intuition.
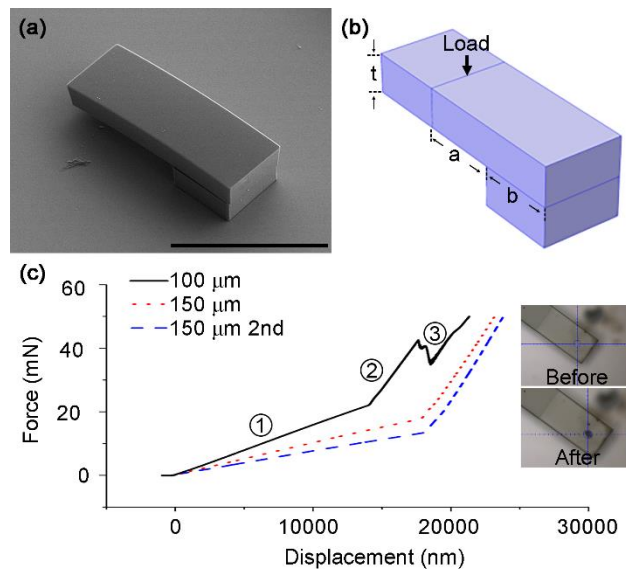
Figure 3.11 A cantilever specimen fabricated for nanoindenter test through micro-Lego and load versus displacement plot (a) SEM image of SU-8 cantilever beam on a Si substrate. The scale bar represents 100 μm (b) Schematics of the beam with notations. (c) Load versus displacement plot obtained through nanoindenter test. The inset represents before and after the nanoindenter test where after the testing, there exists indentation in the beam. ①, ② and ③ represent spring constant of the structure, stiffness from the indentation and failure of the structure respectively

Quantitative verification of the nanoindenter test is further conducted assuming the joined interface is a fixed with the load at arbitrary location based on beam theory [58]. The deflection of the beam (*d*) under the load (i.e. at x=a) is

$$d = \frac{Fa^3}{3EI}$$ (3-4)

where *a* is the load position, *E* is the elastic modulus and *I* is the area moment of inertia. The **Equation (3-4)** can be converted to obtain the spring constant *k* as shown in **Equation (3-5)**, which can be directly compared with the obtained nanoindenter data by examining the slope in the plot.

$$k = \frac{F}{d} = \frac{3EI}{a^3}$$ (3-5)

The elastic modulus of the SU-8 used to prepare the cantilever is approximated at 2.0 GPa in conjunction with other dimensions (*a* = 150 μm, *t* = 40 μm) yields the spring constant of ~ 948.15 N/m, which is close to the slope of the load versus displacement plot obtained from nanoindenter (~ 1005.8 N/m) assuming the small deformation of ~ 1 μm. The error between the experiment and the analytical value is attributed possible error in registration of the top cantilever beam as well as inaccurate location of the load. Nonetheless, the data from nanoindenter is consistent with the analytical solution, which validates the data obtained from the experiment.

To convert the nanoindetation data to energy release rate, the tensile stress concentrated at the back end of the interface needs to be quantified, which is approximated by finite element analysis (FEA) as shown in **Figure 3.12**. The **Figure 3.12 (a)** is the deformation plot in z direction (vertical as shown in the figure) to verify the validity of the FEA. The nanoindentation experiment results in ~ 17.9 μm of deflection with 17.985 mN of load at 150 μm from the fixed end, which is slightly different from the FEA analysis, which yields ~ 23 μm of deflection with consistent

geometrical values. This is mainly due to the unibody assumption when simulating through FEA, and this offset indicates that the energy release rate found is the upper bound of the SU-8 – SU-8 micro-Lego assembled structure.

Energy release rate for the failure due to the tensile stress normal to the plane of the crack is referred by mode I and its energy release rate is analytically given by

$$G = \frac{K_I^2}{E'}$$

(3-6)

where G refers to the energy release rate, K_I is the stress intensity factor for mode I and E' is the plane strain elastic modulus, which is function of elastic modulus and the Poisson ratio v as shown in **Equation (3-7)**.

$$E' = \frac{E}{(1 - v^2)}$$

(3-7)

Also, the stress intensity factor of an edge crack in a plate under tensile stress is given by

$$K_I = \sigma\sqrt{\pi c}\,[1.12 - 0.23\left(\frac{c}{b}\right) + 10.6\left(\frac{c}{b}\right)^2 - 21.7\left(\frac{c}{b}\right)^3 + 30.4\left(\frac{c}{b}\right)^4]$$

(3-8)

with σ, c and b refer to stress, crack length, width of the structure, respectively. In order to utilize the **Equation (3-8)**, two unknowns, σ and c, have to be found. It was assumed that the crack tip is located at the interface between the spacer and the beam at the opposite end with ~ 1 μm of length, which is the potential misalignment error when utilizing microtip PDMS stamp while FEA simulation was conducted to obtain ~ 2.2 x 10^7 N/m^2 for tensile stress as shown in **Figure 3.12 (b)** [60]. The FEA simulation in **Figure 3.12 (b)** is isolated plot that displays only the stress in z direction. In the FEA simulation, the stress was applied at ~ 100 μm distance from the fixed end since the failure of the cantilever only occurred during the nanoindentation experiment at 100 μm

location. The focus in FEA simulation is the tensile stress at the edge where the two micro-Lego assembled SU-8 begin to delaminate since other internal stress may cause deformation of the structure but not directly involved in the failure mechanism of the cantilever structure. Adopting the tensile stress value from FEA in conjunction with ~ 1 μm of crack length, the energy release rate is ~ 0.992 J/m^2, which closely matches previously demonstrated SU-8 and Si micro-Lego assembled joining strength as well as it is in the same order of magnitude of other previously reported wafer-scale bonded structures [23, 35-39].
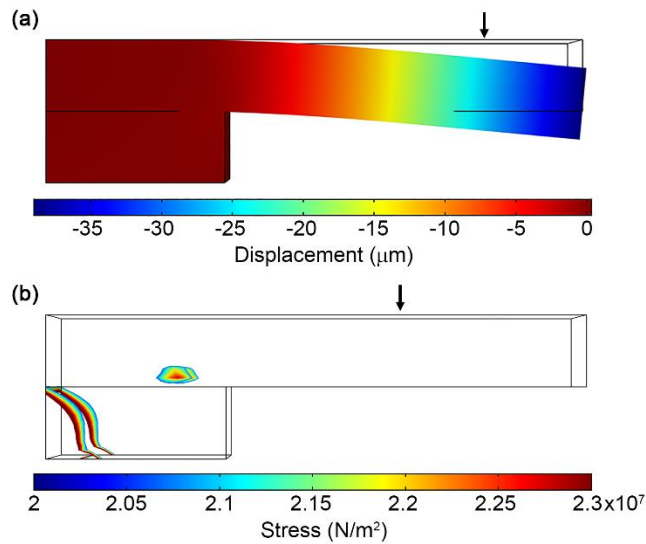
Figure 3.12 *FEA simulation of the nanoindenter experiment (a) displacement upon 17.985 mN and (b) zoom in view of the stress distribution upon 42.6 mN load. The arrows in the plot represent the location of the load*

3.3.3 Electrical contact resistance formed by Au – Au cold welding

As briefly mentioned previously, an impressive advantage of the micro-Lego is in its adhesiveless microassembly scheme that can fully utilize the joining material properties. An attempt to justify our claim is conducted, by investigating the contact resistance at the Au – Au cold weld joined interface as shown in **Figure 3.13**. **Figure 3.13 (a)** is the schematic of the specimen where two Au lines are formed via e-beam evaporation with thin chromium (Cr)

adhesive layer on thermally oxidized Si substrate. One Au line is continuous line which works as a reference line, and the other is discontinuous so that the two distinct lines can be bridged by micro-Lego processed Au ink.
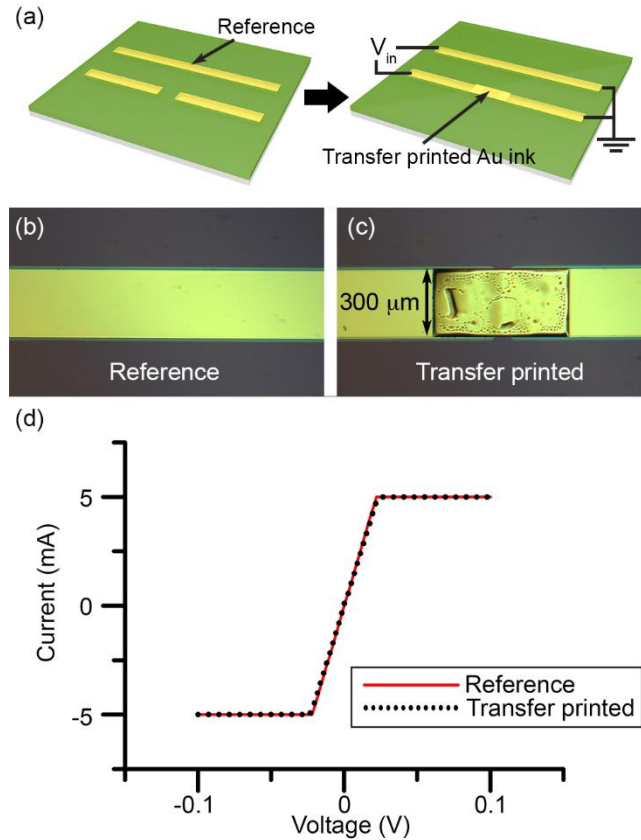
Figure 3.13 *Contact resistance of microassembled Au – Au interface. (a) Schematic of reference and assembled Au lines, (b) and (c) are optical images of a reference Au line fabricated through photolithography and a connected Au line with an assembled Au ink and (d) I-V curves of the two Au strips [23].*

The two Au lines are then placed in probe station to measure the current versus voltage plot. **Figure 3.13 (b)** and **Figure 3.13 (c)** are optical microscopic image of the reference line and transfer printed Au line and **Figure 3.13 (d)** represents the I-V curve in the probes station with compliance current set at -5 mA and 5 mA. As the plot demonstrates, the two measurements are in extreme congruence, which demonstrates that there's negligible contact resistance between the

Au – Au cold-welded interface. The methods of cold welding Au through micro-Lego can potentially find its applications in electrical wiring between two contact pads that are located in two different topologies.

3.3.4 Electrical contact resistance formed by Au – Si eutectic joining

While thermal conductivity transfer printed Au ink on Si substrate had been discovered, contact resistance between the transfer printed and irreversibly joined Au and Si surface has not be investigated yet [61]. In this aspect, the micro-Lego assembly of Au onto Si can be adopted in the formation of contact pads in MEMS devices provided that the interface contact resistances are negligible. A transmission line model (TLM), which makes a series of metal-semiconductor contacts spaced differently, is employed to measure the contact resistance of the micro-Lego assembled Au-Si specimen. The data obtained is further compared with vacuum deposited Cr / Au sample to for verification. **Figure 3.14** represents the SEM image of the TLM sample where two contact pads are spaced by 100, 200, 300 and 400 μm apart. The image is colorized to distinguish the Au, PR, SiO_2 and Si in the image, which are colored by yellow, red, brown and untouched respectively. The black rectangular are alignment marks for micro-Lego process, which doesn't serve any functionality in TLM measurement.
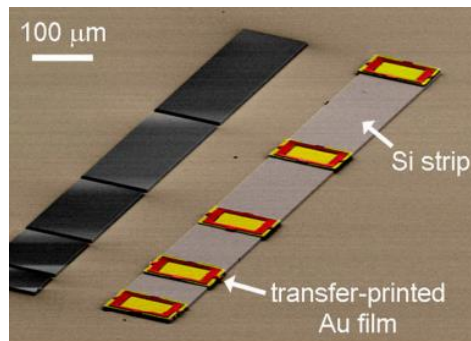
Figure 3.14 *SEM image of the TLM specimen, which is colorized to distinguish the different materials [43].*
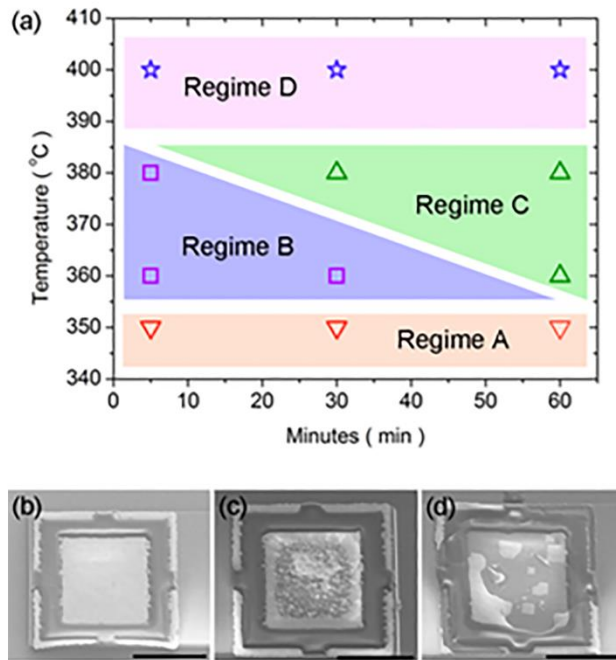
Figure 3.15 *(a) different parameters of temperature and duration combination experimented for eutectic joining with regimes division, (b) SEM image of the Regime A and Regime B, (c) SEM image of Regime C, (d) SEM image of Regime D. All scale bars in (b) – (d) represents 50 μm [43]*

Prior to the TLM measurement, proper joining protocols need to be developed since the irreversible joining of transfer printed Au film has not been fully discovered yet. Twelve different testing parameters with three different thermal treatment temperatures (350, 360, 380 and 400 ºC) and three different duration (5, 30 and 50 min) are tested as shown in **Figure 3.15 (a)**, where the samples are largely categorized by four different regimes (**Figure 3.15 (b)** through **Figure 3.15 (d)**). It came to our surprise that with excessive thermal treatment, the surface of the micro-Lego assembled Au (~ 400 nm) is ruptured and becomes ineffective since the Au membrane is extremely difficult to probe when serviced as a contact pad [43].
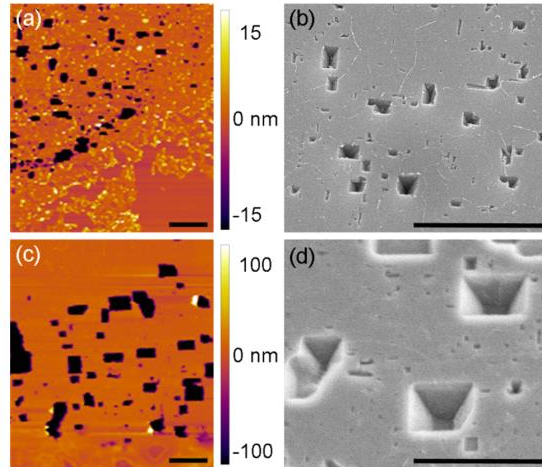
Figure 3.16 *AFM and SEM images of the surface after thermal treatment. Both measurements were conducted after completely removing Au by wet etching process. (a) and (b) represent the sample in regime A and B in* *Figure 3.15 (a), (c) and (d) represents sample from regime C in* *Figure 3.15 (a). All scale bars represent 2 μm [43].*

The surface morphology of unaltered (regime A and B in **Figure 3.15(a)**) and moderately dewetted surface (regime C in **Figure 3.15 (a)**) are further investigated by atomic force microscopy and SEM after etching Au with an iodine based wet etchant as shown in **Figure 3.16**. It is worthwhile to mention that the pits in found in the Si surface follows the pyramidal shape in the [100] wafer, which stems from the anisotropic nature of the crystalline Si wafer where the [111] plane has the highest atomic density, hence the slowest for migration of atoms [65]. The AFM and SEM images reveal that at elevated temperature and longer duration, higher degree of interdiffusion between Si and Au, which accompanies the surface dewetting of the Au film. The TLM measurement data is plotted in **Figure 17**, which lead to the contact resistance when the slope is extended to find y-intercept according to the **Equation (3-9)**.

$$R_T = 2R_C + \frac{R_{SH}d}{w}$$

(3-9)
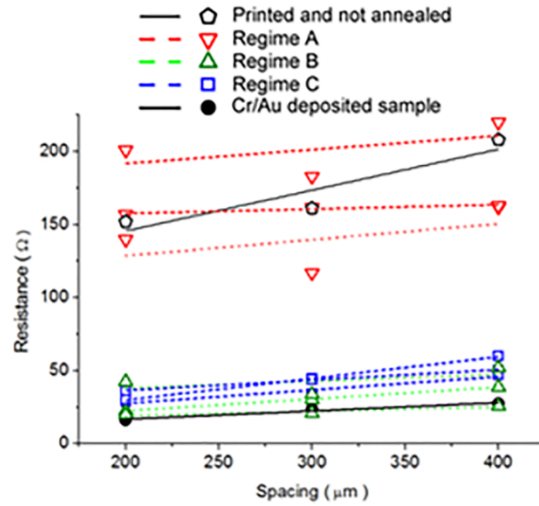
Figure 3.17 *TLM measurement of different regimes A through C in* **Figure 14 (a)** *with reference Cr / Au vacuum deposited sample [43].*

The variables R_T, R_C, R_{SH}, d and w represent total resistance, contact resistance, sheet resistance of Si, distance between two Au pads and width of the Au films. **Table 3.4** is the summary of contact resistances where the lower contact resistances are discovered when the joining protocols are at elevated temperature with longer duration, which is reasonable since with higher temperature and longer duration, the level of interaction will be higher. However, the surface morphology of the Au after thermal joining demands accommodation that leads us to conclude that the optimal process parameter is when Si and Au are joined at 360 ºC for 30 min of duration which is slightly higher than our control sample (5.37 Ω) but within the reasonable difference.

Table 3.4 *Contact resistance values (R_C, Ω) from* **Figure 3.17** *[43]*

Temperature (ºC)	Duration (min)		
	5	30	60
380	27.6	5.14	25.67
360	26.5	19.67	13.48
350	184.23	126.23	143.57

69

3.4 Applications of micro-Lego

3.4.1 Various microscale complex three dimensional structures

Bespeaks of the heterogeneously integrated four different class of material prepared in ink format; Si, SiO$_2$, Au and SU-8. When micro-Lego assembling the structures, multiple microtip proposed in previous chapter was employed as a stamp, which shows extremely high adhesion on / off ratio in dry manner [66]. **Figure 3.18 (a)** is named micro-teapot owing to its correlation with actual teapot. The structure is hollow inside and the bottom half is prepared by 50 μm thick rings while the top half is fabricated by 10 μm thick rings [66]. Likewise, **Figure 3.18 (b)** is prepared with 50 μm rings and a block with a 10 μm rings with slight offset to emphasize the capability of micro-Lego in tailoring suspended structure with modest contact area [66]. While **Figure 3.18 (a)** and **Figure 3.18 (b)** represent micro architectures formed through cohesive Si – Si fusion bonding, **Figure 3.18 (c)** through **Figure 3.18 (f)** depict heterogeneous material integration in microscale. **Figure 3.18 (c)** is microassembly of double stacked Si and SiO$_2$ rings with thicknesses 10 μm and 1 μm respectively. When joining the two-different class of material, due to the extremely thin thickness of the SiO$_2$, it is prone to buckle during thermal processing owing to the difference in thermal expansion coefficient. Therefore, making intimate and conformal contact to overcome this stress when printing, is vital for successful micro-Lego assembly [23]. **Figure 3.18 (d)** is multiple stack of Si disc and SU-8 block with thicknesses of 10 μm and 50 μm respectively. Due to the low temperature process of SU-8 adhesive joining protocol, the structure is prepared at relatively low temperature with drawback of alignment issues since the larger circular Si discs aren't transparent when precisely registering the subsequent SU-8. Nonetheless, such SU-8 and Si structures are extremely difficult to replicate in other means of microfabrication since spin casting of the SU-8 will fill the gap between the two Si discs [23].
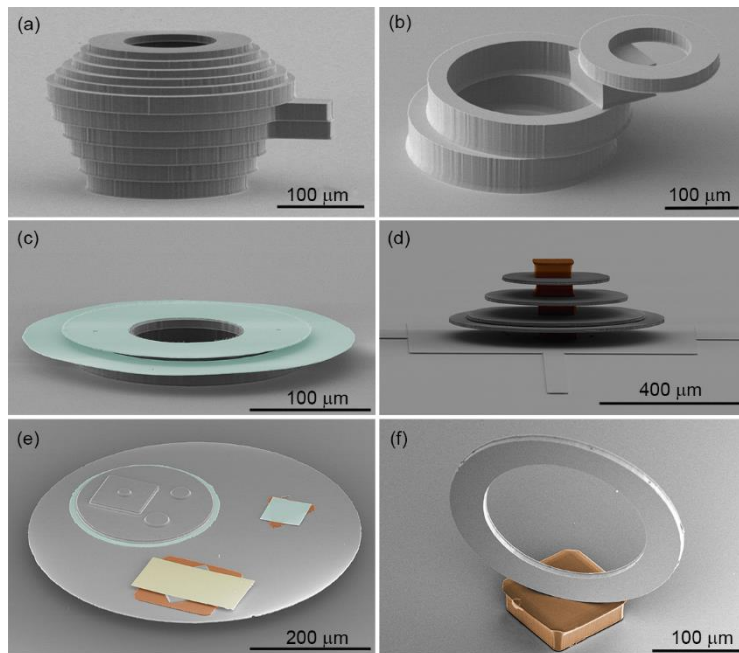
Figure 3.18 *SEM images of heterogeneously integrated material. The images are colorized to highlight the different material constituents of the microscale structures. SiO_2, Au and SU-8 are colored in green, yellow and brown respectively. Si is left uncolored [23,66]*

Likewise, **Figure 3.18 (e)** is the microsctructure that is formed by collection of all the materials available for micro-Lego. While transfer printing process is not precarious by any means, it is in significant importance to plan ahead for their respective permanent joining process since SU-8 polymer exhibits degradation temperature that is lower than some of other joining thermal treatment [23]. Lastly, vertically microassembled Si ring over SU-8 is demonstrated in **Figure 3.18 (f)**. The Si ring ink is first prepared in two-dimensional (2D) approach with the DRIE process, which is rearranged in vertical orientation after inking process by applying shear force to the ink. Although the reliability of the process of reorienting the ink is still in question, such vertical structure with hollow circular region at the center is exceedingly inordinate, which can only be fabricated via micro-Lego process [23]. Although microstructures in is unique, they are not functional devices, which makes them invaluable. Subsequent sections will deal with representative functional devices that are prepared by micro-Lego process.

3.4.2 **Silicon micro-Lego for functional devices**

Unlike much anticipated applications of MEMS devices, the adaptation of MEMS devices is partially stagnant when compared with other semiconductor based electronic devices due to the difficulty in fabrication of actuating device [67, 68]. Although with emergence of micromanufacturing techniques like molding, plating, wet etching, dry etching and electro discharge machining (EDM), the MEMS device began to draw attention. Yet, the market share when compared with other micro / nanoscale electronic devices is still insignificant [69]. Probably, the most common application of accelerometer based devices such as airbag sensor, gyroscopes and pressure sensors, besides the micro-nozzles for inkjet printers, which are commonly based on the comb drive design [70-72]. The fundamental of comb drive is to establish opposing voltage bias between two facing electrodes through which the electrostatic force is formed to either attract or repel the movable component. However, as a result of 2D process nature of the microfabrication, the MEMS devices are frequently structured in planar format where the opposing electrodes are in the same topology. By utilizing micro-Lego process, 3D comb drive can be established with flexure beams for actuation for novel applications and form factor.

Figure 3.19 is a schematic process flow of micro-Lego assembly of the vertical comb drive device. The top comb with flexure beams are prepared in ink format, which is retrieved by microtip stamp (**Figure 3.19 (a)**), and transferred onto another microtip stamp to orient the comb downwards upon transfer printing (**Figure 3.19 (b)**). This process of transferring the ink twice for proper orientation of the ink is termed 'double transfer printing'. **Figure 3.19 (c1)** and **Figure 3.19 (c2)** represent the SEM image of the comb ink after double transfer printing. This ink is subsequently printed with high precision that features spacer and bottom comb as shown in **Figure**

3.19 (d). Schematics of finalized vertical comb drive (**Figure 3.19 (e2)**) are shown as well as after forming electrical contact pad with Au (**Figure 3.19 (f)**) [67].
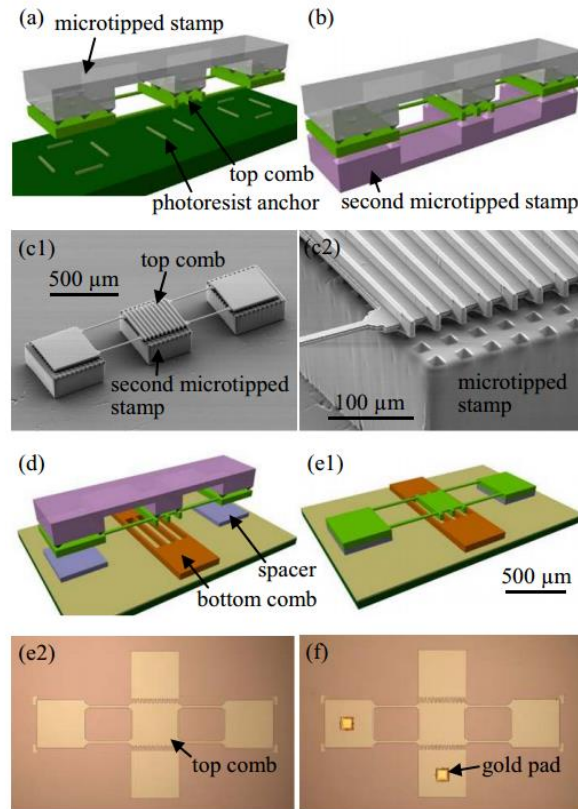
Figure 3.19 Schematics, SEM and optical images of the vertical comb drive fabrication process. (a) and (b) represent the double transfer printing of the top comb drive for proper orientation of the ink (c1) and (c2) are SEM images of the comb ink after double transfer printing (d) schematic of printing (e1) and (e2) are schematic and optical image of fully fabricated device (f) after forming Au contact pad for wire bonding [67]

Another application of Si micro-Lego is in biosensor application where membrane platelet resonators are drawing attention in recent years due to the advantages in stiffer configuration of the membrane form factors when compared with cantilever biosensors [74-80]. The stiffer device structure not only benefits in reliability of the device especially the biosensors are often required to operate in rather harsh environment when experimenting in-vivo or in-situ situations, but also, the stiffer devices have higher Q-factors for higher resolution sensing [81]. Furthermore,

completely sealed membrane resonator with a vacuum cavity beneath eases the fabrication process significantly since cantilever resonators when operating in-vivo require additional post process for encapsulation if operated electrostatically. Much membrane based resonators are fabricated by backside removal of an SOI wafer where the oxide layer is adopted for etch stop, which is commonly used technique when fabricating suspended structure in MEMS devices. However, the process suffers from considerably expensive process (DRIE) as well as inefficiency in material wastes. Hence, exploiting the additive characteristics of micro-Lego, the membrane resonator can be conveniently fabricated.

To observe the feasibility of the nanomembrane resonator fabrication through micro-Lego, passive device is prepared as shown in **Figure 3.20**. The transfer printed ink is prepared as described in previous Si ink section with an SOI wafer that exhibits device layer thickness of 340 nm for extremely thin nanoscale membrane. The gap between the resonating membrane with the base is determined by the thickness of the oxide base, which in this case was predetermined at 1.25 μm with cavity radial dimensions varying from 8 to 30 μm. Following the transfer printing, the fusion joining was conducted at 950 ⁰C to induce the permanent joining, at which stages problems of non-proper joining appeared occasionally due to the expansion of the air captured in the cavity as verified by the infrared microscopy as shown in **Figure 3.21**. The **Figure 3.21 (a)** is the successfully integrated resonating nanomembrane whereas **Figure 3.21 (b)** is the failed specimen as indicated by ambiguous bright yellow region that indicates air gap.
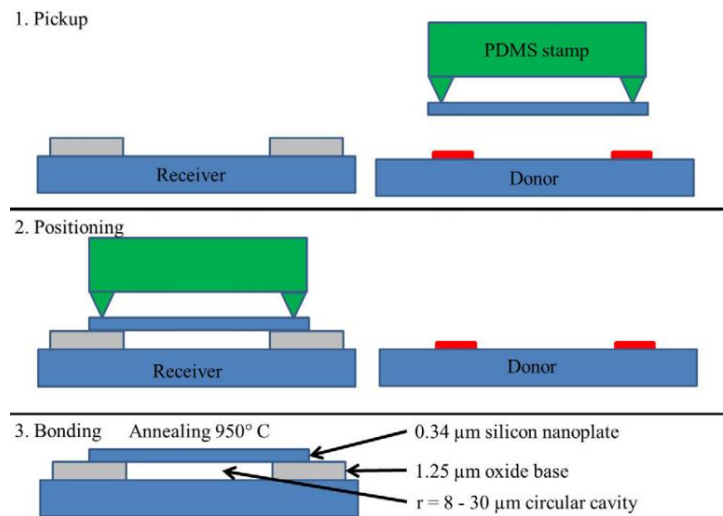
Figure 3.20 *Schematics of micro-Lego assembly of nanomembrane resonator [74]*
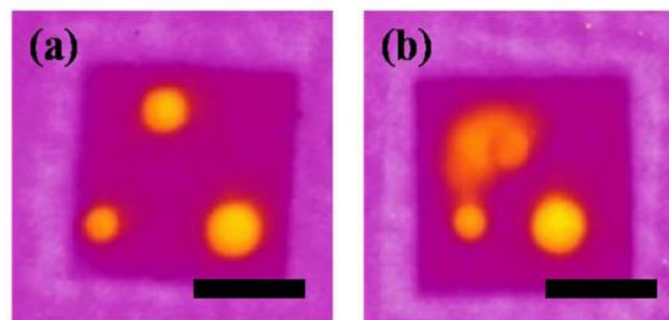
Figure 3.21 *Infrared Microscopic images of the nanomembrane resonator after joining. (a) successful joining and (b) unsuccessful joining. The scalebars are 50 μm [74]*

With established micro-Lego process for nanomembrane resonator, functional active device is subsequently pursued as shown in schematics in **Figure 3.22**. The basic concept of the device is consistent with above-mentioned passive device with differences in Si being heavily doped by boron (B) with a dose of 10^6 atoms/cm^2. It is also worthwhile to mention that the micro-Lego assembled nanomembrane is robust enough to withstand the post process of photolithography process as demonstrated when patterning metallic electrical connection after the micro-Lego assembly of the nanomembrane, which indicates that there're immense potential of the micro-Lego process to fabricate active devices when adopted in conjunction with conventional microfabrication techniques.
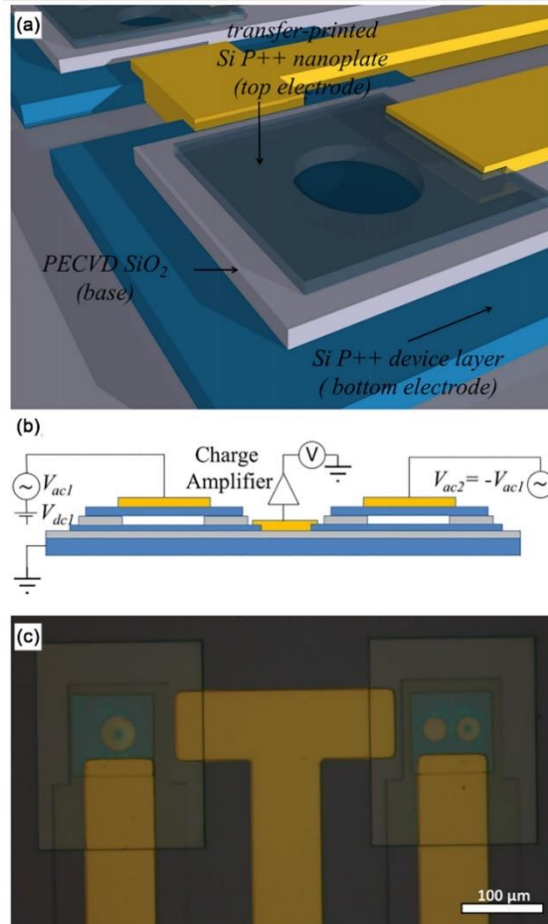
Figure 3.22 _Schematics and optical image of active nanomembrane resonator (a) in perspective view (b) side view and (c) optical image of the fully fabricated device [75]_

AFM is based on microfabricated cantilever structure that is utilized in sensing by measuring the interaction between the tip and the sample, and its sensitivity is in the regime pico-Newton, which enables mapping in sub-nanometer scale, measuring material properties of the sample specimen and even sensing of extremely small mass objects such as biomolecules [83-88]. This unique functionality is attributed by the high Q-factor, which operates in linear behavior. In the other aspect, the AFM suffers in the applications where wide range of frequency operating range is required, which can be conquered by introduction of intentional nonlinearity [89]. Various methods have been investigated including geometrical design alteration of the AFM, which

involves nanoscale attachment for geometric or kinematic nonlinearities such as incorporation of flexible boron nitride nanotube (BNNT) [91,92]. While the nanotube attachment scheme provides strong nonlinearity, the challenges in manually integrating a single nanowire to the AFM is an extremely sluggish task with low yield. In this aspect, micro-Lego of nanomembrane Si ink on to the surface of the AFM and subsequent focused ion beam (FIB) removal is employed to enrich the nonlinear AFM by providing high output via parallel processing of integration as well as high tunability of the degree of coupling and subsequent nonlinearity through delicate FIB process.
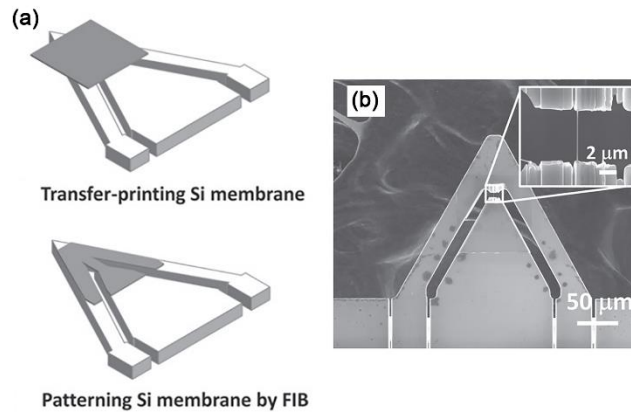
Figure 3.23 *(a) Optical and (b) capacitive measurement as a function of frequency with varying driving DC voltage of the active device fabricated through micro-Lego and subsequent microfabrication process [83]*

Figure 3.23 (a) represents schematic overview of the intentional nonlinearity induced AFM through micro-Lego and FIB processes. The nanoscale thickness Si membrane is micro-Lego assembled onto the tip of AFM (top in **Figure 3.23 (a)**) which is subsequently removed to construct extremely thin coupling between the two distinct cantilevers (bottom in **Figure 3.23 (b)**). The process of transfer printing generally involves slight preloading in printing process, which may band the delicate AFM tip, yet, the negligible adhesion between the Si membrane ink with the microtip PDMS stamp permitted the printing process. **Figure 3.23 (b)** is the SEM image of the

finalized device with its inset to highlight the thin coupling between the two comparably large cantilevers. Once again, the micro-Lego process demonstrated its capability of post vacuum process, since the FIB is done in ultra-high vacuum chamber.

Expanding the intentional non-linearity AFM cantilever project, an AFM tip with inner paddle is prepared to demonstrate an AFM with multi harmonic resonance as shown in **Figure 3.24**. The **Figure 3.24** inhibits 1:3 internal resonance, which in return, enhances the signal at the third harmonic of the response at the micro-Lego assembled inner paddle. Although the scope of its detailed behavior is not in the scope of this thesis, as shown in **Figure 3.23** and **Figure 3.24**, the Si micro-Lego process enriched the field of AFM with its ability to conveniently manufacture the miniscule but complex structures.
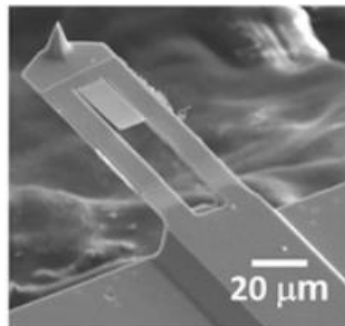
Figure 3.24 SEM image of the AFM tip with inner paddle [84]

Also, micro-Lego assembly of silicon photonic crystal mirror on MEMS scanner actuated by comb drive is pursued [92]. Inspired from the capability of assembling delicate Si photonic crystal as well as ability to print on extremely vulnerable AFM tips, incorporation of Si photonic crystal onto two axis electrostatically actuating MEMS mirror is conducted. MEMS optical devices commonly exploit metal layer such as aluminum (Al) to enhance the reflectivity owing to its process compatibility with other manufacturing protocols utilized in MEMS devices. However, the metallic layer suffers from tolerance in optical power densities, complication in hermetic

packaging and the relatively low operational temperature. The drawbacks of metallic layer can be avoided by employing distributed Bragg reflectors made of dielectric stacks, but the material is challenging to integrate due to the complexity in process compatibility [93]. In this view, photonic crystal (PC) with its high reflectivity and robustness of Bragg mirrors without excessive rigidity and stress seem to be a plausible candidate to enhance the performance of the optical MEMS devices.

Figure 3.25 (a) describes the process flow of photonic crystal fabrication and **Figure 3.25 (b)** describes its subsequent micro-Lego process to incorporate the photonic crystals to the 2-axis electrostatically actuating mirror. The key importance lies in that the photonic ink fabrication is processed on a separate substrate, which doesn't obscure the manufacturing of intensely delicate MEMS mirror. The **Figure 3.26 (a)** represents the fully prepared PC MEMS mirror with micro-Lego process, **Figure 3.26 (b)** and **Figure 3.26 (c)** describes the incorporated PC in top and the cross-sectional views respectively. As visually demonstrated in the SEM images, the photonic crystal with extremely fine features of sphere cavities, are not spoiled during the micro-Lego process.

Micro-Lego process with Si inks have been demonstrated here. For the context of this manuscript, the focus has been on the manufacturing process and what is achievable with micro-Lego processes. The devices presented here either exhibited higher performance, i.e. broader operating frequency, higher Q-factor, or demonstrated new functionalities such as hermetically sealed nanomembrane resonator. Detailed experimental characterizations can be found in the respective manuscripts. Nevertheless, the devices included here can only be created through micro-Lego process.
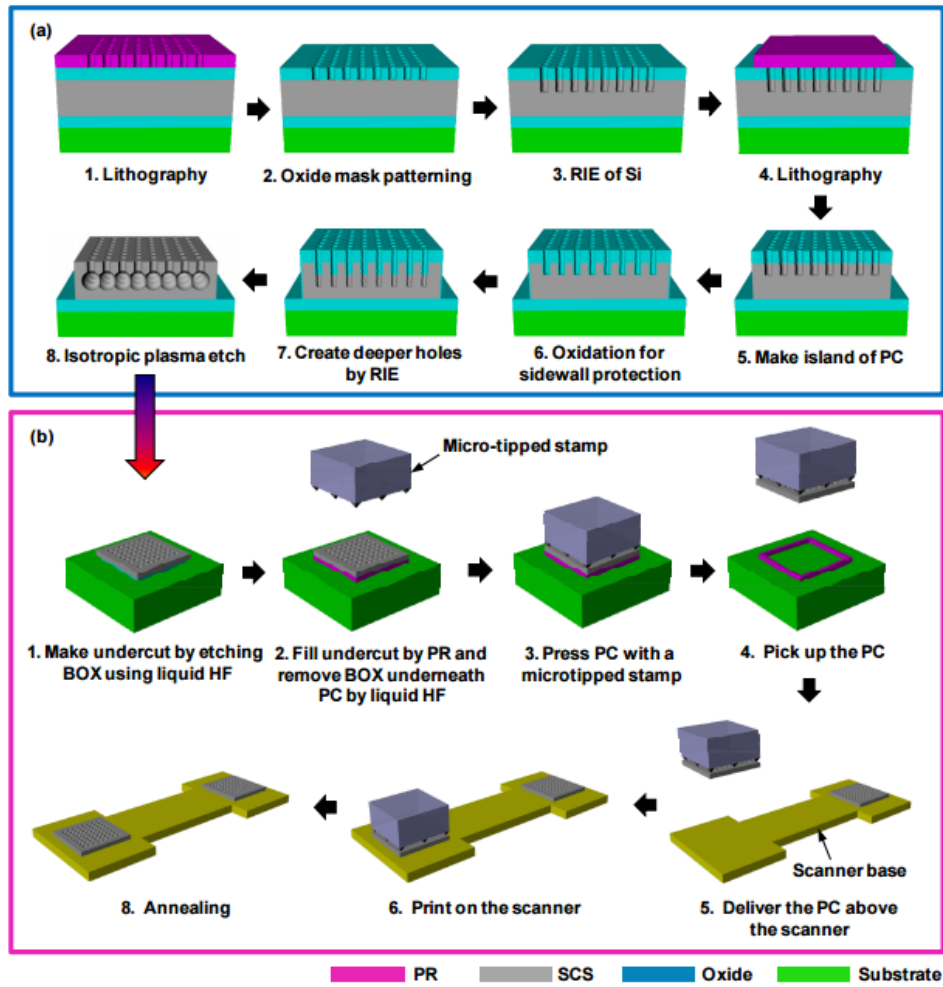
Figure 3.25 *Schematic process flow of the (a) photonic crystal and (b) photonic crystal incorporated MEMS mirror [92]*
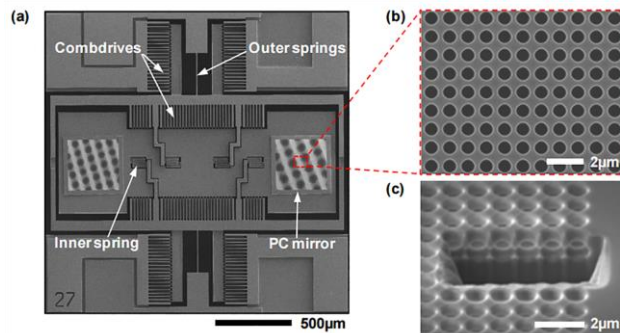
Figure 3.26 *SEM image of the PC incorporated MEMS mirror and its reflectance spectra (a) SEM image of the full PC MEMS mirror (b) top view of the PC, (c) cross section view of the PC [92]*

3.4.3 Gold micro-Lego (thermal switch)
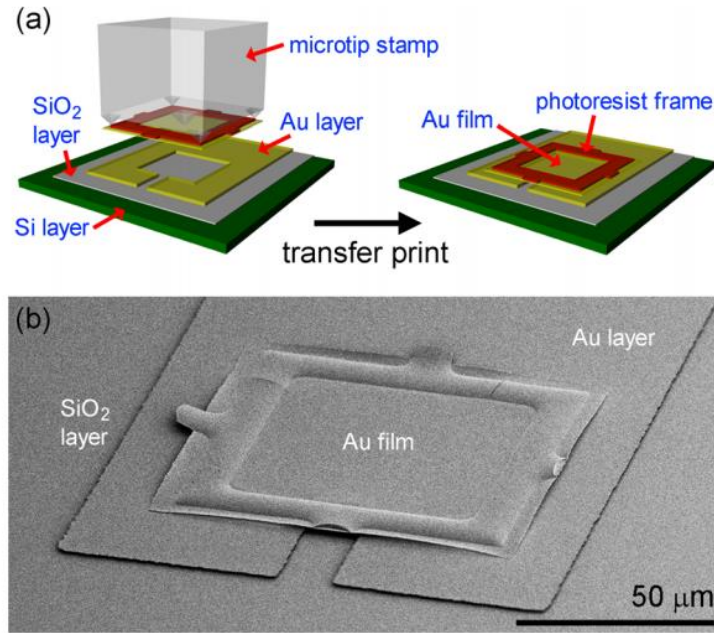
Figure 3.27 (a) Schematic of the device fabrication and (b) SEM image of the fabricated thermal switch device [94]

Previous work with interfacial thermal conductance between transfer printed Au film and different substrates has motivated to develop an electrostatically driven suspended Au membrane structure that exhibits a potential to be operated as a thermal switch [61]. It was found from Au – Au cold welding and its electrical contact resistance experiment that Au – Au joined interface displays exceptional electrical conductance in the level of vacuum deposited interface, which allowed us to design a device structure as shown in **Figure 3.27** [23, 94]**.** Genuinely, the Au ink is prepared as described in previous chapters, which is transfer printed onto a receiver substrate with Au pattern that can form an air cavity underneath the micro-Lego assembled Au membrane. Since the Au ink is printed onto a patterned region on receiver substrate, the electrical bias can be applied at the photolithographically patterned Au that is distant from the printed region (**(Figure 3.27 (a)**). Underneath the Au is an SiO_2 layer, which serves as a dielectric layer to prevent any potential shortage when the Au film collapses and make physical contact with the substrate. **Figure 3.27**

(b) is an SEM image of the fully fabricated specimen with a small opening at the bottom for the air to flow for reliable operation.
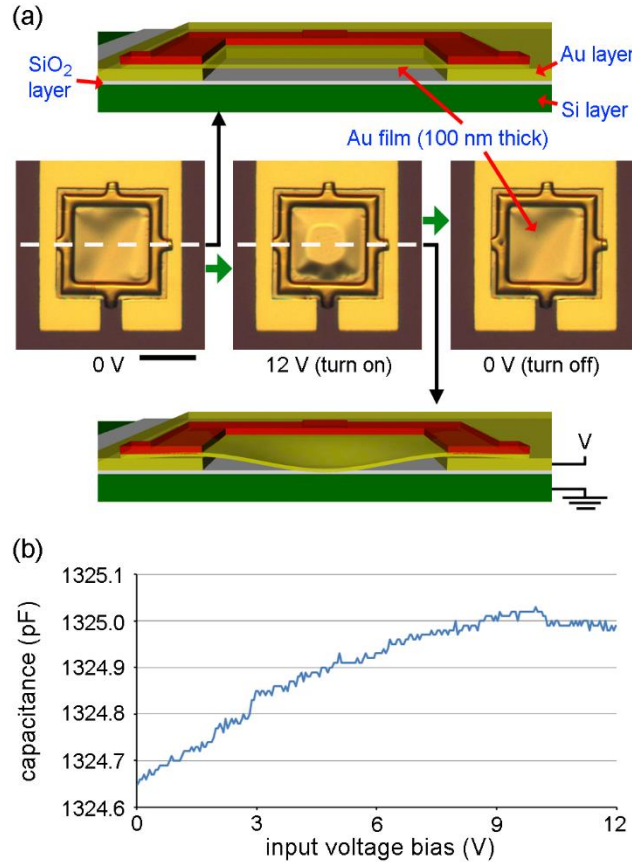
Figure 3.28 (a) Side view schematics of on (top) and off state (bottom) of the proposed active device with optical image (middle row) when electric bias is applied and removed. The middle optical image evidently demonstrates that the central planar region is conformally contacting the bottom oxide layer. (b) capacitance measurement plot with voltage bias. The capacitance gradually increases and become steady when it approaches ~ 11 – 12 V [94]

The device fabricated is applied with electrical bias between the top and the bottom electrodes and at ~ 12 V of bias, the top micro-Lego assembled Au layer is fully collapsed and makes the conformal contact with the bottom dielectric layer as presented in the **Figure 3.28 (a)**. The **Figure 3.28 (a)** includes the optical image that demonstrates the reversibility with the electrical bias (middle row) with corresponding side view schematics on top (off state) and the on state (collapsed state). The middle optical image shows flat planar region at the center where the

Au is pulled to contact the bottom dielectric layer. In addition to the optical observation of the deformation, capacitance change with respect to the voltage bias was measured to further validify the operation of the electrostatic actuation, which is shown in **Figure 3.28 (b)**. The absolute values of the capacitance are not considered due to the parasitic capacitance that exists between the two electrodes, but the focus in the plot is in its change in the capacitance.

$$C_{total} = \frac{C_{oxide} C_{air}}{C_{oxide} + C_{air}} \qquad (3\text{-}10)$$

When the Au membrane is in fully suspended, the total capacitance, C_{total}, is function of C_{oxide} and C_{air} where each term represents capacitance in oxide layer and the capacitance in the air as shown in **Equation 3-10**. The parallel plate assumption yields

$$C = \frac{\varepsilon A}{d} \qquad (3\text{-}11)$$

where ε, A and d represent electrical permittivity, area (50 μm x 50 μm) and the distance between the two electrodes. When the top electrode is fully collapsed, the capacitance only exists within the SiO$_2$ layer, which can be obtained from **Equation 3-11**. After through calculation, the capacitance difference between adhesion on and off states is ~ 0.55 pF which is slightly higher than the capacitance change obtained experimentally through LCR meter (0.35 pF). Although the difference isn't insignificant, the assumption that complete removal of capacitance in air layer is comparably crude approximation since the optical image indicates that only the fraction of the suspended region is fully collapsed and the other regions are in transition.

$$U = \frac{-CV^2}{2} = \frac{-\varepsilon A V^2}{2d} \qquad (3\text{-}12)$$

$$P_{elec} = \frac{V^2 \varepsilon_{oxide}^2 \varepsilon_{air}^2}{2(\varepsilon_{air} d_{oxide} + \varepsilon_{0x9de} d_{air})^2} \tag{3-13}$$

$$w_{max} = c_1 \frac{P_{mech} L^4}{E h^3} \tag{3-14}$$

Additionally, the optical image in **Figure 3.28 (a)** left indicates that the micro-Lego assembled Au membrane is not perfectly planar, which could've also altered the capacitance measurement. In addition to the capacitance change, the mechanical collapsing behavior with respect to the voltage applied is considered analytically, by first looking at the total potential energy of the capacitor as shown in **Equation 3-12**, which is subsequently taken derivative with respect to d and divide by the area to obtain **Equation 3-13,** which can be equated with mechanical pressure **(Equation 3-14)** to obtain the required voltage for the deflection of air gap in the capacitor. In **Equation 3-14,** w_{max}, c_1, L^4, E and h represents height of the deflection, geometric factor of 0.0444, lateral dimension, Young's modulus and thickness of the deflecting membrane respectively [95]. The voltage required to deflect the airgap of 800 nm is calculated at 11 V, which closely matches with our operating voltage of 12 V.

3.4.4 Micro-Lego of heterogeneous materials

The devices demonstrated so far are all solely based on micro-Lego assembly of homogeneous materials, i.e. Si ink assembled on Si receiving surface and Au on Au surface. Although the homogeneously assembled inks served its unique functionalities, the ability to heterogeneous integration of micro-Lego process exhibits potential to be employed in the wide range of applications. The subsequent sections deal with some of the applications of micro-Lego when homogeneously integrated. Although the devices had already been demonstrated by other numerous research groups, the ease of fabrication by micro-Lego assembly is the highlight of the

demonstrate while maintaining its device performance on par with the conventionally available devices.

3.4.4.1 **Microtoroid optical resonator**

The first demonstrative heterogeneously integrated microdevices is a photonic whispering-gallery resonator (WGR) shaped in microscale toroid which is much touted in nonlinear optics with its extremely high optical Q-factors [96-99]. In typical fashion, the SiO_2 micro resonators of toroidal and edge-disk configurations are formed through combination of chemical etching, laser-reflow and undercut etching by XeF_2 [100]. Although their superiority in the device performance had been proven, the integration of such microtoroid resonators with electronic devices or other form of microdevices made of Si is considerably challenging due to the XeF_2 undercut etching. In this aspect, additive manufacturing technique is more favorable. Furthermore, complex multi-layered WGR geometries are also possible if the structure presented in **(c)** is fully exploited. **Figure 3.29 (a)** shows a process flow for producing a SiO_2 microtoroid through micro-Lego and **Figure 3.29 (b)** and **(c)** show SEM images of the device before and after the laser reflow of SiO_2 top layer. The SiO_2 in SEM images are colored in green to further distinguish the material with Si. The fabricated microtoroid resonator is tested via tapered fiber-coupling as shown in **Figure 3.29 (d)**, which yielded the transmission plot as shown in **Figure 3.29 (e)** [101]. The characteristic Lorentzian shaped 0.087 nm wide optical resonance of the WGR at 1549 is discovered with Q-factor of 1.7×10^4. The Q-factor extracted is not on par with the state-of-the-art microtoroid resonator, but it is still higher than the best reported planar 2D resonators. Therefore, it can be concluded that the presented microtoroid WGR resonator serves its functionality with room for improvement, such as uniformity in the SiO_2 disk during laser reflow.
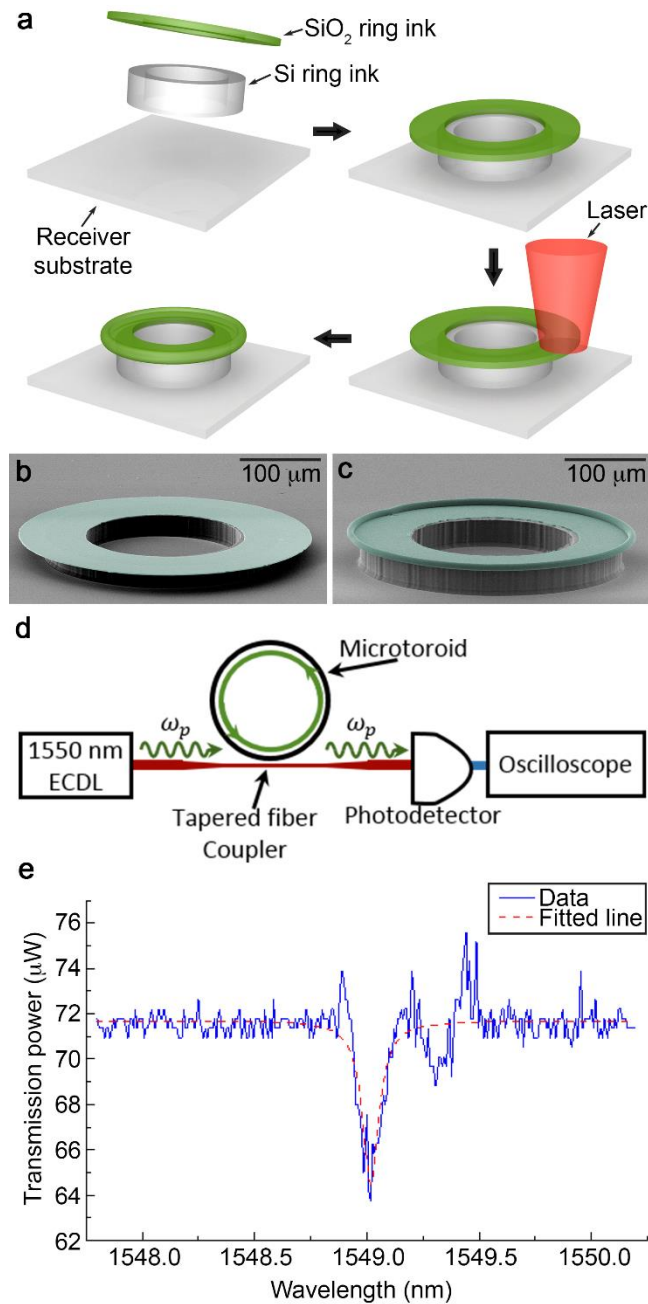
Figure 3.29 *(a) Schematics of a microtoroid resonator fabrication. Through micro-Lego, Si ring and SiO2 disc inks are assembled. The assembled structure is illuminated with 10.6 μm wavelength light from a 10W CO_2 laser to induce material reflow at the outer circumference of the SiO$_2$ disc, resulting in microtoroid shaped whispering-gallery photonic resonator. (b,c) SEM images of the assembled structure before and after lasing. These images are colored to provide distinction between different materials. Untouched and green color represent Si and SiO$_2$, respectively. (d) Laser light is coupled into a microtoroid resonator through a tapered optical fiber. Forward propagating light in the fiber is collected at a photodetector and analyzed by an oscilloscope. (e)*

Power transmission in the fiber is measured with respect to wavelength, and shows the characteristic resonance dip associated with the microtoroid resonance. Lorentzian curve fitting indicates Q-factor of 1.7×10^4 [23]

3.4.4.2 **RF MEMS switch**
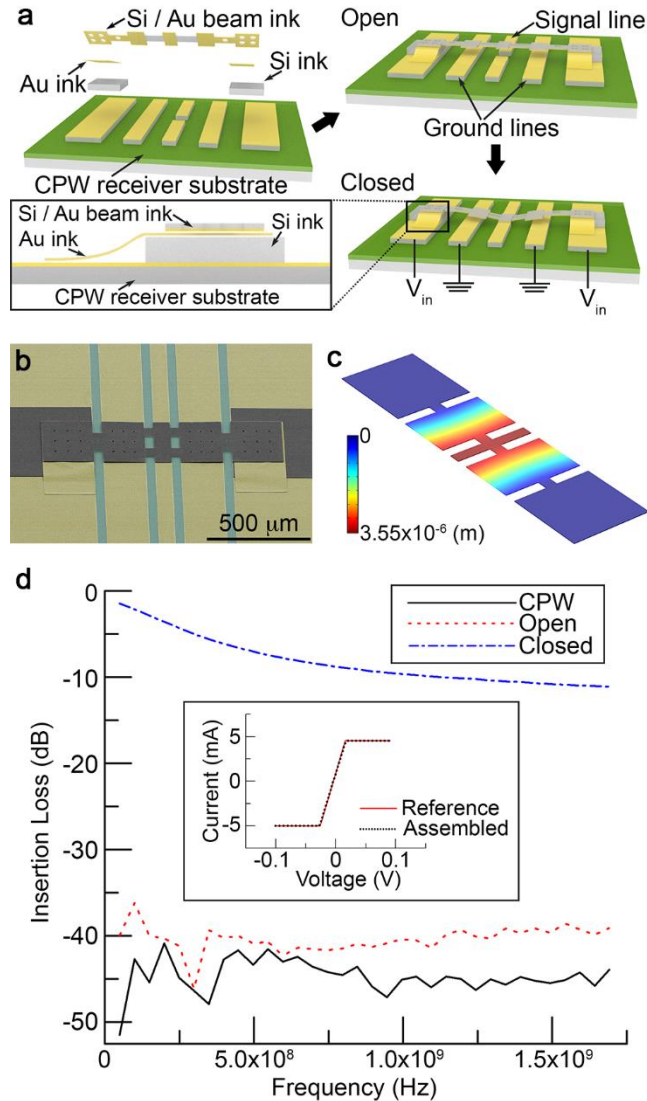
Figure 3-30 (a) Schematics of a radio frequency (RF) MEMS switch assembled via micro-Lego. The suspended beam on a coplanar waveguide (CPW) substrate deflects upon biasing resulting in physical contact with the center signal line. An inset cross-sectional illustration highlights 3D interconnection using an Au ink assembled on two different steps. (b) A SEM image of the assembled RF MEMS switch. The image is colored to provide distinction between different materials. Untouched, green and yellow colors represent Si, SiO_2 and Au, respectively. (c) FEA simulation of the mechanical deflection of the suspended beam. Upon 25 V, the central region of

Figure 3-30 (continued)
the beam deflects approximately 3.6 μm allowing for physical contact with the center signal line.
(d) Measured insertion loss data in CPW, open and closed states [23].

Furthermore, a series contact type radio frequency [RF] MEMs switch is fabricated. RF MEMS switches often require suspended form factor for actuation to switch on and off the RF signal, and preparation of such suspended thin film architecture is somewhat complicated due to the stiction during wet process [102]. Flip-chip transfer techniques are also explored, but the limitation with a single transfer in the filp-chip transfer technique bounds the utilization of the process technique [103]. Hence, micro-Lego process that transfers and joins individual components of a device in dry condition in the device fabrication when compared with other means of microfabrication and transfer techniques can greatly reduce the complexity and endow more freedom in design at the same time. **Figure 3-30 (a)** is the schematic of the manufacturing process where co-planar waveguide (CPW) is patterned lithographically on Si / SiO$_2$ substrate, on which, Si (spacer), Au (electrical connection) and Si / Au composite beams are transfer printed and joined following the process protocol as depicted previously. The suspended Si / Au composite beam in suspended architecture is actuated through electrostatic force, which controls the RF signal. The inset in **Figure 3-30 (a)** represents the electrical interconnection by the Au ink, which connects the two components in different topology by utilizing the inherent ductile nature of the Au. Further detailed micro-Lego assembly process can be found in **Figure 3.31** where **Figure 3.31 (a)** describes the dimensions and geometry, **Figure 3.31 (b)** represents individual inks utilized for RF MEMS switch fabrication and **Figure 3.31 (c)** is the assembly procedure.
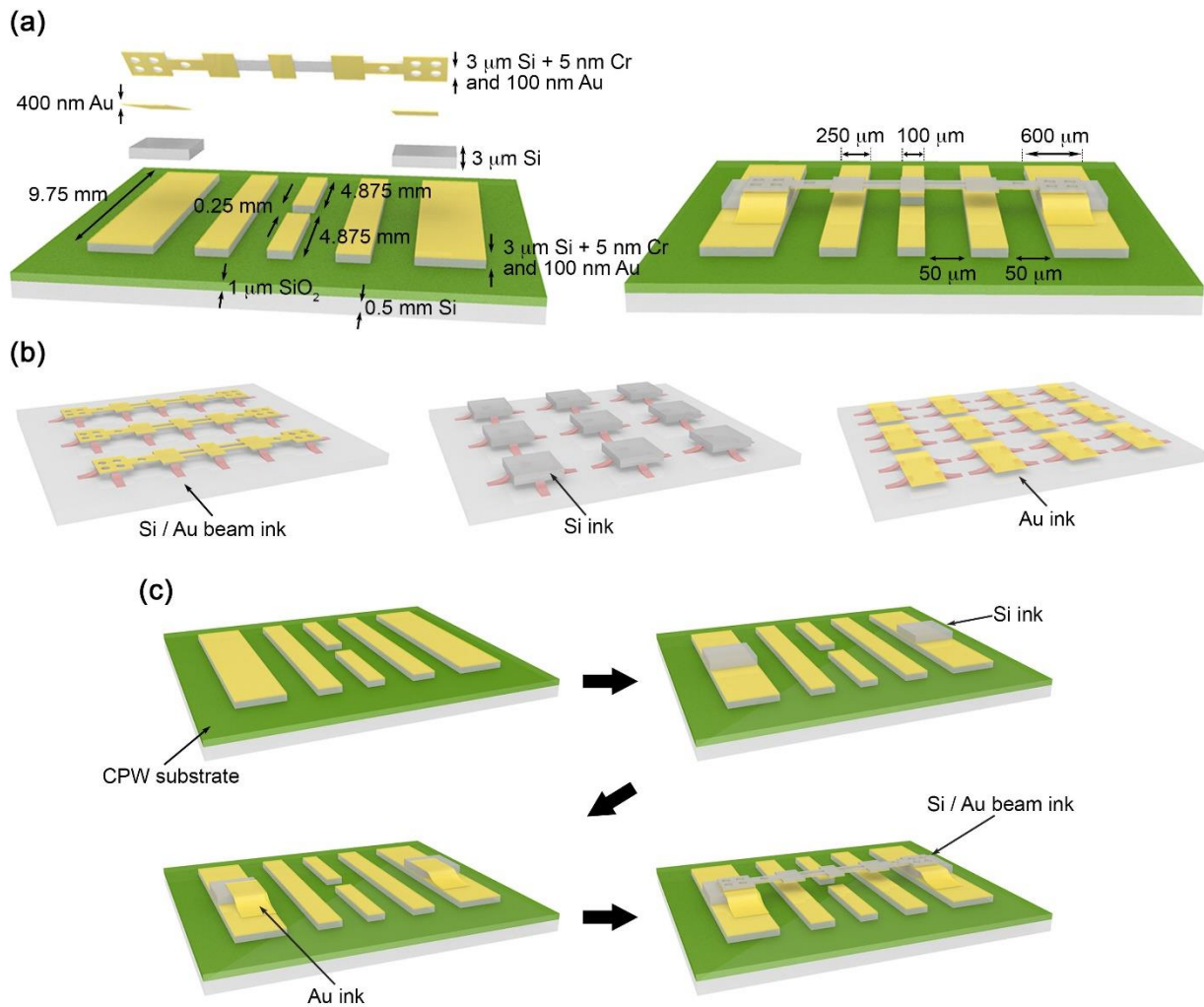
Figure 3.31 *Schematics of RF MEMS switch device (a) dimensions and geometry of the RF MEMS switch with explode view and assembled view (b) description of individual inks fabricated (c) sequence of assembly [23].*

Figure 3-30 (b) is the SEM image of the fully fabricated devices with post colorizing process in yellow (Au), green (SiO_2) and natural SEM color (Si) to differentiate the different materials assembled by micro-Lego. The FEA simulation is conducted to estimate the required voltage to deflect ~ 3 μm, which is the thickness of the spacer (**Figure 3-30 (c)**). The simulation reveals that upon 450 Pa, the deflection of 3.5 μm is achieved. The pressure applied is converted

to ~25 V by **Equation 3-15**, where ε, A, V and d represents permittivity, area, voltage and distance between the two plates respectively.

$$F = \frac{\varepsilon A V^2}{2 d^2}$$

(3-15)

The **Figure 3-30 (d)** represents the insertion loss plot with respect to frequency. The RF MEMS switch, as fabricated is in open state and the pull-down state is the closed state. The comparison between CPW and open states show small difference while the closed state plot is clearly distinguished with its significantly low level of insertion loss.

3.4.4.3 **Metamaterial devices**

Metamaterial refers to an engineered material through meticulous arrangement of geometry, size and orientation to yield properties that are not found in nature [104]. The fine tuning of the metamaterial is established by repeating patterns with different materials in the scales that are smaller than the electromagnetic or sound waves to interfere with the diffracted waves. In the early ages of the metamaterial focused on the theoretical analysis and experiments on the phenomena of the metamaterials, which are extended to facilitate the unusual characteristics to realize functional devices [105-109]. A notable challenge in metamaterial device fabrication is in the difficulty in heterogeneous integration where the metamaterials modules are generally formed in composite format with different class of materials. Lithography based microfabrication techniques have been adopted to form 2D planar metamaterial surfaces, which can be further enhanced in their utilization if profound and convenient tool for heterogeneous integration is developed. In this view, micro-Lego process is employed to form metamaterial surfaces in 2D arrangement on polymeric surface for compliant metasurface as well as 3D structure for further tunability and functionalities.

Unlike the inks demonstrated until now, the metamaterial ink module exhibits metal on silicon membrane (MoSM) composite format. The composite material configuration adds an extra procedure of deposition and patterning the metal layer on the device Si in SOI wafer, it doesn't significantly complicate the overall ink fabrication. Following the metal layer patterning is analogous with conventional Si ink fabrication, where the device Si layer is patterned into 600 μm x 600 μm lateral dimensions using conventional microfabrication techniques and the subsequent anchor formation and undercut etching of the box oxide layer. The key importance in this step is the meticulously designed metal layer in its dimension, arrangements and configuration as well as the low doping level of the device silicon layer (high resistivity float zone) for optimal performance in the designed operating terahertz (THz) frequencies. The designing and simulation of the metamaterial is found in the supporting information in [104], which is neglected since the scope of this manuscript is in the modular micro-Lego assembly of the metamaterial.

Figure 3.32 shows 2D and 3D arrangement of micro-Lego assembled metamaterial. The honeycomb MoSM inks are printed on polyimide (PI, **Figure 3.32 (a)**) and on PDMS (**Figure 3.32 (b)** and **Figure 3.32 (c)**) in arrays of 5 x 5 and 15 x 20 in 2D arrangement. Printing on both PI and PDMS organic materials are advantageous since the surfaces are rather tacky, which facilitates the printing procedure effortlessly while the compliant material properties enable conformal lamination on the curved surfaces. However, the adhesion between the printed MoSM inks and the polymeric surfaces are debatable, which is further accommodated with encapsulation with PI. The large array of MoSM printed on PDMS demonstrates the feasibility of micro-Lego process of large sheet-like metamaterial array on compliant and stretchable surfaces, that endows freedom in metadevice designs. Additionally, multiple stacking of the metamaterial is demonstrated in **Figure 3.32 (d)** through **Figure 3.32 (f)** with intentional angular and lateral offsets.
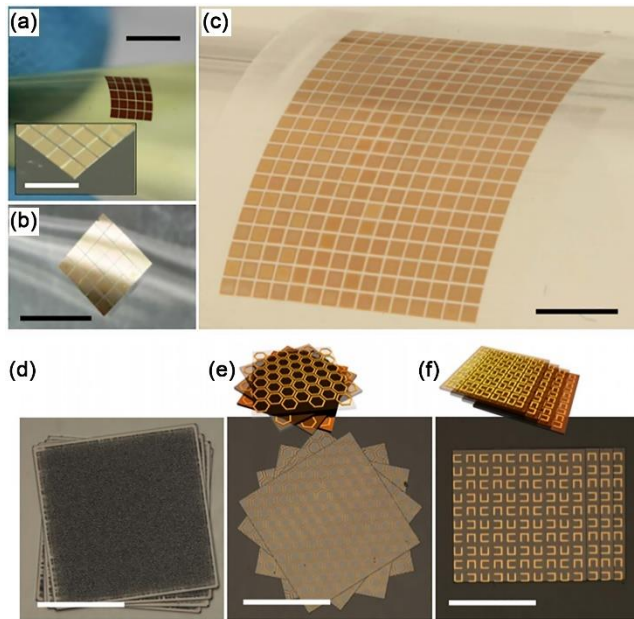
Figure 3.32 *Optical images of the metamaterial integrated in 2D and 3D format (a) 5 x 5 honeycomb MoSM array printed on polyimide (PI) with scalebars 3.5 mm and 2.0 mm (inset) (b) 5 x 5 honeycomb MoSM printed on PDMS with 3.5 mm scalebar (c) 15 x 20 printed on PDMS with 3.5 mm scalebar (d) 3D printed rough silicon membranes (320 nm of root mean square) (e) 3D printed honeycomb MoSM with larger angular rotation (f) U shaped MoSM with offset. The figures (d) – (f) have scale bar of 300 μm [104].*

The **Figure 3.32 (d)** is a primitive demonstration of the feasibility of micro-Lego assembly of rough surfaces (root mean square of 320nm) which is similar with the thickness of the metallic layer in MoSM. Encouraged with the result from **Figure 3.32 (d)**, multiple stacking of the MoSM in honeycomb and U shaped patterns is conducted as shown in **Figure 3.32 (e)** and **Figure 3.32 (f)**. For the joining purpose of the multiple stacked MoSM, thermal treatment of 330 ºC for 2 hours is conducted to induce slight reflow of the metallic layer, as with gold welding. Although the joining techniques are not fully characterized in terms of mechanical stability, the reliability in the multiple stacking with offsets imply that their joining strength is higher than mere Van der Waal's interaction. The work described here demonstrates the feasibility of metamaterial incorporation in large 2D sheet like configuration on compliant and stretchable substrate as well as 3D multiple

stacking with offsets. The operating frequency is in the realm of THz, which bounds the application as in the device functionalities. However, with further delicate design and the fabrication of MoSM inks, metamaterial devices with unparalleled performances with uncommon form factors are achievable.

3.5 References

[1]   Carlson, A., et al., *Transfer Printing Techniques for Materials Assmebly and Micro/Nanodevice Fabrication*. Advanced Materials, 2012, **24**: p. 5284-5318

[2]   Flory, P. J., and Tatara, Y.-I., *The Elastic Freen Energy and the Elastic Equation of State: Elongation and Swelling of Polydimethysiloxane Netowrks*. Advanced Materials, 1975, **13**, 4: p. 683-702

[3]   Mark, J. E., and Sullivan, J. L., *Model networks of end-linked polydimethylsiloxane chains. I. Comparison between experimental and theoretical values of the elastic modulus and the equilibrium degree of swelling.* The Journal of chemical Physics, 1977, **66**: p.1006-1011

[4]   Camino, G., Lomakin, S. M., and Legeard, M., *Thermal polydimethysiloxane degradation. Part 2. The degradation mechanisms.* Polymer, 2002, **43**: p. 2011-2015

[5]   Chang, T. C., Chen, H. B., Chiu, Y. S., and Ho, S. Y., *Degradation of polydimethylsiloxane-bloc-polystyrene copolymer*, Polymer degradation and stability, 1997, **57**: p. 7-14

[6]   Mcdonald, J. C., and Whitesides, G. M., *Poly(dimethylsiloxane) as a Material for Fabricating Microfluidic Devices*, Accounts of Chemical Research, 2002, Vol. **35**, No. 7: p. 491-499

[7]   Sylgard 184, Dow Corning corp., Midland, MI, http://www.dowcorning.com

[8]   Ashurst, W. R., et al. *Dichlorodimethysilane as an Anti-Stiction Monolayer for MEMS: A comparison to the Octadecyltricholosiane Self-Assembled Monolayer.* Journal of Microelectromechanical Systems, 2001 Vol. **10**: p. 41-49

[9]   Maboudian, R., Ashurst, W. R., and Carraro, C., *Self-assembled monolayers as anti-stiction coatings for MEMS: characteristics and recent developments*, Sensors and Actuators, 2000, **82**: p. 219-223

[10]   Meitl, M. A., et al., *Transfer printing by kinetic control of adhesion to an elastomeric stamp,* Nature Materials, 2006, **5**: p. 33-38

[11]   Kim, B. H., et al. *Multilayer Transfer Printing for Pixelated, Multicolor Quantum Dot Light-Emitting Diodes*, ACS Nano, 2016 **10**: p. 4920-4925

[12]   Kim, T.-H., et al., *Bright and stable quantum dots and their applications in full-color displays*, MRS Bulletin, 2013, **38**, 09: p. 712-720

[13]   Lee, S., Yoon, D., Choi, D. and Kim, T.-H., *Mechanical characterizations of high-quality quantum dot arrays via transfer printing*, Nanotechnology, 2013, **24**, 025702

[14]   Hines, d. R. et al., *Nanotransfer printing of organic and carbon nanotube thin-film transistors on plastic substrates*. Applied Physics Letters, 2005, **86**, 163101

[15]   Yip, H.-L., et al., *Patterning of Robust Self-Assembled n-type Hexaazatrinaphthylene-Based Nanorods and Nanowires by Microcontact Printing*, Journal of the American Chemical Society, 2006, **128**, 40: p. 13042-13043

[16]   Waser, R., *Nanoelectronics and information technology.* John Wiley & Sons, 2012

[17]   Hanson, G. W. *Fundamentals of nanoelectronics.* Pearson / Prentice Hall, Upper Saddle River, 2008

[18]   Schroder, D. K., *Semiconductor material and device characterization.* John Wiley & Sons, 20206

[19]   Siffert, P., and Krimmel, Eberhard, *Silicon: Evolution and future of a technology,* Springer Science & Business Media, 2013

[20]   Tomozeiu, N., Antohe, S., and Modreanu, M., *Electrical Properties of LPCVD Polysilicon Deposited in the Vicinity of Amorphous – Polycrystalline Phase,* Journal of Optoelectrnoics and Advanced Materials, 2000, Vol **2**, no. 5: p.657-663

[21]   Proano, R. E., Misage, R. S., and AST, D. G., *Development and Electrical Properties of Undoped Polycrystalline Silicon Thin-Film Transistors,* IEEE Transactions on Electron Devices, 1989, Vol. **36**, No. 9: p. 1915-1922

[22]   Liu, C., *Foundations of MEMS, Second edition,* Pearson, 2012

[23]   Keum, H., et al, *Microassembly of Heterogeneous Materials using Transfer Printing and Thermal Processing*, Scientific Reports, 2016, vol. **6**, 29925

[24]   Kim, S., et al., *Microstructured elastomeric surfaces with reversible adhesion and examples of their use in deterministic assembly by transfer printing.* Proceedings of the National Academy of Sciences, 2010, **107.40**: p. 17095-17100

[25]   Goodman, P., *Current and future uses of gold in electronics,* Gold Bulletin, 2002, **5**.1: p. 21-26

[26]   Ellis, T. W., *The future of gold in electronics,* Gold Bulletin, 2004, **37**.1: p. 66-71

[27]   Holliday, R., and Goodman, P., *Going for gold [gold in electronics industry],* IEE Review, 2002, **48**.3 p: 15-19

[28]   Riordan, M., *The silicon dioxide solution* IEEE Spectrum, 2007, **55.** 12: p. 51-56

[29]   Lukasiak, L., and Jakubowski, A., *History of semiconductors,* Journal of Telecommunications and information technology 2010: p.3-9

[30]   Kingon, A. I., Maria, J. -P., and Steiffer, S. K., *Alternative dielectrics to silicon dioxide for memory and logic devices,* Nature, 2000, **406**.6799: p. 1032-1038

[31]   Lorenz, H., et al., *SU-8: a low-cost negative resist for MEMS*, Journal of Micromechanics and Miroengineering, 1997, **7**: p. 121-124

[32]   Campo, A. D., and Greiner, C., *SU-8: a photoresist for high-aspect-ratio and 3D submicron lithography,* Journal of Micromechanics and Microengineering, 2007, **17**: p. R81-R95

[33]   Lee, K. Y., LaBianca, N., and Rishton, S. A., *Micromachining applications of a high resolution ultrathick photoresist,* Journal of Vacuum Science & Technology B: Microelectronics and Nanometer Structure Processing, Measurement, and Phenomena, 1995, **13**, 3012

[34]   NaNO[TM] PMMA and Copolymer, Newton, MA, MicroChem, http://microchem.com/pdf/PMMA_Data_Sheet.pdf

[35]   Maszara, W. P. "Silicon-On-Insulator by Wafer Bonding: A Review." Journal of the Electrochemical Society, 1991, **138**.1: p. 341-347.

[36]   Liu, Z., and Devoe, D. L., *Micromechanism fabrication using silicon fusion bonding*, Robotics and Computer Integrated Manufacturing, 2001, *17*: p. 131-137

[37]   Shimbo, M., Furukawa, K., Fukuda K., and Tanzawa, K., *Silicon-to-silicon direct bonding method*, Journal of Applied Physics, 1986, **60**, 2987

[38]   Lasky, J. B., *Wafer bonding for silicon-on-insulator technology*, Applied Physics Letters, 1986, **48**, 78

[39]   Abe, T., et al., *Silicon Wafer Bonding Mechanism for Silicon-on-Insulator Structures,* Japanese Journal of Applied Physics, 1990, Vol. **29**, No. 12: p. L2311-L2314

[40]   Plobl, A., and Krauter, G., *Wafer direct bonding: tailoring adhesion between brittle materials,* Materials Cience and Engineering, 1999, **R25**: p. 1-88

[41]   Maszara, W. P., Goetz, G., Cavigila, A., and McKitterick, J. B., *Bonding of silicon wafer for silicon-on-insulator,* Journal of Applied Physics, 1988, **64**, 4943

[42]   Gotou, H., et al., *A 256 kbit SOI-full-CMOS-SRAM*, Electron Devices Meeting, 1989, IEDM 89, Technical Digest, International IEEE

[43]   Keum, H,, Chung, H.-J. and Kim, S.,. *Electrical contact at the interface between silicon and transfer-printed gold films by eutectic joining*. ACS applied materials & interfaces, 2013, **5**.13: p. 6061-6065.

[44]   Wolffenbuttel, R. F. *Low-temperature intermediate Au-Si wafer bonding; eutectic or silicide bond,* Sensors and Actuators A: Physical, 1997, **62**.1: p. 680-686.

[45]   Tiensuu, A.-L., et al., *Assembling three-dimensional microstructures using gold-silicon eutectic bonding,* Sensors and Actuators A: Physical, 1994, **45**. 3: p. 227-236

[46]   Lani, S., et al., *Gold metallizations for eutectic bonding of silicon wafers,* Microsystems technologies, 2006, **12**, 10-11: p. 1021-1025

[47]   Okamoto, H., and Massalski, T. B., *The Au-Si (gold-silicon) system,* Journal of Phase Equilibria, 1983, **4**.2: p. 190-198

[48]   Ferguson, G. S., and Chaudhury, M. K., Sigal, G. B., Whitesides, G. M., *Contact adhesion of thin gold films on elastomeric supports: cold welding under ambient conditions,* Science, 1991, **253**. 5021: 776

[49]   Lu, Y., et al., *Cold welding of ultrathin gold nanowires,* Nature nanotechnology, 2010, **5**.3: p. 218-224.

[50]   Franssila, S., *Introduction to microfabrication,* John Wiley & Sons, 2010.

[51]   Yu, L., et al., *Adhesive bonding with SU-8 at wafer level for microfluidic devices*, Journal of Physics: Conference Series, 2006, **34**, 776

[52]   Bilenber, B., Nielsen, T., Clausen, B., and Kristensen, A., *PMMA to SU-8 bonding for polymer based lab-on-a-chip systems with integrated optics,* Journal of Micromechanics and Microengineering, 2004, **14**: p. 814-818

[53]   Allen, M. G., and Senturia, S. D., *Analysis of critical debonding pressures of stressed thin films in the blister test.* The Journal of Adhesion 1988, **25**.4: p. 303-315.

[54]   Doll, A., et al. *Versatile low temperature wafer bonding and bond strength measurement by a blister test method.* Microsystem technologies 2006, **12**.5: p.418-429.

[55]   Ayón, A. A., et al. *Characterization of silicon wafer bonding for power MEMS applications. Sensors and Actuators A: Physical*, 2003, **103**.1: p. 1-8.

[56]   Fischer-Cripps, A. C., *Nanoindentation,* Springer, New York, 2004

[57]   Lee, H., Coutu Jr., R. A., Mall, S., and Kladitis, P. E., *Nanoindentation technique for characterizing cantilever beam style RF microelectromechanical systems (MEMS) switches*, Journal of Micromechanics and Microengineering, 2005, **15**: p. 1230-1235

[58]   Dym, C. L., and Shames, I. H., *Solid Mechanics,* McGraw-Hill, New York, 1973

[59]   SU-8 Permanent Photoresist, Microchem, http://www.microchem.com/pdf/SU-8-table-of-properties.pdf

[60]   Yang, Z., and Kim, S., *Positioning errors in transfer printing-based microassembly,* Journal of Micro-Bio Robotics, DOI: 10.1007/s12213-016-0092-0

[61]   Oh, D.-W., et al., *Interfacial thermal conductance of transfer-printed metal films*, Advanced Materials, 2011, **23**, 5028

[62]   Reeves, G. K., and Harrison, H. B., *Obtaining the specific contact resistance from transmission line model measurements,* IEEE electron device letters, 1982, **3**, 5: p.111-113

[63]   Schroder, D. K., *Semiconductor material and device characterization, 3rd ed.,* John Wiley & Sons, Inc., Hoboken, NJ, 2006

[64]   Stavitski, N., et al., *Specific Contact Resistance Measurements of Metal-Semiconductor Junctions,* Microelectronic Test Structure, 2006, IEEE International Conference

[65]   Young, T. F., Chang, J. F., and Ueng, H. Y., *Study of annealing effects of Au thin films on Si*, Thin Solid Fims, 1998, **322**.1: p. 319-322

[66] Keum, H., et al., *Silicon Micro-Masonry Using Elastomeric Stamps for Three-dimensional Microfabrication,* Journal of Micromechanics and Microengineering, 2012, **22,** 055018

[67] Zhang, Y., et al., *Micro-Masonry of MEMS Sensors and Actuators,* IEEE / ASME Journal of Microelectromechanical Systems, 2014, **13**, 308

[68] Feynman, R. P., *There's plenty of room at the bottom*, Engineering and Science, 1960, **23**.5: p. 22-36

[69] Azonano, *Worldwide MEMS System Market Forcasted to Reach $72 Billion by 2011*, AZoNano, Juyly 17, 2007, http://www.azonano.com/news.aspx?newsID=4479

[70] Tang, W. C., et al., *Electrostatic-comb Drive of Lateral Polysilicon Resonators,* Sensors and Actuators, 1990, **A21-A23**: p. 328-331

[71] Legtenberg, R., Groeneveld, A. W., and Elwenspoek, M., *Comb-drive actuators for large displacements*, Journal of Micromechanics and microengineering, 1996, **6**.3: p.320

[72] Bernstein, J., et al., *A micromachined comb-drive tuning fork rate gyroscope*, Micro Electro Mechanical Systems, IEEE, 1993,

[73] Hopcroft, M., Nix, W., and Kenny, T., *What is the Young's modulus of silicon?* Journal of Microelectromechanical Systems, 2010, Vol. **19**, No. 2: p. 229-238

[74] Bhaswara, A., et al *Fabrication of Nanoplate Resonating Structures vis Micro-Masonry,* Journal of Miucromechanics and Microengineering, 2014, **24**, 115012

[75] Bhaswara, A., et al, *A Simple Fabrication Process based on Micro-Masonry for the realization of Nanoplate Resonators with Integrated Actuation and Detection Schemes,* Frontiers in Mechanical Engieering, section Micro- and Nanoelectromechanical Systems, **2016**, 01 March

[76] Ayela, C., and Nicu, L., *Micromachined piezoelectric membranes with high nominal quality factors in Newtonian liquid medial: a Lamb's model validation at the microscale,* Sensors and Actuators B, 2007, **123:** p 860-868

[77] Xu, T., et al., *Micromachined piezoelectric membrane-based immunosensor array* Biosensors Bioelectronics, 2008, **24**: p. 638-643

[78] Lu, X., et al, Biosensor platform based on stress-improved piezoelectric membrane, Sensors and Actuators Physics, 2012, **179**: p. 32-3882]

[79]   Cha, M., et al., *Biomolecular detection with a thin membrane transducer,* Lab on a Chip, 2008, **8**: p. 932-937

[80]   Alava, T., et al., *Silicon-based micromembranes with piezoelectric actuation and piezoresistive detection for sensing purposes in liquid media,* Journal of Micromechanics and Microengineering, 2010, **20**, 075014

[81]   Ekinci, K. L., and Roukes, M. L., *Nanoelectromechanical systems,* Review of Scientific Instruments, 2004, **76**, 061101

[82]   Schomburg, W. K., *Introduction to Microsystem Design,* Springer, Berlin, 2011

[83]   Jeong, B., et al, *Complex Nonlinear Dynamics in the Limit of Weak Coupling of a System of Microcantilever Connected by a Geometrically Nonlinear Tunable Nanomembrane, 25, 465501*

[84]   Jeong, B. et al., *Corrigendum: Utilizing intentional internal resonance to achieve multi-harmonic atomic force microscopy,* Nanotechnology, 2016, **27**, 125501

[85]   Girssible, F. J., *Advances in atomic force microscopy,* Review of Modern Physics, 2003, **75**: p. 949-983

[86]   Lavrik, N. V., Sepaniak M. J., and Datskos, P. G., *Cantilever transducers as a platform for chemical and biological sensors,* Review of Scientific Instruments, 2004, **75**: p. 2229-2253

[87]   Li, M., Tang, H. X., and Roukes, M. L., *Ultra-sensitive NEMS-based cantilevers for sensing, scanning probe and very high-frequency applications,* Nature Nanotechnology, 2007, **2**: p. 114-120

[88]   Goeders, K. M., Colton, J. S., and Bottomley, L. A., *Microcantilevers: sensing chemical interactins via mechanical motion,* Chemical Reviews, 2008, **108**: p. 522-542

[89]   Vakakis, A. F., et al, *Passive Nonlinear Targeted Energy Transfer in Mechanical and Structural Systems,* Springer, Berlin, 2008

[90]   Cho, H., et al., *Nonlinear hardening and softening resonances in micromechanical cantilever-nanotube systems originated from nanoscale geometric nonlinearities,* International Journal of Solids and Structures, 2012, **49**, 15: p. 2059-2065

[91]   Jeong, B., et al., *Modeling and measurement of geometrically nonlinear damping in a microcantilever nanotube system,* ACS nano, 2013, **10**: p. 8547-8553

[92] Jeong, J.-W., et al, *Two-Axis MEMS Scanner with Transfer-Printed High-Reflectivity, Broadband Monolithic Silicon Photonic Crystal Mirrors,* Optics Express, 2013, **21**, 13800

[93] Akiyama, S., et al, *Fabrication of highly reflecting epitaxy-ready Si-SiO$_2$ Bragg reflectors,* IEEE Photonic Technology Letters, 2005, **17**(7): p. 1456-1458

[94] Keum, H., Seong, M., Sinha, A., and Kim, Seok, *Electrostatically driven collapsible Au thin films assembled using transfer printing for thermal switching*, Applied Physics Letters, 2012, **100**, 211904

[95] Pikey, W., *Formulas for Stress, Strain and Structural Matrices, 2nd edition,* Wiley, Hoboken, NJ, 2005

[96] Spillane, S. M., Kippenberg, T. J., and Vahala, K. J., *Ultralow-threshold Raman laser using a spherical dielectric microcavity,* Nature, 2002, **415**: p. 621-623

[97] Kippenberg, T. J., and Vahala, K. J., *Cavity optomechanics: back-action at the mesoscale,* Science, 2008, **321**: p. 1172-1176

[98] Anetsberger, G., et al., *Measuring nanomechanical motion with an imprecision below the standard quantum limit,* Physical Review A, 2010, **82**, 061804

[99] Vollmer, F., Arnold, S., and Keng, D., *Single virus detection from the reactive shift of a whispering-gallery mode,* Proceedings National Academics of Science, U. S. A., 2008, **105**: p. 20701-20704

[100] Armani, D. K., Kippenberg, T. J., Spillane, S.M., and Vahala, K. J., *Ultra-high-Q toroid microcavity on a chip,* Nature, 2003, **421**: p. 925-928

[101] Knight, J. C., Cheung, G., Jacques, F., and Birks, T. A., *Phase-matched excitation of whispering-gallery-mode resonance by a fiber taper,* Optical Letters, 1997, **22**: p. 1129-1131

[102] Tas, N., Sonnenberg, T., Janse, H., and Elwenspoek, M., *Stiction in surface micromachining*, Journal of Micromechanics and Microengineering, 1996, **6**, 385

[103] Harsh, K. F., et al., *The realization and design considerations of a flip-chip integrated MEMS tunable capacitor,* Sensors and Actuators, A Physics, 2000, **80**: p. 108-118

[104] Lee, S., et al., *Heterogeneously Assembled Metamaterials and Metadevices via 3D Modular Transfer Printing,* Scientific Reports, 2016, **6**: 27621

[105] Chen, H. T., et al., *Active terahertz metamaterial devices,* Nature, 2006, **444**: p. 597-600

[106] Chen, H. T. et al., *A metamaterial solid-state terahertz phase modulator,* Nature Photonics, 2009, **3**: p. 148-151

[107] Hu, T., Padilla, W. J., Xin, Z., and Averitt, R. D., *Recent progress in electromagnetic metamaterial devices for terahertz applications,* IEEE Journal of Selected Topics in Quantum Electronics, 2011, Vol. **17**, No. 1

[108] Lee. S. H., et al., *Switching terahertz waves with gate-controlled active graphene metamaterials,* Nature Materials, 2012, **11**: p. 936-941

[109] Yao, Y. et al., *Electrically tunable metasurface perfect absorbers for ultrathin mid-infrared optical modulator,* Nano Letters, 2014, **14**: p. 6526-6532

Chapter 4.   Quantum dot film integration

4.1 Nanomaterial overview

Nanomaterial is an emerging class of material that exhibits nanometer length scale in at least one dimension. The first attempt to classify the nanostructured materials was based on the shape of the crystallites and the chemical composition of the crystallites, which is delayed by the development of novel nanomaterials such as quantum dots (QD), fullerenes, nanotubes and nanoflowers, which are not fully considered in the aforementioned classification [1,2]. Hence, Pokropivny and Skorokhod developed a contemporary mean of classification, where the nanomaterials are genuinely divided by its mere dimensions [2,3]. Depending on the dimensionality, the nanomaterials can be classified into one of the fourth, zero-dimensional (0D), one-dimensional (1D), two-dimensional (2D) and three-dimensional (3D) with elementary building blocks in 0D, 1D, and 2D [2,3].

0D materials are in the form of spheres or clusters, which are considered as point-like particles. For past 10 years, the progress in synthesis of the 0D materials (QD) in well controlled manner as well as characterization has been extensively developed and the materials have found the applications in light emitting diodes (LEDs), solar cells, single-electron transistors and lasers [4-10]. 1D materials, on the other hand, shows tube like shape with dimensions in nanometer regime in its radius. Similar with QD, 1D nanostructures have gained enormous focus owing to their unique applications in mesoscopic physics and fabrication of nanoscale devices such as interconnects and functional constituents in electronic, optoelectronic, electrochemical and electromechanical devices [11-13]. 2D materials are commonly found in sheet like format where the lateral dimensions are in the out of nanometric range and their unique characteristics that depend on shape have been the key focus in the 2D nanomaterials research. Lastly, 3D

nanostructures have been developed to utilize the extremely high surface area to volume ratio, which can be facilitated in the high absorption sites like batteries for example [14,15].

Until now, majority of the investigations in the nanomaterials have been focusing on the development and synthesis of these materials in controlled manner to tune their sizes and the incorporation of diverse class of materials. Also, understanding the physics behind the nanomaterials has also attracted many researchers and their utilization in functional devices has begun to advance. However, the wide classes of elements in nanomaterials as well as their delicate mechanical characteristics when processed in bulk scale hinders the establishment of standardized protocols of fabrication. In this aspect, transfer printing that solely relies on the mechanical process is a seemingly suitable manufacturing technique to integrates these nanomaterials into functional purposeful devices.

4.2 Quantum dot film integration

4.2.1 Background

Quantum dot (QD) is a general terminology that refers to nanometer scale semiconductor particles with compactly crowded electrons or holes in its discrete single object form factor. The QD accommodate metallic and semiconducting materials, which can be tuned in its sizes and subsequently influencing the electron-hole generation and recombination dynamics, tunneling behavior and energy transfer. An example of the size dependency in tuning can be cadmium selenium (CdSe) where 2 nm and 6 nm diameter QDs emit blue and red spectrum respectively [16]. Although numerous researches have been conducted to fully exploit the tunability asset in the colloidal QDs (c-QD), the drawback in extremely high surface area has required further attention prior to commercialization. The cations are mostly passivated by the surfactants during synthesis, but the anions remain unprotected, which is prone to oxidation in the surface level, and

consequently affect the performance of the QD based devices. Recently, capping the QD by shell with broader bandgap material has demonstrated ~ 30% improved efficiency, and the method is seemingly potential approach to fabricate numerous QD based devices in the fields of bio related applications, photovoltaic, light emitting devices, photodetectors and photocatalysts as well as common computing applications [17-22].

In addition to the tunability of the optical and electrical properties of the QDs by adjusting the sizes, the c-QDs are suspended in organic solvent, which is advantageous in the perspective of processability for device fabrication since it does not require high vacuum process. The c-QD is commonly spin casted onto the surface and subsequent thermally treated to result in conformally precipitated and crosslinked QD film on the substrate. Also, the solution based process can be modified to alter the precipitated QD film thickness by either altering the concentration of the QD in the solution, or simply adjusting the spinning rate during spin casting. Although the QD process is advantageous by its convenient solution process and cost efficiency, the above mentioned spin casting method is limited since the casting method coats the entire surface of the substrate meaning that the patterning of the c-QD layer to create individually operating pixels are unattainable. As an example, Cho and his colleagues had demonstrated a QD LED prepared by c-QD, which is pixelized by the patterning the amorphous Si (a-Si) thin film transistor (TFT) while maintaining the QD layer as a film [23]. Hence, the authors were able to construct an image by modulating the luminance by the applied voltage in each pixel. While the demonstration of image is successful, rather low pixel density as well as the limited color volume limited by a single type of QD are the challenges lie on the path to the QD based commodities.

A route to overcome is by means of transfer printing, which can selectively transfer individual QD pixel onto the receiver substrate. The first attempt was carried out by Kim and his colleagues

where the QD is spin casted onto structured PDMS with parylene-C coating, which is subsequently printed onto substrate where the QD is formed on the high topology in the PDMS as shown in **Figure 4.1** [24]. The parylene-C coating on the PDMS is utilized to overcome the chemical compatibility between the chloroform or chlorobenzene solutions and the PDMS manipulator. It was discovered that the contact angle between the chloroform and the parylene-C is reduced to 6° $\pm 1^{o}$, which guaranteed the uniform coating of the QD layer. At the same time, the parylene-C coating is a suboptimal material to facilitate the printing procedure. Although the presented technique successfully demonstrated a device fabrication with patterned QD, the limited chloroform or chlorobenzene solution limits the c-QD.
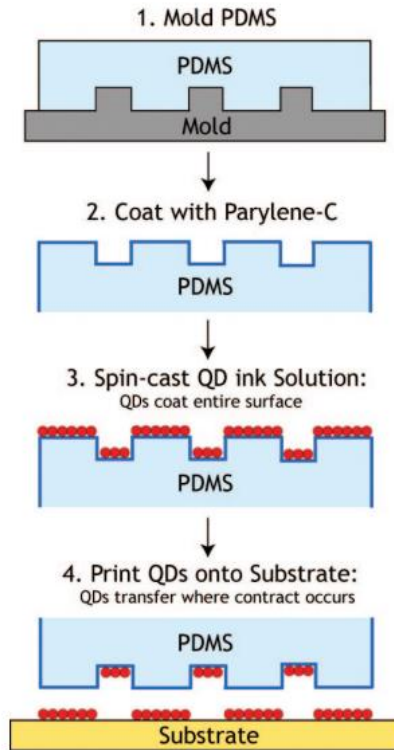
Figure 4.1 The schematic description of the patterned QD transfer [24]
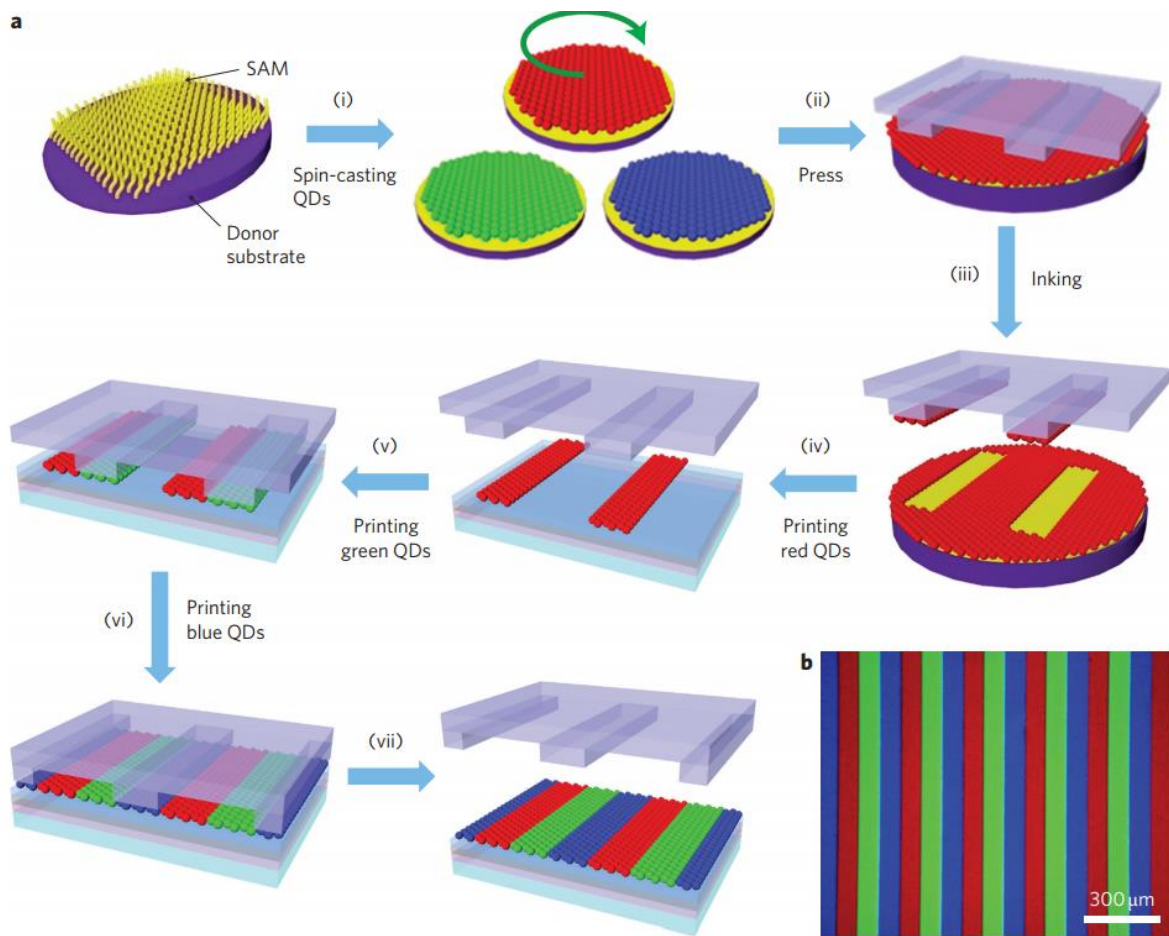
Figure 4.2 *(a) The schematic process flow of transfer printing QD stripes onto receiver substrate by ODTS SAM treatment on the donor substrate and (b) fluorescence image of the printed red, green and blue array upon exited by 365 nm UV [25]*

Hence, purely mechanical process of transfer printing of patterned QD to fabricate device fabrication had been vigorously investigated. It was first carried out by modifying the donor substrates by covalently bonded, dense, self-assembled octadecyltrichlorosilane (ODTS) monolayer and subsequently spin casting red, green and blue c-QDs [25]. Owing to the ODTS self-assembled monolayer (SAM), the surface energy is reduced to 21 mJ/m^2 from 1140 mJ/m^2, which drastically promotes the delamination of the QD from the donor substrates [26,27]. Also, the ODTS SAM layer displays roughness of ~ 0.2 nm and good wettability with the c-QD, which contributes to the uniform QD film layer [26]. The individual red, green and blue QD donor

substrate is transfer printed onto the receiver substrates with indium tin oxide (ITO), PEDOT and TFB hole transport layers to fabricate red, green and blue integrated pixels. **Figure 4.2 (a)** represents the schematic flow of the process and **Figure 4.2 (b)** represents the red, green and blue ordered array fluorescence microscopic image when exited by 365 nm UV.
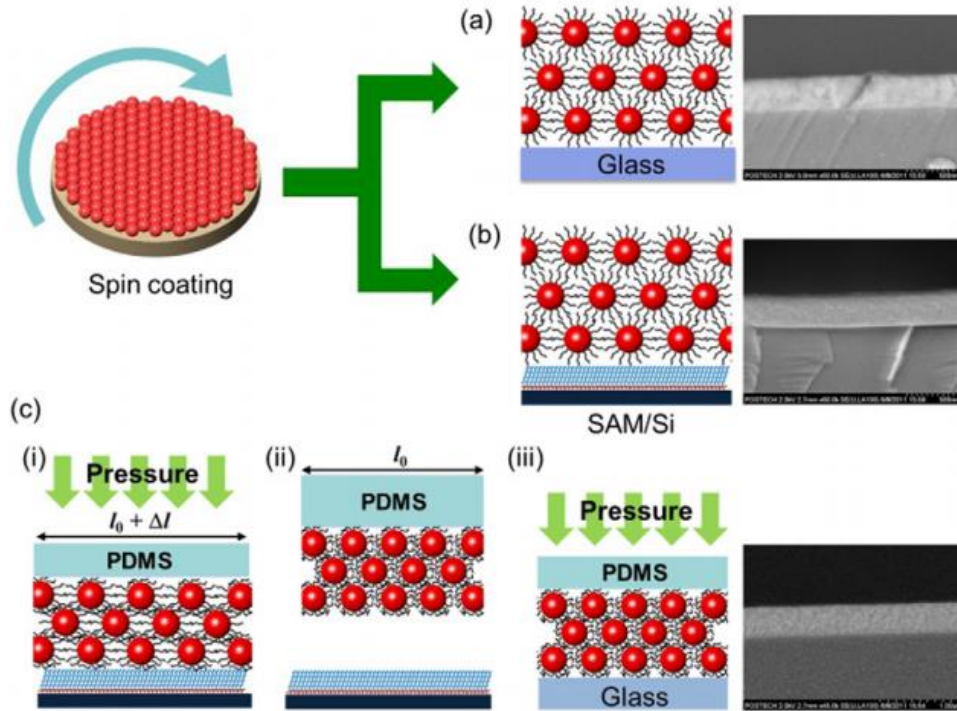
Figure 4.3 *Schematic description of three test samples and the corresponding side view SEM (a) QD on glass substrate, (b) QD on SAM treated Si substrate and (c) transfer printed QD on glass substrate [28]*

The authors further pursued to analyze the quality of the QD after transfer printing, since the transfer printing requires high preload in order to retrieve the QD from the donor substrate [28]. Three cases are studied, the c-QD coated on glass substrate, SAM treated Si substrate and transfer printed onto glass substrate as shown in **Figure 4.3 (a)** through **Figure 4.3 (c)** [28]. Through nanoindentation method, elastic modulus (*E)* and hardness (*H)* are obtained, which was found that the transfer printed QD onto glass showed ~ 25% higher elastic modulus and twice of the hardness when compared with spin casted QD film. This is attributed by the load applied during transfer

printing process, which results in compacter QD. The high density QD benefits QD devices not only in the aspect of reducing the probability of electrical shorts from pin holes, but also increases the luminous efficiency and hence enhances the brightness.

Although transfer printing QD enables heterogeneous QD materials onto prearranged format conveniently, thus permits fabrication of red, green and blue pixel with higher luminous efficiency, there still exists drawbacks in the presented structured PDMS transfer printing scheme. Although the ODTS SAM surface treatment reduces the surface energy immensely, the authors imply that high preload (greater than 98 kPa) and peeling rate (above 40 mm/s) are required to induce sufficient pull-off force to achieve close to 100 % pick up yield [25]. The dependency in the preload and the peeling rate are expected since there will be crack propagation at edge of the interface between the QD and the PDMS in the fracture mechanics view. Such high preload and pealing rate combination is often difficult to achieve. Additionally, there's resolution limitation due to the molding of the PDMS procedure as well as the sagging problem of the PDMS if the structured PDMS posts are too sparsely located. Hence, intaglio technique is proposed by Choi and his colleagues [29].

Figure 4.4 (a) describes the process flow. Similar with the transfer printing technique described above, each RGB color QD is coated on ODTS SAM treated Si substrate which is retrieved by a slab of PDMS manipulator. The QD 'inked' PDMS slab is brought to contact with an inversely patterned template (intaglio trench) to remove unwanted QD from the PDMS, which is subsequently printed onto a substrate with high resolution alignment. **Figure 4.4 (b)** shows large scale of RGB QD printed photoluminescence (PL) image that is composed of individual ~ 20 μm pixel as shown in **Figure 4.4 (c)**. Also, PL image shown in **Figure 4.4 (d)** opens a potential application in high resolution QD display. The intaglio technique circumvents the challenge in

direct transfer printing process where the high preload and pealing rates are required for ~ 100 %

pick up yield by simply contacting substantially larger area than final expected design such that

the crack propagation at the edge of the interface between QD and PDMS doesn't affect

significantly in the final patterned array.
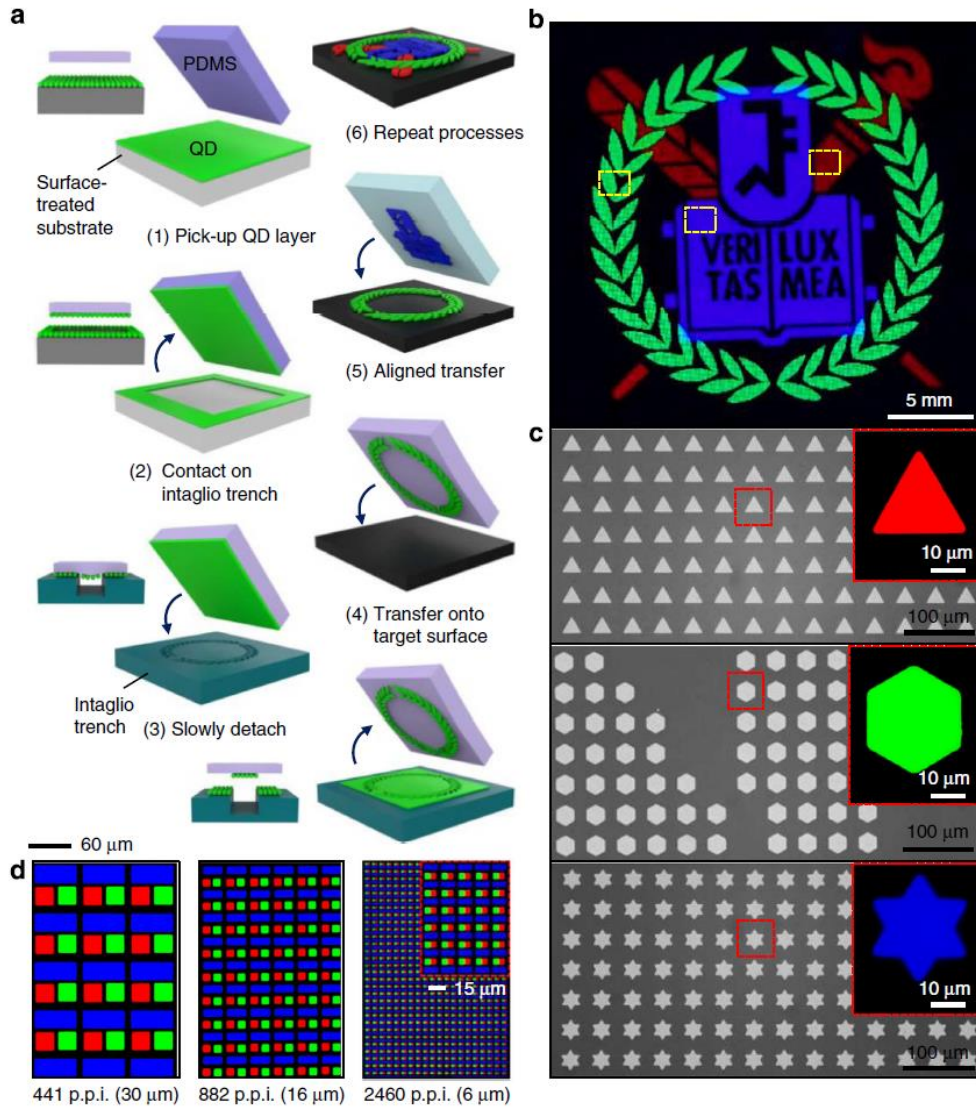
Figure 4.4 *Intaglio transfer printing schematics and high resolution RGB QLED integration demonstration (a) Schematics of process flow of intaglio transfer printing technique (b) photoluminescence (PL) image of the RGB QD pattern constructed through intaglio transfer printing (c) magnified view of each color in (b) with PL inset images (d) PL image of different pixel per inch resolution [29]*

Furthermore, the Si templates are fabricated by conventional lithography based technique, through which high resolution patterning of RGB QD and subsequent integration is achieved at ease. While the presented intaglio is a ground breaking approach for high resolution RGB QD integration, the technique suffers when integrating a single pixel where excessive amount of QD is wasted. Additionally, the process requires an intermediate step between QD donor substrate preparation and printing process where the inked PDMS is brought to contact with a negative template for patterning. The process is cumbersome in the view of mass production since the process is difficult to expand into roll to roll manufacturing scheme.

Another process developed to achieve high throughput is by integrating a polyvinylalcohol (PVA) lifting layer prior to QD coating on the ODTS SAM coated substrate as shown in **Figure 4.5 (a)** [30]. The PVA is chemically stable with cyclohexane solution, which is the commonly used solvent in c-QD. The adhesion between PVA and QDs is formed by polymer chains and organic alkyl chains adhered to the nanocrystal surface whereas the interface between the ODTS SAM and PVA is formed by ordered alkyl chains, thus allowing the delamination to occur at the interface between the ODTS and PVA layer [28,31]. Once the PVA and the QD are picked up and attached to the PDMS stamp, the inked stamp is submerged into deionized water (DI) to dissolve the PVA layer, and subsequently print the QD layer onto the target site. As shown in the plot in **Figure 4.5 (b)**, the PVA lifting layer incorporation allows consistent pick up yield without compromising with the thickness of the QD layer as long as sufficiently high preload and the pealing speed is facilitated in the pick-up process. **Figure 4.5 (c)** shown is the SEM image of the transfer printed QD layer, which appears to be crack and PVA residue free. Although the proposed method is a significant improvement in the facet of widening the transferrable QD layer thicknesses, the technique still suffers from the high preload as well as the high pealing rate of which, the

drawbacks are prescribed above. Additionally, the lifting layer incorporation utilizes dissolving step where the inked stamp is submerged in DI bath. DI is most commonly used ingredients in microfabrication, process may have an effect in the transfer printed QD thickness. The **Figure 4.5 (b)** only describes the pick-up yield on the donor substrate with wide range of QD layer thicknesses, the manuscript only describes extremely thin mono layer of QD printed onto receiver substrate and neglects commenting on the results when thick QD layer is transfer printed by consistent approach. QD layers formed from c-QDs are typically adhered to each other particles by weak intermolecular forces, which results in extremely fragile layers. Although the weak interaction is advantageous to pattern the QD layer by mechanical pealing with PDMS stamp, the thick layer of QD is potentially influenced by the incorporation of the wet process.

Although numerous transfer printing based heterogeneous integration of QD film have been demonstrated, each have their advantages and limitations. Herein, we propose a method of patterning QD layer formed from c-QD by purely mechanical means in dry condition that requires little preload and the pealing rate. The patterned QD substrate is analogous with donor substrates in deterministic transfer printing, which can potentially be transfer printed onto nearly any class of substrate material for heterogeneous integration. The challenge with pick-up yield can be overcome by having structured PDMS stamp that is slightly larger in lateral dimension than the QD pattern such that the crack initiation at the edge is fully avoided [32]. By clearly distinguishing the donor substrate preparation step, the patterned QD can be transfer printed in scalable manner conveniently.
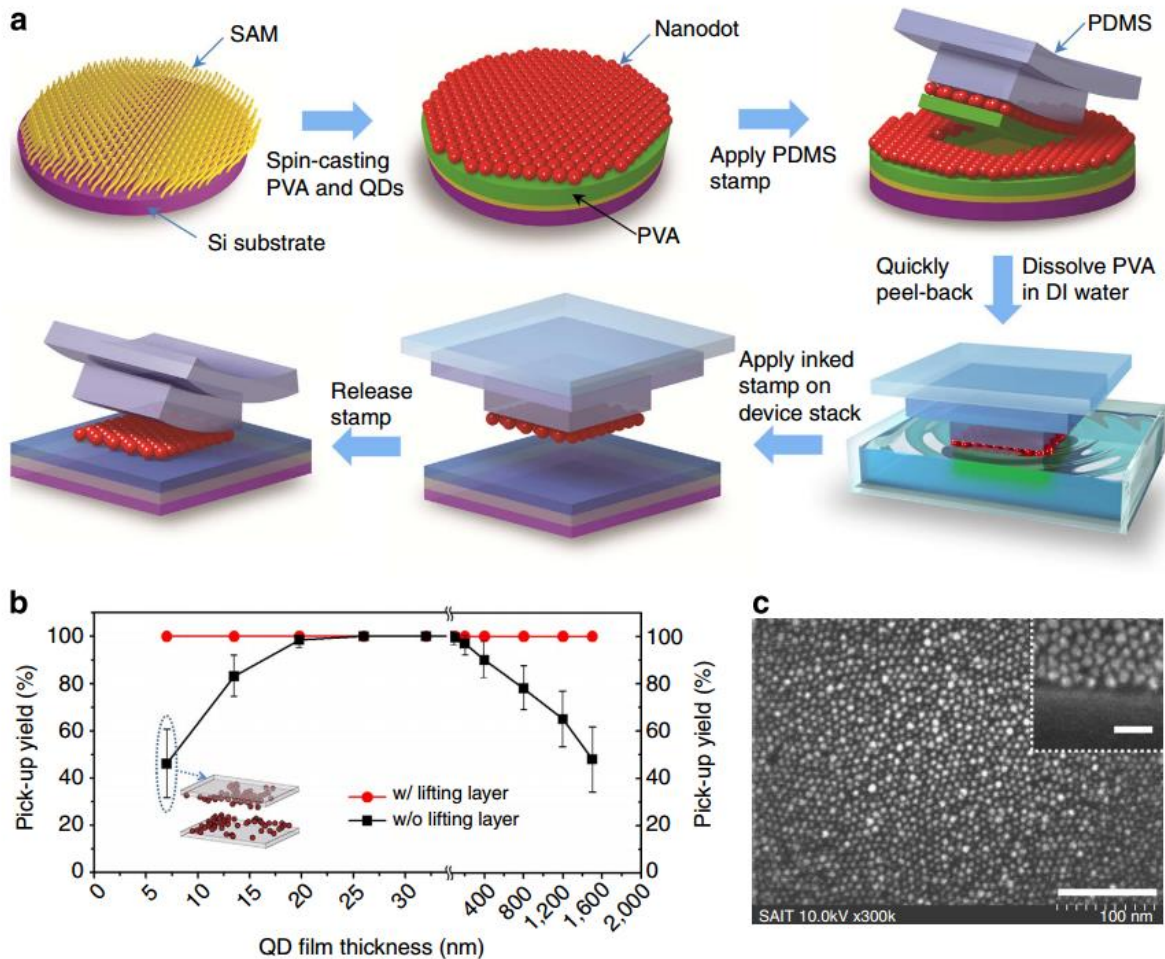
Figure 4.5 *PVA lifting layer assisted transfer printing schematics and its results (a) Schematic process flow of the PVA lifting layer transfer printing (b) pick up yield with respect to the QD thickness with and without the lifting layer (c) SEM image of the QD monolayer transferred using the PVA lifting layer technique [30]*

4.2.2 Quantum dot film patterning by a shape memory polymer

The mechanical patterning of the QD layer is strongly depend on the adhesion between the QD layer and the stamping material. Until now, all the methods utilized PDMS as a stamp material which had been successfully demonstrated its capability of transfer printing by kinetically controlling the adhesion energy between the transferring QD layer and the stamp. However, our approach is in separating the transfer printing and the patterning, which is similar with the deterministic transfer printing process. Hence, the option for patterning material is not bounded with PDMS.

A shape memory polymer (SMP) is a class of thermosensitive materials that change their mechanical compliance across the polymer's glass transition or melting temperature (T_g or T_m) [34,35]. The reversibility in the elastic modulus can be fully exploited to provide conformal contact and high pull-off force, useful for transfer printing and patterning [36]. The high elastic modulus of SMP at below T_g point is advantageous in patterning purpose in two perspectives. Firstly, pull off force that the SMP stamp exhibits against a rigid surface during separation can be expressed as [37]

$$F_{pull-off} = \sqrt{25.31\gamma_0(2E_{smp})L^3}$$

<div align="right">*(4-1)*</div>

where γ_0 is the work of adhesion between the SMP stamp and a rigid surface, E_{smp} is the elastic modulus and L is the width of the SMP stamp. As described in **Equation (4-1)**, the pull-off force is in proportional relationship with the elastic modulus, which can be increased by the higher elastic modulus of the SMP below T_g. Secondly, Yuan and his colleagues had presented normal pull-off stress distribution analytically, which shows more uniform distribution with higher elastic modulus [32]. Therefore, the reversibility of the SMP works favorable in the aspect of dry mechanical patterning.

Figure 4.6 depicts process flow of the QD patterning through structured SMP and its optical and SEM images [33]. In consistency with other transfer printing QD processes, the QD is spin casted on ODTS coated Si substrate and its optical image is presented (**Figure 4.6 (a)**). Separately, similarly with PDMS stamp fabrication, structured SMP is molded and its SEM image is presented (**Figure 4.6 (b)**). The two elements are brought to contact while the SMP stamp is heated above T_g with preload for conformal contact (**Figure 4.6 (c)**) and subsequently cooled below T_g to fix the SMP stamp configuration with high elastic modulus (**Figure 4.6 (d)**). Once the SMP stamp is fully

cooled, the SMP is removed from the QD donor substrate which results in removed QD region as depicted in **Figure 4.6 (e)**. The peeling velocity was conducted at considerably lower velocity at ~ 2 μm/s, which sufficiently provide pull-off force to remove the QD.
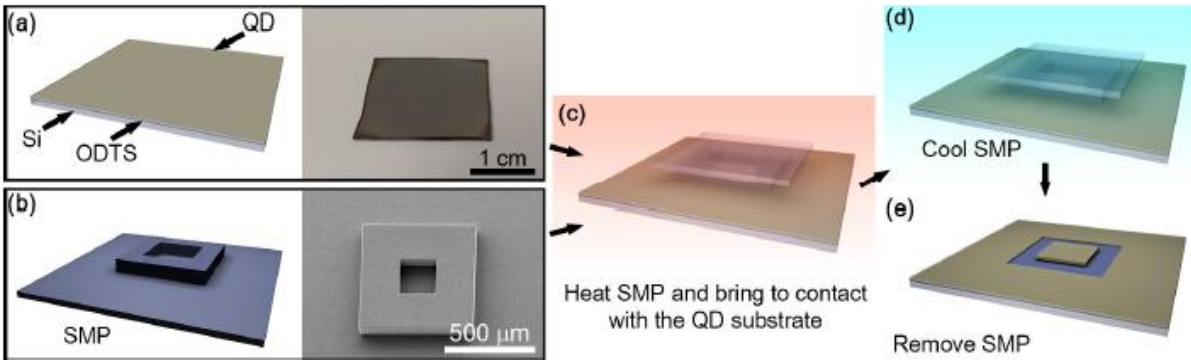
Figure 4.6 *Schematic process flow of QD patterning using an SMP stamp (a) An ODTS and QD ccoated Si substrate is prepared with a photograph (b) Structured SMP stamp is prepared separately with its SEM image (c) the SMP stamp is heated above T_g and brought to contact with the QD substrate (d) cool the stamp below T_g (e) the QD is removed at contact site upon removal of the SMP stamp [33].*

In order to fully investigate the effect of the elastic modulus of SMP in QD patterning, three different controlled experiments are conducted as shown in **Figure 4.7**. The first attempt was to make contact and separate at room temperature (below T_g) which shows irregular shape of the patterned region (**Figure 4.7 (a)**). Additionally, the SEM image reveals that the solid-like SMP stamp with high elastic modulus swept the QD resulting in thicker aggregated region on the right. **Figure 4.7 (b)** is a situation when the contact and separation both are conducted at elevated temperature (above T_g), which shows moderately patterned square at the center, yet, substantial amount of QD remains in the contacting site. Lastly, **Figure 4.7 (c)** represents the contacting at above T_g and cooled to room temperature (below T_g) prior to separation, which results in sharp contrast between the remaining QD square and its surrounding. Another important aspect worth to mention is that the operating parameters are ~ 5.5 kPa of preload and 2 μm/s separation rate, which are substantially lower than previously demonstrated QD transfer printing processes.
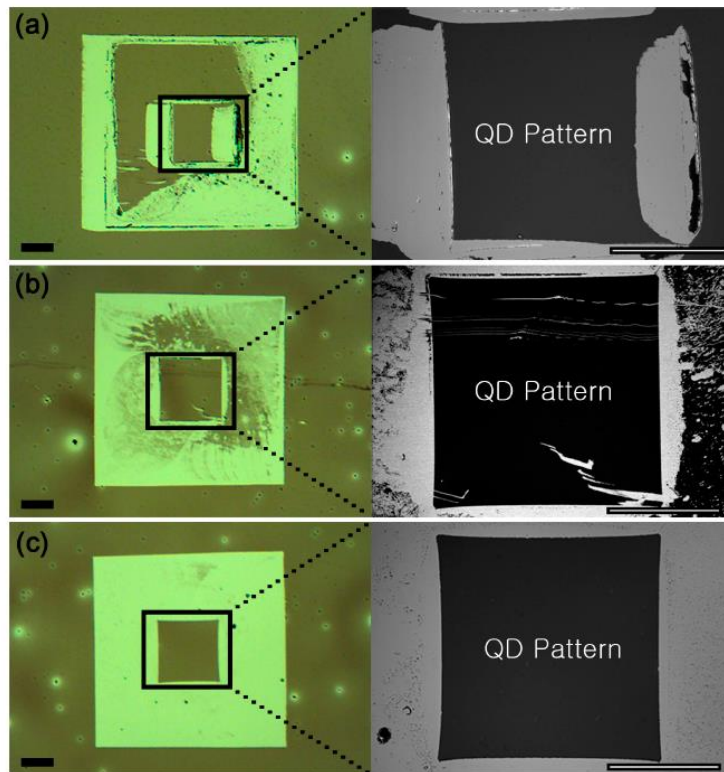
Figure 4.7 Optical and its corresponding SMP images of the boxed region (a) The contacting and separation are both conducted at a temperature below T_g (b) Both contact and separation are conducted at above T_g (c) the stamp is heated above T_g prior to contact, which is subsequently cooled to room temperature (below T_g) prior to separation. All experiments were conducted at consistent preload (~ 5.5 kPa) and separation rate (~ 2 μm/s). All scale bars indicate 100 μm. [33].

The patterned QD is examined by SEM and PL measurements included in **Figure 4.8** [33]. The SEM image in **Figure 4.8 (a)** represents clear edge line between the patterned QD and the exposed Si substrate with sharp edge, and the QD patterned region is shown in extremely high resolution to observe if any crack is induced during the SMP patterning process (**Figure 4.8 (b)**). The process does not physically contact the remaining QD region, which results in compactly dense and crack free QD patterned region. The pattern is further examined by PL intensity mapping (**Figure 4.8 (c)**) that matches the SEM image (red region in the image) with black region representing non-luminescing exposed Si region. Lastly, the QD pattern is cross-confirmed with

the solution state c-QD and background by observing PL intensity, where the QD pattern PL peak

closely matches with the solution state peak.
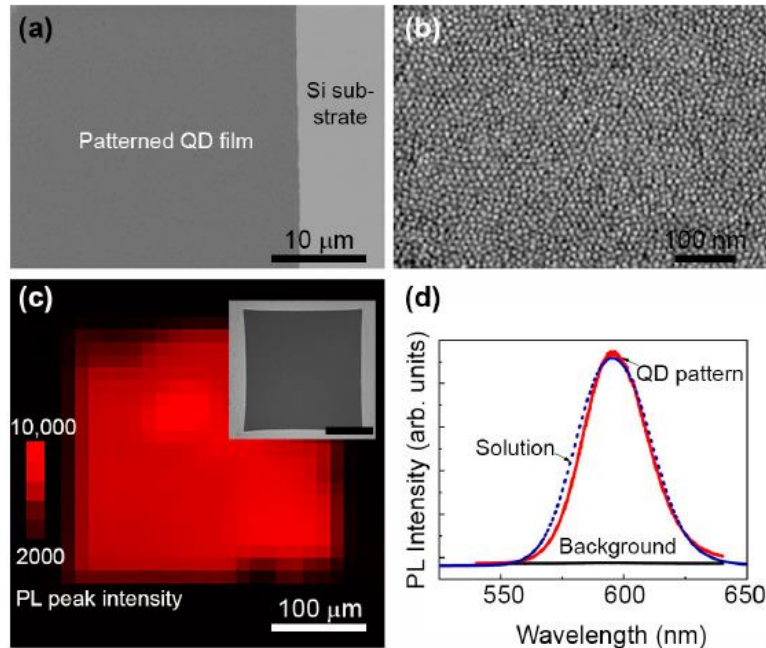
Figure 4.8 QD pattern examination by SEM and PL measurements. (a) SEM image of the patterned QD edge clearly shows the distinction between the QD pattern region and the Si substrate (b) high magnification of the QD pattern region shows compact, dense and crack-free QD (c) PL mapping is also consistent with the SEM image (inset) and (d) PL intensity spectrum peak also matches with the solution state c-QD [33].

Lastly, scalability of the SMP patterning is further testified by first preparing 1.2 cm x 1.2

cm lateral dimension SMP square arrays with 200 μm x 200 μm square cavity as shown in **Figure**

4.9 (a) SEM [33]. The stamp is utilized to make array of 200 μm x 200 μm square QD patterns as

shown in optical image (**Figure 4.9 (b)**). The inset image in **Figure 4.9 (b)** shows defect free

square QD patterns. The proposed SMP QD patterning scheme is carried out with low preload (~

5.5 kPa) and peeling rate (~ 2 μm/s) by fully exploiting the reversibility characteristic of SMP.

The patterned QD can be viewed as "inks" on the donor substrate, which can be transfer printed

onto diverse material surfaces with a structured stamp (single post or multiple posts) with larger

lateral dimension for high pick-up yield. Furthermore, with development of higher surface energy SMP can utilize the proposed SMP patterning scheme to pattern QD on the spin casted substrate, which can be directly used as functional devices.
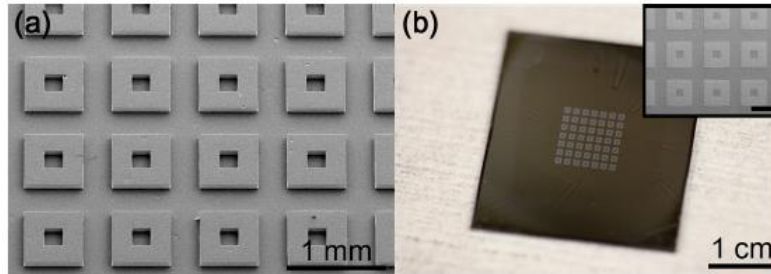
Figure 4.9 *Scalability demonstration of the SMP QD patterning scheme. (a) SEM image of the SMP array posts with 200 μm x 200 μm cavity and (b) optical image of the large array QD pattern with inset indicating clear square QD patterns. The scale bar in the inset represents 600 μm [33].*

4.2.3 **Quantum dot film patterning by photoresist stamping**

Photolithography technique is possibly a single major micro / nano manufacturing technique with its capability in defining extremely high resolution and the scalability for efficient mass production, which direct adaptation of the well-established photolithography in QD patterning would be fortunate. Yet, the vital issue with the wet process hinders the utilization of the photolithography process. The QD substrates are patterned for subsequent convenient transfer printing process, thus exhibiting extremely low adhesion with the surface. While the low adhesion behaves favorable in the scope of transfer printing, it bounds the some of the commonly utilized micromanufacturing techniques, i.e. spin casting to register PR layer as well as wet process for developing or wet chemical etching, which can potentially affect the QD films. Therefore, development of dry and non-detrimental method to pattern is required while maintaining the resolution limit on par with the photolithography process. In this view, a composite stamp which is composed of PDMS slab support with patterned PR surface is studied as plausible new stamp

design for QD patterning process. The method is inspired from detachment lithography process where the PR and PDMS slab is explored in its feasibility in the micromanufacturing field [37].

The schematics of process flow is presented in **Figure 4.10**. PR pattern on PDMS slab support and the QD film on ODTS SAM treated Si substrate are separately prepared. The PDMS slab serves as a body to handle PR layer conveniently while the compliant material property allows conformal contact with the surface by minimal preload. The PR layer, on the other hand, is the utilitarian layer that patterns the QD film on the opposing surface, which is processed through photolithography that ensures high resolution features. The two constituents are brought together with PR pattern facing the QD film layer, with minimal preload to establish full contact, which is subsequently peeled off to remove QD at the contacting region.
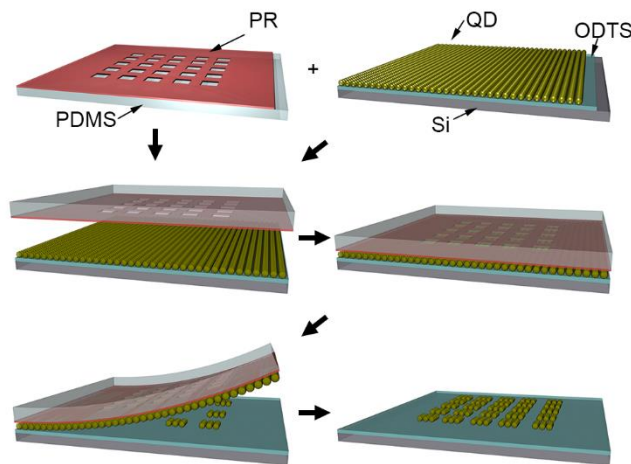
Figure 4.10 *Schematic process flow of the QD patterning through PR stamping process. First, the PDMS slab support with PR pattern on top and the QD on ODTS SAM treated Si substrate are separately prepared. The two are brought to contact with PR layer facing QD and subsequent separation of the composite layer results in the QD on the donor substrate.*

The utilization of the PR layer is favorable in two aspect. Firstly, the higher elastic modulus of the PR upon full curing yields rather uniform stress distribution when compared with similarly structured PDMS stamp as shown by FEA simulation in **Figure 4.11**. The **Figure 4.11 (a)** is the

top view of the PDMS and PR substrate while the **Figure 4.11 (b)** is the side view of the same structure which only display z-direction (normal to the stamping material) stress. The mechanical characteristics of the QD is unknown, hence replaced with Si substrate mechanical properties with $E \sim 170$ GPa, with Poisson's ratio (v) ~ 0.22 for both simulations. Identical pull off force is applied on the PDMS and PR region which yields substantial amount of stress distribution difference in case of PDMS and the PR situations. Small regions at the interface between the PDMS and the substrate experiences significantly high normal stress, while most of the contacting area suffers from low normal stress. This non-uniformity is attributed by the lower E, which deforms prior to physically inducing the pull-off force at the substrate as analytically described by Yuan [32].
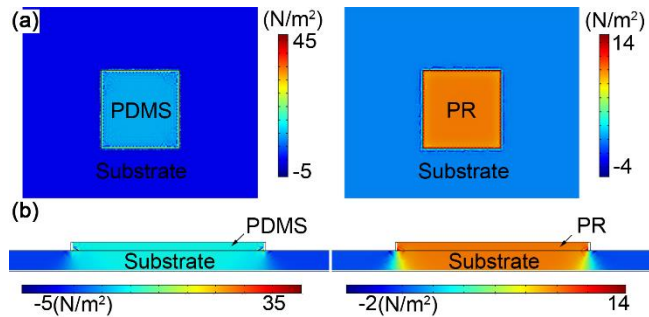

Figure 4.11 *Schematic process flow of the QD patterning through PR stamping process. First, the PDMS slab support with PR pattern on top and the QD on ODTS SAM treated Si substrate are separately prepared. The two are brought to contact with PR layer facing QD and subsequent separation of the composite layer results in the QD on the donor substrate.*

In addition to observing the stress distribution, we also investigated the work of adhesion (W_a) between the PR and the QD and compared with that of the PDMS and the QD. The thermodynamic work of adhesion is calculated from contact angle measurements of some probe liquids that describes free energy difference per unit normal area between the two phases concerned in contact at equilibrium and entirely separate in vacuum [38-40]. Hence, the work of adhesion fully describes the energy required for fracture, i.e. energy release rate since the energy release rate incorporates irreversible energy dissipated during the fracture. However, there's strong

correlation between the work of adhesion, where the small difference in work of adhesion can result in an order difference in the work of fracture. Therefore, investigating on this work of adhesion is worthwhile to pursue [41-43]. The work of adhesion by two solid adhering surfaces is analytically described by

$$W_{12} = \frac{4\gamma_1^d \gamma_2^d}{\gamma_1^d + \gamma_2^d} + \frac{4\gamma_1^p \gamma_2^p}{\gamma_1^p + \gamma_2^p}$$

(4-2)

where γ represents the surface energy and d and p denote the dispersion and polar components of surfaces 1 and 2. However, each component is often unknow, therefore requires quantification by contact angle measurements through

$$\gamma_1(1 + cos\theta) = 2\sqrt{\gamma_s^d \gamma_l^d} + 2\sqrt{\gamma_s^p \gamma_l^p}$$

(4-3)

where s and l represent solid and liquid components. Since γ_l^d and γ_l^p are known for water and ethylene glycol ($\gamma_{water}^d = 23.9$, $\gamma_{water}^p = 48.8$, $\gamma_{ethylene\ glycol}^d = 29.2$ and $\gamma_{ethylene\ glycol}^p = 18.3$ mJ/m^2), two independent experiments with the liquids yields dispersion and polar components of the solid surface [44]. The experiments are carried out by goniometer against QD substrate, PR, PDMS, ODTS and Si substrates and their contact angles and corresponding work of adhesions are listed in **Table 4.1** and **Table 4.2**.

Table 4.1 Contact angle measurements of Ethylene glycol and water against various surfaces. The values are in angle (°)

	QD	PR	PDMS	ODTS	Si
Ethylene Glycol	78.3	37.5	75.8	86.71	43.9
Water	99.5	67.88	99.7	113.74	77.3

Table 4.2 *Work of adhesion calculated through* **Equation** *(4-2) between two adhering surfaces*

Material combination	Work of adhesion (mJ/m^2)
ODTS – QD	40.43
QD – PDMS	40.95
QD – PR	47.67
PR – PDMS	49.95
QD – Si	50.93

The QD – Si work of adhesion measurement was conducted as a reference since the QD patterning through PR on Si substrate has always been unsuccessful. The work of adhesion values reveal that there's small difference between the ODTS – QD interface and QD – PDMS interface, which explains why it requires substantially high preload and peeling rate that fully exploits the characteristics of the kinetically controlled adhesion in order to successfully pattern the QD. However, the QD – PR interfaces shows ~ 18 % higher work of adhesion, which leads to convenient QD patterning regardless of the preload and peeling rate. Additionally, the PR – PDMS interface exhibits slightly higher work of adhesion, which ensures that fracture occurs at the interface between ODTS and QD instead of PR – PDMS interface. Although the absolute difference in the work of adhesion is miniscule, Penn and Defex found the relationship between work of adhesion and the work of interfacial fracture by [43]

$$W_{fracture} = 91.3 \left(e^{0.033 W_a} \right) \qquad \qquad (4\text{-}4)$$

through experimentally obtaining data and finding the trend line, which implies that the effect of ~ 18% difference in work of adhesion can hugely affect the work of fracture.

Figure 4.12 represents optical images and SEM images of the QD patterned results. **Figure 4.12 (a)** is an array of PR pattern on PDMS, which is directly replicated on QD surface. The

individual squares are 12 μm x 12 μm, which is defined without any defects as can be seen higher

magnification optical image in the inset. **Figure 4.12 (b)** represents rather complex star shaped

pattern in various scales to demonstrate that QD patterning through PR is potentially scalable to

larger patterns as well. **Figure 4.12 (c)** is an SEM image of the corner showing sharp corner and

magnified view reveals clean and undamaged QD particles in the patterned region.
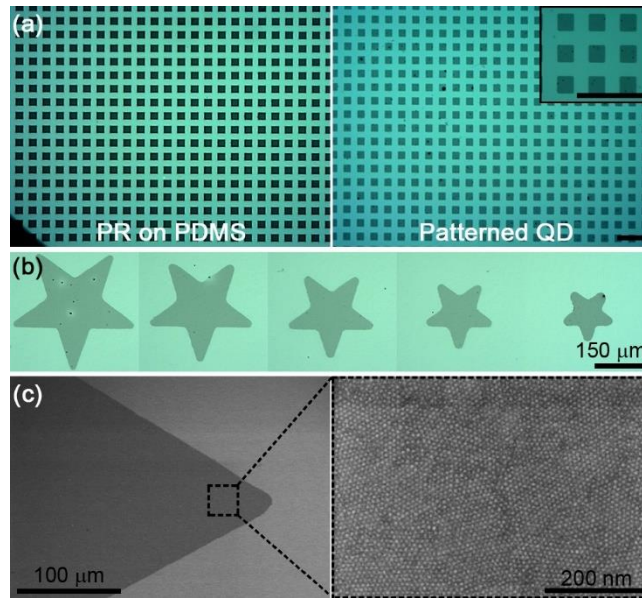
Figure 4.12 *Optical and SEM images of the patterned QD through PR stamping. (a) optical images of PR pattern on PDMS slab support formed through photolithography, which is directly replicated on QD substrate by PR stamping procedure. The inset is high magnification optical image, which shows clear patterns of individual squares. The scale bars indicate 50 μm. (b) demonstration of scalability of the PR stamping procedure with complex star shape (c) SEM image of a corner and high magnification view that shows compactly remaining QD particles in patterned region.*

Additionally, photoluminescence images are taken to demonstrate the capability of PR

stamping in all three-different color QDs as shown in **Figure 4.13 (a)** and **Figure 4.13 (b)**. Three

individual colored QDs are spin coated on ODTS and SAM treated Si substrate which are

subsequently patterned into various dimensions as shown in circle, triangle and star. Additionally,

to highlight the capability of complex configuration, UIUC letter is patterned on red QD substrate

(Figure 4.13 (a)). **Figure 4.13 (b)** is high resolution (12 μm x 12 μm) pixel patterning in large array. Lastly, PL intensity measurement is conducted, which clearly distinguishes different intensity peaks in red, green and blue (**Figure 4.13 (c)**).
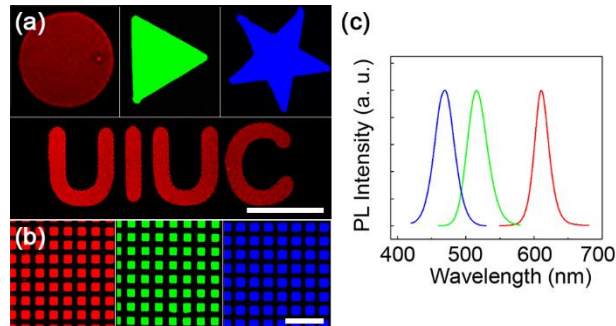
Figure 4.13 Photoluminescence images of various shape in red, green and blue QD and its PL intensity spectra. (a) Red, green and blue QD substrates are individual prepared which is subsequently patterned into circle, triangle, star and 'UIUC' letter through PR stamping procedure. (b) Additionally, small 12 μm x 12 μm square pixel arrays are formed (c) PL intensity spectra with respect to wavelength reveals the clear distinction between the three different colors. All scale bars represent 50 μm

The patterned individual QD pixels are vertically stacked by transfer printing technique with PDMS stamp with lateral dimensions slightly larger than the pixel as shown in **Figure 4.14**. The **Figure 4.14 (a)** is an optical microscopic image and **Figure 4.14 (b)** is the photoluminescence image. The heterogeneous integration of multiple colors vertically without PR patterning is an efficient means of transfer printing individual pixel since transfer printing by utilizing single post structured PDMS would collapse when such high preload (> 100 kPa) is applied, which damages the surrounding QD film. On the other hand, intaglio technique requires picking up the whole QD layer and subsequently removing the unnecessary QD, which will remove substantial amount of QD. Hence, patterning through PR stamping and subsequent transfer printing by structured PDMS is a plausible candidate to heterogeneously integrate different materials in spatially prearranged format.
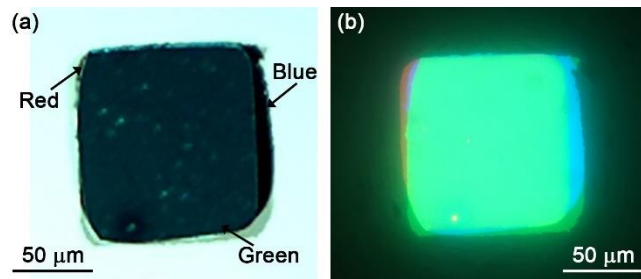
Figure 4.14 optical image of vertically stacked 100 μm x 100 μm red, green and blue pixel (a) optical image and (b) photoluminescence image

Furthermore, the detachment of PR pattern from PDMS slab support is utilized to pattern the QD layer in composite format. The surface energy of PDMS is inversely related with temperature, which leads to reduced work of adhesion between PDMS and photolithographically patterned PR layer [45-47]. This phenomenon is facilitated to detach the PR layer from PDMS and print onto the QD layer on ODTS treated Si substrate. This formation of PR masking layer on the QD substrate is conducted in dry condition, which works as great advantageous in the view of micromanufacturing since the opening region in QD can be subsequently processed to add other functional layers by PVD method. For demonstrative purpose, 5 nm Cr adhesive layer and 100 nm of Au are deposited on the QD substrate with PR masking layer. The deposited substrate is laminated with commercially available Scotch^{TM} tape, which makes contact with higher topology surfaces (where metal layer is deposited on PR masking layer). Subsequent separation of the substrate with the tape results in perfectly patterned composite QD and metallic pixels, with no QD residues in between each pixel (**Figure 4.15 (a)**). This is because the interface between the QD and detached PR is unaltered during the process, and maintains strong adhesion. The composite ink formation finalizes a donor substrate procedure, which can be utilized in transfer printing process. **Figure 4.15 (b)** is optical images taken during the process, where the PR pattern on PDMS is consistent with the final composite ink. Although Cr and Au are not frequently utilized

124

material in QD devices due to mismatch in the work function, the composite ink formation is an alternative tool to process QD into ink format in dry manner.
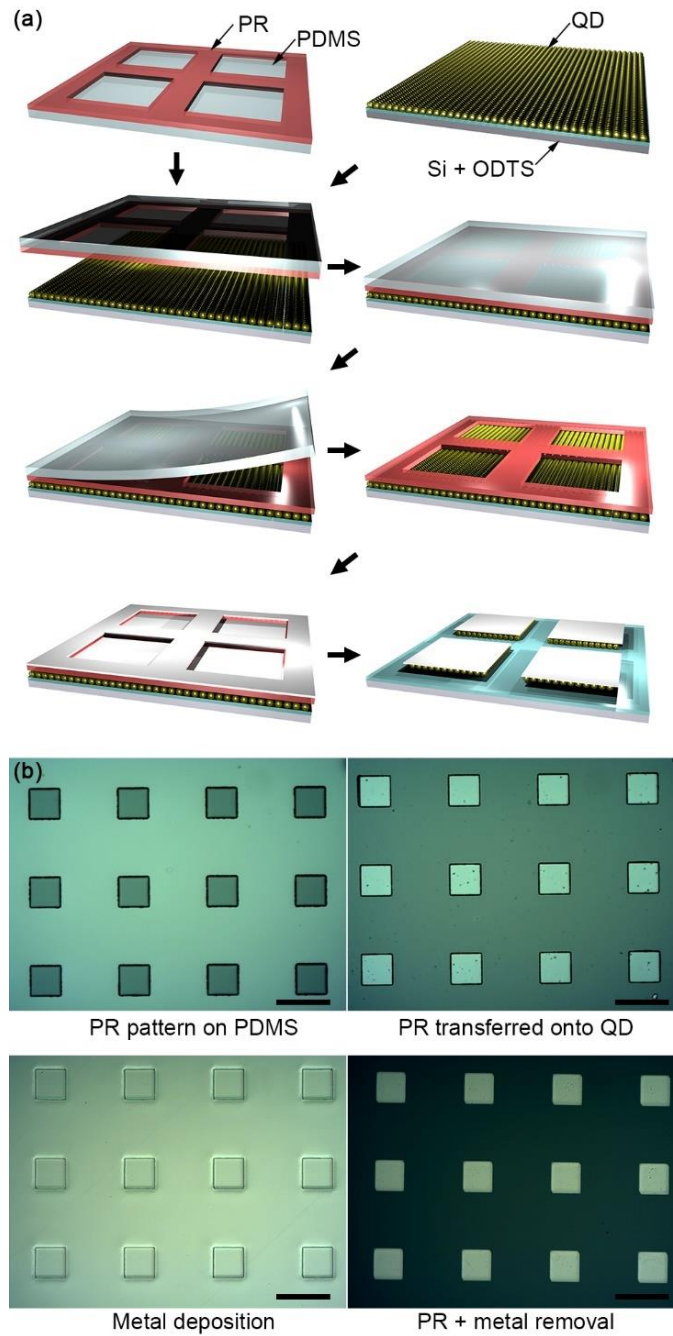

Figure 4.15 *QD and metal composite ink fabrication through detachment of PR pattern from PDMS support (a) schematic of the process flow (b) optical image of the PR pattern on PDMS,*

Figure 4.15 *(continued)*
after transferred onto QD substrate, after 5 nm Cr and 100 nm Au deposition and final removal of the PR and metal layer using tape. All scale bars represent 100 μm.

4.3 **References**

[1]   Gleiter, H., *Nanostructured materials: basic concepts and microstructures,* Acta materialia, 2000, **48**.1: p. 1-29

[2]   Tiwari, J. N., Tiwari, R. N., and Kim, K. S., *Zero-dimensional, one-dimensional, two-dimensional and three-dimensional nanostructured materials for advanced electrochemical energy devices,* Progress in Materials Science, 2012, **57**.4: p. 721-803

[3]   Pokropivny, V. V., and Skorokhod, V. V. *Classification of nanostructures by dimensionality and concept of surface forms engineering in nanomaterial science,* Materials Science and Engineering: C, 2007, **27**.5: p. 990-993

[4]   Kim, Y.-T., et al., *Electrochemical Synthesis of CdSe Quantum-Dot Arrays on a Graphene Basal Plane Using Mesoporous Silica Thin-Film Templates*, Advanced Materials, 2010, **22**.4: p. 515-518

[5]   Ledentsov, N. N., et al., *Quantum dot heterostructures: fabrication, properties, lasers (Review),* Semiconductors, 1998, **32**. 4: p. 343-365

[6]   Zhang, G., and Wang, D., *Fabrication of Heterogeneous Binary Arrays of Nanoparticles via Colloidal Lithography*, Journal of American Chemical Society, 2008, **130**: p. 5616-5617

[7]   Stouwdam, J. W., Janssen, R. A. J., *Red, green and blue quantum dot LEDs with solution processable ZnO nanocrystal electron injection layers,* Journal of Materials Chemistry, 2008, **18**.165: 1889-1894

[8]   Lee, W., et al., *TiO$_2$ nanotubes with a ZnO thin energy barrier for improved current efficiency of CdSe quantum-dot-sensitized solar cells,* Nanotechnology, 2009, **20**.33: 335706

[9]   Mokerov, V. G., et al., *New quantum dot transistor*, Nanotechnology, 2001, **21**.4: 552

[10]   Ustinov, V. M., et al., *Long-wavelength quantum dot lasers on GaAs substrates,* Nanotechnology, 2000, **11**.4: 397

[11]   Xia, Y., et al., *One-Dimensional Nanostructures: Synthesis, Characterization, and Applications,* Advanced Materials, 2003, **16**, no. 5: p. 353-389

[12]   Wang, Z. L., *Charracterizing the Structure and Properties of Individual Wire-Like Nanoentities,* Advanced Materials, 2000, **12**, 17, 1295

[13]   Hu, J., Odom, T. W., and Lieber, C. M., *Chemistry and Physics in One Dimension: Synthesis and Properties of Nanowires and Nanotubes*, Accounts of Chemical Research, 1999, **32**: p. 435-445

[14]   Simon, P., and Gogotsi, Y., *Materials for electrochemical capacitors*, Nature Materials, 2008, **7**, 11: p. 845-854

[15]   Hu, C.-C., et al., *Design and tailoring of the nanotubular arrayed architecture of hydrous RuO2 for next generation supercapacitors*, Nano Letters, 2006, **6**, 12: p. 2690-2695

[16]   Parak, W. J., et al., *Quantum dots. In: nanopraticles: from theory to application, (Schmid G. ed)* Weinheim, Wiley, 2004

[17]   Hines, M. A., and Guyot-Sionnest, P., *Synthesis and Characterization of Strongly Luminescing ZnS-Capped CdSe Nanocrystals*, Journal of Phyysical Chemistry, 1996, **100**. 2: p. 468-471

[18]   Ohara, P. C., Leff, D. V., Heath, J. R., and Gelbart, W. M., *Crystallization of Opals from Polydisperse Nanopartices*, Physical Review Letters, 1995, Vol. **75,** No. 18: p. 3466-3470

[19]   Whetten, R. L., et al., *Nanocrystal Gold Molecules*, Advanced Materials, 1996, **8**, 5: p. 428-433

[20]   Berg, D., *Quantum dot heterostructures: fabrication, properties, lasers (Review)*, Semiconductors, 1998, Vol. **32**, Number 4.

[21]   Collier, C. P., et al., *Reversible Tuning of Silver Quantum Dot Monolayers Through the Metal-Insulator Transition,* Science, 1997, Vol. **277**: p. 1978-1981

[22]   Murray, C. B., Kagan, C. R., and Bawendi, M. G., *Self-Organization of CdSe Nanocrystallites into Three-Dimensional Quantum Dot Superlattices,* Science, 1995, Vol. **270**: p. 1335-1338

[23]   Cho, K.-S., et al, *High-performance crosslinked colloidal quantum-dot light-emitting diodes*, Nature Photonics, 2009, Vol. **3**: p. 341-345

[24]   Kim, L., et al., *Contact printing of quantum dot light-emitting devices,* Nano Letters, 2008, **8**. 12: p. 4513-4517

[25]   Kim, T.-H., et al, *Full-colour quantum dot displays fabricated by transfer printing,* Nature Photonics, 2012, Vol. **5**: p. 176 - 182

[26]   Kim, D.-H., et al, *Tunable crystal nanostructures of pentance thin films on gate dielectrics processing surface-ordered control,* Advanced Functional Materials, 2008, **18**: p. 1363-1370

[27]   Kim, T.-H., et al, *Printable, flexible, and stretchable forms of ultrananocrystalline diamond with applications in thermal management,* Advanced Materials, 2008, **20**: p. 2171-2176

[28]   Lee, S., Yoon, D., Choi, D., and Kim, T.-H., *Mechanical characterization of high-quality quantum dot arrays via transfer printing*, Nanotechnology, 2013, **24,** 025702

[29]   Choi, M. K., et al., *Wearable red-green-blue quantum dot light-emitting diode array using high-resolution intaglio transfer printing*, Nature Communications, 2015, **6**, 7149

[30]   Kim, T.-H., et al., *Heterogeneous stacking of nanodot monolayers by dry pick-and-place transfer and its applications in quantum dot light-emitting diodes*, Nature communications, 2013, **4**, 2637

[31]   Meredig, B., Salleo, A., and Gee, R., *Ordering of poly(3-hexaylthiophene) nanocrystallites on the basis of substrate surface energy,* ACS Nano, 2009, **3**: p. 2881-2886

[32]   Yuan, H., et al., *Interfacial stress analysis of a thin plate bonded to a rigid substrate and subjected to inclined loading*, International Journal of Solids and Structures, 2007, **44**, 16: p. 5247-5271

[33]   Keum, H., et al., *Solvent-Free Patterning of Colloidal Quantum Dot Films Utilizing Shape Memory Polymers,* MDPI Micromachines, 2017, **8**, 18

[34]   Zhao, Q., Qi, H. J., Xie, T., *Recent progress in shape memory polymer: New behavior, enabling materials, and mechanistic understanding,* Progress in Polymer Science, 2015, **49**: p. 79-120

[35]   Eisenhaure, J. D., Xie, T., Varghese, S., and Kim S., *Microstructured shape memory polymer surfaces with reversible dry adhesion,* ACS Applied Material Interfaces, 2013, **5**: p. 7714-7717

[36]   Eisenhaure, J. D., et al., *The use of shape memory polymers for microassembly by transfer printing,* Journal of Microelectromechanical Systems, 2014, **23**: p. 1012-1014

[37]   Yeom, J., Shannon, M. A., *Detachment Lithography of Photosensitive Polymers: A Route to Fabricating Three-Dimensional Structures*, Advanced Functional Materials, 2010, **20**.2: p. 289-295

[38]   Packham, D. E., *Work of adhesion: contact angles and contact mechanics,* International Journal of Adhesion and Adhesives, 1996, **16**: p. 121-128

[39]   Brown, H. R., *The Adhesion Between Polymers,* Annual Reviews in Material Science, 1991, **21**: p. 463-489

[40]   Kendall, K., *Adhesion: Molecules and Mechanics,* Science, 1994, Vol. **263**: p. 1720-1725

[41]   Okamatsu, T., YUasuda, Y., and Ochi, M., *Thermodynamic Work of Adhesion and Peel Adhesion Energy of DimethoxysilyI-Terminated Polypropylene Oxide/Epoxy Resin System Jointed with Polymeric Substrates,* Journal of Applied Polymer Science, 2001, Vol. **80**, Issue 11: p. 1920-1930

[42]   Gent, A. N., and Lai, S.-M., *Interfacial bonding, energy dissipation and adhesion* Journal of Polymer Science Part B: Polymer Physics, 1994, **32**.8: p. 1543-1555

[43]   Penn, L. S., and Defex, E., *Relation between work of adhesion and work of fracture for simple interfaces,* Journal of Material Science, 2002, **37**, 3: p. 505-513

[44]   Wang, Zhe, et al., *Micropatterning of Organic Semiconductor Microcrystalline Materials and OFET Fabrication by "Hot Lift Off",* Journal of American Chemistry Society, 2003, **125**: p. 15278-15279

[45]   Plazek, D. J., and Ngai, K. L., *Correlation of polymer segmental chain dynamics with temperature dependent time-scale shifts*, Macromolecules, 1991, **24**: p. 12212-1224

[46]   Roland, C. M., and Santagelo, P. G., *Effect of temperature on the terminal relaxation of branched polydimethysiloxane,* Journal of Non-Crystalline Solids, 2002, 307-310

[47]   Feng, X., et al., *Competing Fracture in Kinetically Controlled Transfer Printing,* Langmuir, 2007, **23**: p. 12555-12560

Chapter 5.   Conclusion

Micro-Lego discussed in this thesis incorporates introduction of new ink materials i.e. SiO_2 and SU-8 and the utilization of the inks along with previously demonstrated Si and Au ink through the deterministic transfer printing in conjunction with the irreversible permanent joining to construct microscale 3D structures and devices with unusual form factors. For successful micro-Lego process, three major constituents are required, proper manipulator (i.e. stamp), preparation of donor substrate composed of transferred object (ink) and appropriate irreversible joining schemes. Firstly, multiple microtip PDMS stamp is developed for versatility in manipulating diverse configuration and dimension solid ink objects. The multiple microtip PDMS stamp exhibits superb adhesion on / off ratio attributed by restoration of the microtips as well as the viscoelastic property of the PDMS stamp. Secondly, representative materials from each semiconductor (silicon), metal (gold), dielectric (silicon dioxide) and polymer (SU-8) classes are processed into retrievable ink format. Although the developed raw materials are limited, any functional materials i.e. photonic crystal based on Si, can be processed in the consistent method to create inks. Lastly, the irreversible permanent joining schemes; fusion bonding, eutectic bonding, cold welding and adhesive bonding, are borrowed from wafer scale and employed for irreversible permanent joining without adhesive layers.

Microscale joining displays different characteristics such that unlike the bulk scale joining process, external pressure to make intimate contact is irrelevant, as confirmed by blister tests and nanoindenter experiments. It was suspected that in microscale, the defect sites as well as angular misalignments are less probable, which induces conformal contact between the transfer printed ink and the receiving substrate. Furthermore, electrical contact at the interface was investigated by transmission line measurement and by simply comparing with lithographically prepared reference

specimen, which revealed consistent contact resistance with the reference specimen. Through micro-Lego processes, heterogeneously integrated complex 3D micro structures are constructed as well as functional microsystems, which have benefited in terms of higher functionality or by simplifying the manufacturing process.

In addition to the development of micro-Lego process, patterning of QD layer prepared from colloidal QD had been investigated. The first attempt was carried out by utilizing shape memory polymer (SMP), which inhibits switchable elastic modulus across glass transition temperature (T_g). At elevated temperature (above T_g), the material is compliant that allows perfect contact with the QD layer. Once contact is established, the SMP is cooled to exhibit solid-like state, which induces higher pull-off force and subsequently removing the contacting area. The employment of SMP enables successful removal of QD regardless of preload and retrieval rate, which are required for PDMS patterning processes.

Additionally, QD layer patterning through PR layer on PDMS slab support was studied. The PR is patterned through photolithography that ensures high resolution features in the PR layer. Although PR layer is fully cured during the photolithography process, the layer still accompanies tacky surface, that facilitates QD patterning in high resolution at relatively low separation rate and preload. Furthermore, composite ink preparation by transferring the PR layer onto QD layer coated substrate was conducted. Following the transferring of the PR layer, chrome and gold were deposited by sputter, and successive removal of the PR layer by commercially available Scotch^{TM} tape exposed finely defined QD composite ink arrays for subsequent transfer printing processes. The vertical integration of red, green and blue QD square inks patterned through PR stamping established potential application of PR stamping scheme in QD manufacturing processes.

Chapter 6.   Future research plan

6.1 Through silicon via (TSV) background

The resolution of IC and MEMS are in the realm of nanometers with enhancements in photolithography. The reduction in feature sizes benefited by creation of higher performing devices not only by accommodating higher number of transistors in the same form factor. In contrarily, due to the high-density configuration of the modern devices, accommodating the large number of I/O pins without sacrificing power consumption and data transfer delay became challenges in electrical interconnections [1,2]. In this context, 3D IC integration via through silicon via (TSV), which is prepared by conventional micromanufacturing technology that permits fabrication of interconnects at moderately high-aspect ratio with dense form factor that is compatible with I/O pins is a promising solution [3]. Conventionally, TSVs are fabricated and assembled through flip-chip bonding technique in wafer scale where TSVs are prepared on a wafer and joined with separately prepared receiving wafer in the packaging stage [4]. While the deterministic parallel microassembly protocol of flip-chip bonding creates devices in cost efficient manner, the process suffers in integration at inconsistent topology for fabrication of multi-level system on chip (SoC) since manipulation of individual interposers are not yet achieved. Furthermore, the process is largely utilized in the packaging stage of the manufacturing process, which bounds the utilization of TSV as a device component. In this context, adaptation of micro-Lego technique for TSV assembly can benefit by integrating microscale TSV at specifically required spatially organized miniscule site.

6.2 Current stage of the development

To examine the feasibility of micro-Lego assembly of TSV, a prototype of TSVs made of polyimide (PI) structure material with via patterns filled with electroplated copper (Cu) is explored

owing to the convenience in the micromanufacturing of the PI. **Figure 6.1** depicts micro-Lego assembly of a PI interposer on a patterned Cu layer on a Si foreign substrate, which involves transfer printing of a PI interposer from its donor substrate and thermal joining at 120 ⁰C for 15 min under a compressive load of 700 kPa by a pressing block [5]. The fabrication of PI interposers in the donor substrate is shown in **Figure 6.2**. PI structure material is adopted at the early stage of the interposer ink fabrication due to its accessibility and compatibility with other etching, electroplating and thermal processes. On a silicon (Si) substrate, poly (methyl methacrylate) (PMMA) and PI are spin casted, which forms approximately 200 nm and 1.5 μm film. The two layers are then O_2 plasma etched to form via holes. The removal of PMMA layer is advantageous since it results in corresponding thickness of Cu bump as well as tethering of interposers onto the substrate after removing the sacrificial PMMA layer. Subsequently, Cu is deposited to fill the via holes and excessive Cu is removed through an etch back process. After the formation of Cu vias and lines, the PI layer is defined into desired microscale configuration using O_2 plasma etching followed with removal of PMMA sacrificial layer in acetone.
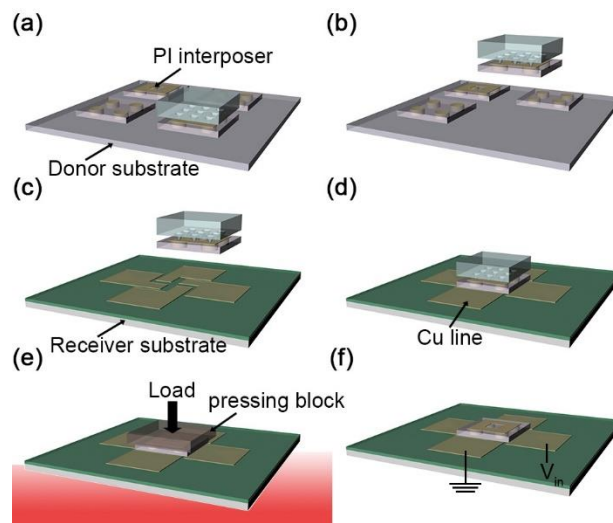

Figure 6.1 *Micro-Lego procedure of the PI interposer. (a) interposer is prepared on a donor substrate (b) a PI interposer is retrieved using an elastomeric stamp (c) the interposer is delivered*

onto receiver substrate (d) printing of the PI interposer (e) thermal compression joining (f) fully assembled PI interposer is tested by applying bias between two pads
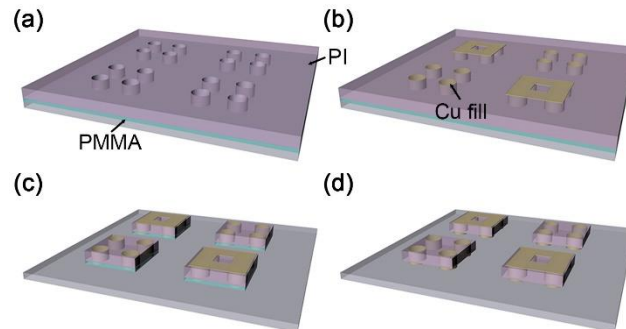

Figure 6.2 *PI interposer ink fabrication procedure. (a) PMMA and PI are applied onto Si substrate followed with O_2 plasma etching of the polymeric layer (b) Cu filling and line formation (d) defining individual retrievable microscale objects (e) removal of PMMA sacrificial layer*

Figure 6.3 (a) is the optical microscopy image and **Figure 6.3 (b)** is the zoom in scanning electron microscopy image (SEM) of a via after thermal compression joining. The SEM image is colorized to distinguish Cu (yellow), PI (purple) and SiO_2 (untouched color). The Cu-Cu mechanical joining strength between Cu bumps of a PI interposer and Cu lines of a foreign substrate after thermal compression was qualitatively verified with a peeling test. A polydimethylsiloxane (PDMS) slab was placed on an assembled PI interposers and peeled without causing a failure of Cu-Cu joining. The electrical contact quality of the joined Cu–Cu interface is examined by measuring an I-V curve with a probe station. **Figure 6.4** shows the micro-Lego assembled PI interposer and reference I-V curve. While the raw data shows slight distinction between the two samples, converting the data into resistivity yields 5.49×10^{-8} Ωm and 1.92×10^{-8} Ωm respectively, which validates our claim that micro-Lego assembled PI interposer is capable of interconnect devices in different topology.

The following research objects remain for future works. Firstly, multi-stacking of the demonstrated PI interposer and subsequently measuring I-V curve to obtain comprehensive contact

resistance would further validate our Cu – Cu thermal compression joining schemes. Secondly, incorporation of functional device will enrich the research. Current stage merely demonstrates the micro-Lego assembly of PI interposer and its contact resistance without clear manifestation. A simple functional component, such as LED printed on top of the PI interposer can widely attract more readers. Lastly and far most, utilization of more robust and reliable structural material such as Si remains as a future objective. While the PI satisfactorily serve as a structural material, the material is not compatible with other deposition methods that are conducted in elevated temperature. Deposition of dielectric layer and diffusion barrier layers are necessary for reliable and long lasting operation of the interposer, which are commonly deposited in close to degradation temperature of the PI. Replacing the PI with another material can potentially broaden the application of the micro-Lego assembled interposers.
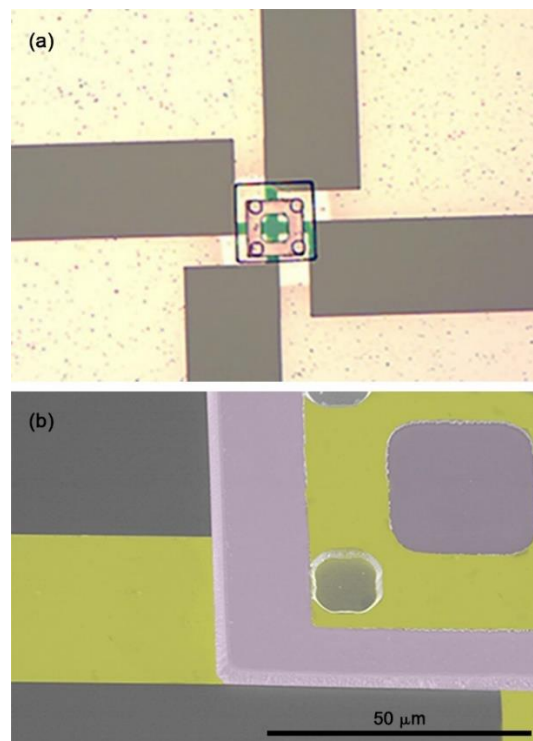

Figure 6.3 PI interposer (a) optical image of the PI interposer joined with Cu pattern and (b) zoom in view of one of the via. The image is colorized to distinguish the Cu (yellow), PI (purple) and SiO$_2$ (untouched)

135
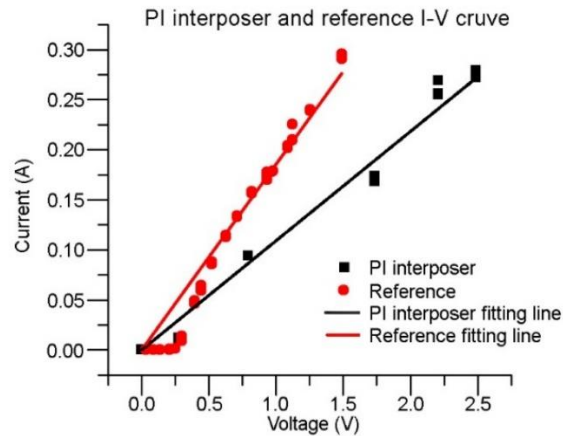
Figure 6.4 *PI interposer and reference I-V curve. The slope of the two lines, which represents that 1/R values different by a margin. However, the conversion of the resistance value into resistivity yields consistent data between the two plots*

6.3 **References**

[1]   Reif, R., et al., *VLSI-SoCL: Technologies for System Integration,* Quality Electronic Design Proceedings International Symposium on IEEE, 2002

[2]   Zhang, X., et al., *Heterogeneous 2.5 D integration on through silicon interposer,* Applied Physics Review, 2015, **2**, 2, 021308

[3]   Mediouni, N., Abid, S. B., Kallel, O., and Hasnaoui, S., *Modeling and Performance Evaluation of 2D and 3D NoCs using Discrete Event Simulation,* International Journal of Computer Application, 2016, Vol. **137**, Number 12

[4]   Jang, D. M., et al., *Development and evaluation of 3-D SiP with vertically interconnected through silicon vias (TSV)*, Electronic Components and Technology Conference, 2007, 57th IEEE

[5]   Keum, H., et al., *Microassembly of Heterogeneous Materials using Transfer Printing and Thermal Processing,* Scientific Reports, 2016, **6**, 29925